

## ABSTRACT

LIU, JIA. Density Functional Study on the Magnetic Structures of Some Transition-Metal Magnetic Oxides. (Under the direction of Mike H. Whangbo).

In this thesis we describe results of our density functional theory (DFT) electronic structure studies on the magnetic properties of some magnetic oxide systems containing transition-metal magnetic ions  $\text{Cu}^{2+}$ ,  $\text{Fe}^{2+}$ ,  $\text{Ag}^{2+}$ ,  $\text{Co}^{2+}$  and  $\text{Mn}^{4+}$ . Results of our DFT calculations on  $\text{FeTe}_3\text{O}_7\text{X}$  ( $\text{X} = \text{Cl}, \text{Br}$ ),  $\text{Ag}_2\text{ZnZr}_2\text{F}_{14}$ ,  $\text{LiNaCo}[\text{PO}_4]\text{F}$  and  $\text{CuAs}_2\text{O}_4$  have been published. Results of our DFT calculations concerning the origin of the magnetic anisotropy of spin-half  $\text{Cu}^{2+}$  ions have been written up for publication, and our studies on  $\text{Bi}_3\text{Mn}_4\text{O}_{12}(\text{NO}_3)$  and  $\text{ACo}_2\text{V}_2\text{O}_8$  ( $\text{A} = \text{Ba}, \text{Pb}, \text{Sr}$ ) have just been completed.

© Copyright 2014 Jia Liu

All Rights Reserved

Density Functional Study on the Magnetic Structures of Some Transition-Metal Magnetic  
Oxides

by  
Jia Liu

A dissertation submitted to the Graduate Faculty of  
North Carolina State University  
in partial fulfillment of the  
requirements for the degree of  
Doctor of Philosophy

Chemistry

Raleigh, North Carolina

2014

APPROVED BY:

---

Mike H. Whangbo (Chair)

---

Paul Maggard

---

Jerry L. Whitten

---

David A. Shultz

## **DEDICATION**

I dedicate my work to my families and friends. I feel grateful for all the support from my loving parents, Xiaoping and Hongao Liu who encouraged me along the way. Here I specially thank my dear husband, who unconditionally supported me in the past few years.

Also I have to thank my academic advisor Dr. Mike Whangbo for his patient and generous guidance in the past 5 years. The things I have learned are beyond science and they will help me in every step of the way to my success.

此文谨献给我的父母和爱人。

Dedicated to my parents and dear husband.

## **BIOGRAPHY**

Jia Liu, born and raised in Dalian, got her Bachelor's degree in Science majoring in Chemistry from University of Science and Technology Beijing in 2007. Her Master's degree in Chemistry was received from the College of William and Mary in 2009. Since then, she joined the Department of Chemistry in North Carolina State University to pursue her PhD degree. In the past five years, she mainly studied in the area of Density Functional Theory on some magnetic solids with supervisor Dr. Mike Whangbo. She attended several international conferences and workshops to present her work, such as annual APS meeting, Gordon Research Conference and so on.

## ACKNOWLEDGMENTS

I wish to thank my committee members who shared their time and effort in my research. A special thanks to Dr. Mike Whangbo, my advisor for his encouragement and patience throughout the entire process. Thank you Dr. Jerry Whitten, Dr. Paul Maggard, Dr. David Shultz, and Dr. Jonathan Olson for agreeing to serve on my committee.

Also, I would like to express my gratitude to all my past and current colleagues, Chuan Tian, Yuemei Zhang, Dr. Erjun Kan, Dr. Hongjun Xiang, Dr. Chang-hoon Li, Dr. Won-joon Son, Jerry Bettis. They helped me tremendously in the past few years.

I would like to acknowledge and thank HPC center at North Carolina State University and NERSC high performance computing center for allowing me to carry out my research projects for valuable computing time. Special thanks go to the members of Chemistry Department at NCSU for continuous support.

Finally, I have to thank my families again for their unconditional love and support.

## TABLE OF CONTENTS

LIST OF TABLES.....	vii
LIST OF FIGURES.....	ix
CHAPTER 1. INTRODUCTION.....	1
CHAPTER 2. THEROTICAL CONSIDERATIONS.....	1
REFERENCES.....	19
CHAPTER 3. SPIN EXCHANGE INTERACTIONS AND MAGNETIC STRUCTURE OF FeTe <sub>3</sub> O <sub>7</sub> X (X = Cl, Br).....	30
REFERENCES.....	33
CHAPTER 4. MAGNETIC STRUCTURE AND SPIN EXCHANGE INTERACTIONS OF Ag <sub>2</sub> ZnZr <sub>2</sub> F <sub>14</sub> .....	41
REFERENCES.....	43
CHAPTER 5. MAGNETIC STRUCTURE AND SPIN ORIENTATINO IN LiNaCo[PO <sub>4</sub> ]F .....	50
REFERENCES.....	54
CHAPTER 6. SPIN FRUSTRATION AND FIELD-INDUCED MAGNETIC ORDER IN Bi <sub>3</sub> Mn <sub>4</sub> O <sub>12</sub> (NO <sub>3</sub> ).....	62
REFERENCES.....	67
CHAPTER 7. CHARACTERIZATION OF THE SPIN-1/2 LINEAR-CHAIN FERROMAGNET CuAs <sub>2</sub> O <sub>4</sub> .....	75
REFERENCES.....	80

CHAPTER 8. QUASI-ONE-DIMENSTIONAL SPIN CHAIN SYSTEM $ACo_2V_2O_8$ (A = Sr, Ba, Pb).....	88
REFERENCES.....	92
CHAPTER 9. SINGLE ION ANISOTROPY OF SPIN-1/2 SYSTEMS.....	101
REFERENCES.....	111
CHAPTER 10. CONCLUDING REMARKS.....	118

## LIST OF TABLES

<b>Table 3.1</b> Spin exchange constants (in meV) of $\text{FeTe}_3\text{O}_7\text{Cl}$ and $\text{FeTe}_3\text{O}_7\text{Cl}$ obtained from GGA calculations.....	34
<b>Table 4.1</b> Relative energies (in meV) of the ordered spin states AF1 – AF4 of $\text{Ag}_2\text{ZnZr}_2\text{F}_{14}$ obtained from GGA+U calculations as a function of U (in eV).....	44
<b>Table 4.2</b> Values (in meV) of the spin exchanges $J_1 - J_3$ of $\text{Ag}_2\text{ZnZr}_2\text{F}_{14}$ obtained from GGA+U calculations as a function of U (in eV).....	45
<b>Table 5.1</b> Relative energies (in meV) of the ordered spin states FM – AF6 of $\text{LiNaCo}[\text{PO}_4]\text{F}$ obtained from GGA+U calculations as a function of U (in eV).....	55
<b>Table 5.2</b> Values (in K) of the spin exchanges $J_1 - J_4$ of $\text{LiNaCo}[\text{PO}_4]\text{F}$ along with the calculated Curie-Weiss temperature $\theta$ (in K) obtained from GGA+U calculations as a function of U (in eV).....	56
<b>Table 6.1</b> Relative energies of eight spin ordered states (in meV/8FUs) with GGA+U calculations with $U = 0 - 4$ eV.....	68
<b>Table 6.2</b> Values (in meV) of the spin exchanges $J_1 - J_{c''}$ of $\text{Bi}_3\text{Mn}_4\text{O}_{12}(\text{NO}_3)$ obtained from GGA calculations.....	69
<b>Table 7.1</b> Values of the NN and NNN spin exchange constants, $J_{nn}$ and $J_{nnn}$ , respectively, obtained from the DFT+U calculations along with the Curie-Weiss temperatures.....	83
<b>Table 8.1</b> Energy difference ( $E_{\perp c} - E_{//c}$ ), in meV/Co, obtained from DFT+U+SOC (with $U = 2, 4, 6$ eV) calculations for the FM states ( $\uparrow\uparrow\uparrow\uparrow$ ) of $\text{BaCo}_2\text{V}_2\text{O}_8$ , $\text{PbCo}_2\text{V}_2\text{O}_8$ and $\text{SrCo}_2\text{V}_2\text{O}_8$ , where ( $E_{\perp c} - E_{//c}$ ) refer to the energies for the $\perp c$ and $//c$ spin orientations, respectively .....	93

**Table 9.1** The energy (in meV/Cu) of the  $\parallel_{xy}$  spin orientation with respect to that of the  $\perp_{xy}$  spin orientation,  $E_{\parallel_{xy}} - E_{\perp_{xy}}$ , obtained from the DFT+U+SOC calculations for three models of  $\text{CuCl}_2 \cdot 2\text{H}_2\text{O}$ .....113

**Table 9.2** The values of the three components  $J_{nn-x}$ ,  $J_{nn-y}$  and  $J_{nn-z}$  (in meV) of the nearest-neighbor spin exchange  $J_{nn}$  in  $\text{CuCl}_2 \cdot 2\text{H}_2\text{O}$  determined from DFT+U+SOC calculations.....114

**Table 9.3** The relative energies,  $E_{\parallel_{xy}} - E_{\perp_{xy}}$ , in meV/Cu obtained from DFT+U+SOC calculations for the “isolated  $\text{Cu}^{2+}$  ion” model, the  $\uparrow\downarrow\uparrow\downarrow$  chain model (in parenthesis), and the  $\uparrow\rightarrow\downarrow\leftarrow$  spin-spiral chain model (in square bracket).....115

## LIST OF FIGURES

**Fig. 2.1** Two electronic states that a system with a half-filled band can have: (a) Non-magnetic metallic state, in which both the up-spin and down-spin states are half-filled. (b) Magnetic insulating state, in which the up-spin band is completely filled, but the down-spin band, separated from the up-spin band by a band gap, is empty.....22

**Fig. 2.2** Split patterns of the up-spin and down-spin levels ( $\phi\uparrow$  and  $\phi\downarrow$ , respectively) for the two extreme cases of spin arrangements for a 1D chain with one orbital per site: (a) FM state in which all sites have up-spins. (b) AFM state in which up-spin and down-spin sites alternate. Only two adjacent spin sites of the chain are shown for simplicity.....23

**Fig. 2.3** Orbital interaction between two spin sites described by the magnetic orbitals  $\phi_1$  and  $\phi_2$  leading to the dimer levels  $\psi_1$  and  $\psi_2$  separated by the energy gap  $\Delta e$ .....24

**Fig. 2.4** Weak JT distortion of a  $MO_6$  octahedron with  $(t_{2g})^1$  configuration leading to a distorted  $MO_6$  octahedron with  $C_3$ -rotational symmetry. This distortion splits the  $t_{2g}$  level into the pattern of  $1a < 1e$  pattern, where the  $1a$  level is described by the  $z^2$  orbital, when the local  $z$ -axis is taken along the  $C_3$ -rotational axis.....25

**Fig. 2.5** Energies of the AFM, the unrelaxed FM and the relaxed FM states of a 2D square-lattice antiferromagnet described by the nearest-neighbor AFM spin exchange  $J (< 0)$ . The relaxed FM state is described by a new nearest-neighbor spin exchange  $J'$  for which  $|J'| < |J|$  .....26

**Fig. 2.6** Triangular spin frustration and non-collinear spin arrangement in a triangle of spin sites described by the nearest-neighbor AFM spin exchange  $J (< 0)$ : (a) Spin frustration that

occurs when the spins are collinear. (b) Compromised non-collinear spin arrangement that minimizes the total spin exchange interactions.....27

**Fig. 2.7** Two coordinate systems used to describe the spin-orbit coupling  $\hat{H}_{\text{SOC}} = \lambda \hat{L} \cdot \hat{S}$ , where the spin z'-axis (i.e., the preferred spin direction) is defined in terms of the angles ( $\theta$ ,  $\phi$ ) with respect to the Cartesian coordinate system describing the orbital angular momentum .....28

**Fig. 2.8** (a) Two degenerate electron configurations of  $(\text{Me}_3\text{Si})_3\text{C-Fe-C}(\text{SiMe}_3)_3$  containing a high-spin  $\text{Fe}^{2+}$  ( $d^6$ ) ion in the linear two-coordinate site. (b) Correspondence between the Cartesian and the spherical-harmonics representations for the split d-states of the linear-two coordinate  $\text{Fe}^{2+}$  ( $d^6$ ) ion.....29

**Fig. 3.1** (a) Projection view of the crystal structure of  $\text{FeTe}_3\text{O}_5\text{X}$  ( $\text{X} = \text{Cl, Br}$ ) along b-axis, where the blue, yellow, red and green spheres represent  $\text{Fe}^{3+}$ ,  $\text{Te}^{4+}$ ,  $\text{O}^{2-}$  and  $\text{X}^-$  ions, respectively. (b) An Fe-Te-O slab showing how the  $\text{Fe}_2\text{O}_8$  dimer units (blue polyhedra) are isolated from each other by the Te (grey) and O (red) atoms. The lone pair on  $\text{Te}^{4+}$  is marked as a black circle.....35

**Fig. 3.2** Structures of the  $\text{Fe}_2\text{O}_8$  dimer units in (a)  $\text{FeTe}_3\text{O}_7\text{Cl}$  (**1**) and (b)  $\text{FeTe}_3\text{O}_7\text{Br}$  (**2**) .....36

**Fig. 3.3** Magnetic susceptibilities of  $\text{FeTe}_3\text{O}_7\text{X}$  ( $\text{X} = \text{Cl, Br}$ ) measured with a field of 0.1 T. The solid (red) lines are fits to the susceptibility of a spin dimer of  $\text{Fe}^{3+}$  ( $S = 5/2$ ) cations .....37

**Fig. 3.4** Spin polarized electronic density of states (states/electron FU) of FeTe<sub>3</sub>O<sub>7</sub>Cl in the FM configuration (see Fig. 12). (a) Total density of states. (b) Projected density of states of the Fe d electrons.....38

**Fig. 3.5** Definition of the three spin exchange parameters J<sub>1</sub> (intradimer), J<sub>2</sub>, and J<sub>3</sub> (both interdimer) in FeTe<sub>3</sub>O<sub>7</sub>X (X = Cl, Br).....39

**Fig. 3.6** Four ordered spin states FM, AF1, AF2, and AF3 in a (a, 2b, c) supercell employed to extract the values of J<sub>1</sub>, J<sub>2</sub>, and J<sub>3</sub>, where only the Fe atoms are shown for simplicity. The up-spin and down-spin Fe<sup>3+</sup> sites are represented by spheres of different colors. The numbers in parentheses give the relative energies (in meV) obtained from the GGA calculations with for 1 and 2, respectively.....40

**Fig. 4.1** Perspective view of the crystal structure of Ag<sub>2</sub>ZnZr<sub>2</sub>F<sub>14</sub>. The orange, green, blue and grey represent silver, zirconium, zinc and fluorine atoms, respectively. The AgF<sub>4</sub> units are highlighted (in grey).....46

**Fig 4.2** Two-leg ladders of Ag<sup>2+</sup> ions resulting from Ag<sub>2</sub>F<sub>7</sub> dimers. The dotted lines running along the b-axis represent the short F...F contacts (2.275 Å) between Ag<sub>2</sub>F<sub>7</sub> dimers .....47

**Fig. 4.3** Temperature dependence of the inverse molar susceptibility of Ag<sub>2</sub>ZnZr<sub>2</sub>F<sub>14</sub> at a magnetic field of 1T. The transition at around 163K is caused by a small amount of AgF<sub>2</sub> in the sample.....48

**Fig. 4.4** (a) Intra-ladder spin and inter-ladder spin exchange (J<sub>1</sub> – J<sub>3</sub>) Ag<sub>2</sub>ZnZr<sub>2</sub>F<sub>14</sub>, where the circles represent the Ag<sup>2+</sup> ions. (b) Four ordered spin arrangements used for GGA+U calculations to extract the values of J<sub>1</sub> – J<sub>3</sub>.....49

**Fig. 5.1** Perspective views of the LiNaCo[PO<sub>4</sub>]F structure (a) with and (b) without the phosphorus and alkali metal atoms.....57

**Fig. 5.2** (a) Magnetic susceptibility  $\chi$  vs. Temperature and the corresponding  $\chi^{-1}$  vs. T plots of LiNaCo[PO<sub>4</sub>]F measured with the applied field  $H = 10$  kOe. (b) Heat capacities  $C_p(T)$  of LiNaCo[PO<sub>4</sub>]F. The inset displays  $C_p/T$  in the region of the phase transition at 10.2(5) K .....58

**Fig. 5.3** The magnetic structure of LiNaCo[PO<sub>4</sub>]F at 3K. The components of the moment along x, y, and z axes are 2.13(2), 0, and 0.87(2)  $\mu_B$ , respectively. The total moment is 2.30(2)  $\mu_B$ , and the angle between the moment direction and ab-plane is 22.2 °.....59

**Fig. 5.4** (a, b) Definitions of the spin exchange paths  $J_1, J_2, J_3, J_{1'}, J_{2'},$  and  $J_{3'}$ . The Co1 and Co2 atoms are indicated as empty and filled circles, respectively. The numbers 1, 2, 3, 1', 2' and 3' refer to the spin exchanges  $J_1, J_2, J_3, J_{1'}, J_{2'},$  and  $J_{3'}$ , respectively. (c) Ordered spin arrangements of the Co1 and Co2 spin sites used to extract the values of  $J_1, J_2, J_3, J_{1'}, J_{2'},$  and  $J_{3'}$  by GGA+U calculations. The positions of the Co1FO3 and Co2FO3 chains are identical with those of (a, b), and the up-spin and down-spin  $Co^{2+}$  sites are indicated by empty and filled circles, respectively.....60

**Fig. 6.1** unit cell view of the Bi<sub>3</sub>Mn<sub>4</sub>O<sub>12</sub>(NO<sub>3</sub>) (a) along c-axis. (b) along b-axis with polyhedron shown. (c) Projection view of extended cell. (d) One MnO<sub>6</sub> layer in ab-plane. (e) Two layers of MnO<sub>6</sub> hexagon with BiO<sub>6</sub> octahedron in between in ab-plane. (f) Side view of Bi-Mn<sub>12</sub> unit.....70

**Fig. 6.2** (a) Intra-layer spin exchange paths  $J_1 - J_4$ . (b) Inter-layer spin exchange paths  $J_c - J_{c''}$ . The number 1 - 4 refer to  $J_1 - J_4$ , respectively, and the symbols c - c'' to  $J_c - J_{c''}$ , respectively

.....71

**Fig. 6.3** Total and projected density of state (DOS) plots of (a) experimental and (b) optimized structure.....72

**Fig. 6.4** Eight spin ordered states from FM - AF7 for (2a, b, 2c) supercell.....73

**Fig. 6.5** (a) Neutron powder diffraction patterns in  $\text{Bi}_3\text{Mn}_4\text{O}_{12}(\text{NO}_3)$   $E = 1.7$  meV at  $H = 0$  and 10 T and at  $T = 3$  K. At 10 T the broad magnetic peak is reduced and sharp magnetic peaks appear. (b) Magnetic structure in the magnetic field-induced phase. The  $\text{Mn}^{4+}$  ions in a  $2 \times 2 \times 2$  supercell are shown. The magnetic moments lie in the ab plane, although the direction of the magnetic moments in the plane cannot be determined uniquely. Magnetic interactions  $J_1, J_2$ , and  $J_c$  are also shown.....74

**Fig. 7.1** (a) Projection along the [001] direction of the trippkeite crystal structure. The  $\text{Cu}^{2+}$  atoms are represented by the large (green) spheres, the oxygen atoms by small (red) spheres, and the As atoms by (gray) medium spheres. (b) A corrugated chain of trans-edge connected  $\text{CuO}_6$  octahedra highlighting the twisted basal planes of the octahedra in  $\text{CuAs}_2\text{O}_4$ , which lead to a corrugation of the  $\text{CuO}_2$  ribbon chains.....84

**Fig. 7.2** Reciprocal magnetic susceptibility of a polycrystalline  $\text{CuAs}_2\text{O}_4$  sample measured in a field of 1 T. The solid (red) line is a fit of the Curie-Weiss law to the data above 150 K. The lower inset shows the data below 20 K, collected at 0.01 T, in an enlarged scale. The upper inset displays the magnetization versus field collected at 1.85 K.....85

**Fig. 7.3** Three order spin states of CuAs<sub>2</sub>O<sub>4</sub> used to determine the values of  $J_{nn}$  ( $\equiv J_1$ ) and  $J_{nnn}$  ( $\equiv J_2$ ) by DFT+ $U$  calculations. Only the Cu sites are shown for simplicity. The unfilled and filled circles represent up-spin and down-spin Cu<sup>2+</sup> sites, respectively.....86

**Fig. 7.4** The ratio of the NN to NNN spin exchange constants of CuAs<sub>2</sub>O<sub>4</sub> calculated from the DFT+ $U$  calculations as a function of  $U_{\text{eff}}$ . The plot displays the dominance of the FM  $J_{nn}$  term over the AFM  $J_{nnn}$  term.....87

**Fig. 8.1** (a) Projection view of ACo<sub>2</sub>V<sub>2</sub>O<sub>8</sub> (A = Sr, Ba, Pb) on the ab-plane. The octahedra, tetrahedra, large ball and small ball represent CoO<sub>6</sub>, VO<sub>4</sub>, A, and O, respectively. The circle shows the Co<sub>4</sub>V<sub>4</sub>O<sub>16</sub> cluster of a unit cell. (b) Perspective view of the Co<sup>2+</sup> arrangements along the c-direction. (c) Projection view of ACo<sub>2</sub>V<sub>2</sub>O<sub>8</sub> on the bc-plane.....94

**Fig. 8.2** Temperature variation of magnetization for (a) SrCo<sub>2</sub>V<sub>2</sub>O<sub>8</sub> and (b) BaCo<sub>2</sub>V<sub>2</sub>O<sub>8</sub> in an applied magnetic field of 5 KOe. The inset shows a zoomed-in view in 2 – 30 K range  
.....95

**Fig. 8.3** Specific heats of SrCo<sub>2</sub>V<sub>2</sub>O<sub>8</sub> and BaCo<sub>2</sub>V<sub>2</sub>O<sub>8</sub> measured in zero magnetic field  
.....96

**Fig. 8.4** Split pattern of the d-states of a high-spin Co<sup>2+</sup> ion in an axially-compressed CoO<sub>6</sub> octahedron with the C<sub>4</sub>-rotational symmetry.....97

**Fig. 8.5** PDOS plots obtained for the Co 3d states of BaCo<sub>2</sub>V<sub>2</sub>O<sub>8</sub> from DFT+ $U$  ( $U = 2, 4, 6$  eV) calculations for the FM state.....98

**Fig. 8.6** PDOS plots obtained for the Co 3d states of PbCo<sub>2</sub>V<sub>2</sub>O<sub>8</sub> from DFT+ $U$  ( $U = 2, 4, 6$  eV) calculations for the FM state.....99

**Fig. 8.7** PDOS plots obtained for the Co 3d states of SrCo<sub>2</sub>V<sub>2</sub>O<sub>8</sub> from DFT+U (U = 2, 4, 6 eV) calculations for the FM state.....100

**Fig. 9.1** (a) A perspective view of the crystal structure of CuCl<sub>2</sub>·2H<sub>2</sub>O (blue circle: Cu, yellow circle: Cl, red circle: O, white circle: H). (b) The magnetic structure of CuCl<sub>2</sub>·2H<sub>2</sub>O, where the filled and unfilled circles represent up-spin and down-spin Cu<sup>2+</sup> sites, respectively. (c) The local coordinate system chosen for an isolated CuCl<sub>2</sub>(OH<sub>2</sub>)<sub>2</sub> complex with the crystal-field split Cu 3d states. (d) The PDOS plots calculated for the Cu 3d states of CuCl<sub>2</sub>·2H<sub>2</sub>O using the “isolated Cu<sup>2+</sup> ion” model.....116

**Fig. 9.2** (a) A schematic view of a CuL<sub>2</sub> (L = O, Cl, Br) ribbon chain found in LiCuVO<sub>4</sub>, CuCl<sub>2</sub> and CuBr<sub>2</sub>. (b) A schematic view of the ↑→↓← spin-spiral arrangement in the CuL<sub>2</sub> ribbon chain, for the case when the spin-spiral plane is the xy-plane. (c) An “isolated Cu<sup>2+</sup> ion” model, in which a chain of Cu<sup>2+</sup> ions is replaced with a (Cu<sup>2+</sup>-Mg<sup>2+</sup>-Mg<sup>2+</sup>-Mg<sup>2+</sup>)<sub>∞</sub> chain. (d) A schematic view of the ↑↓↑↓ collinear arrangement of Cu<sup>2+</sup> spins in the CuL<sub>2</sub> ribbon chain, for the case when the spins lie in the xy-plane. (e) The PDOS plots calculated for the Cu 3d states of CuCl<sub>2</sub> .....117

## 1. Introduction

We have investigated the structure-property relationships in a number of magnetic oxides containing transition-metal magnetic ions  $\text{Cu}^{2+}$ ,  $\text{Fe}^{2+}$ ,  $\text{Ag}^{2+}$ ,  $\text{Co}^{2+}$  and  $\text{Mn}^{4+}$  on the basis of DFT electronic structure calculations. They include  $\text{FeTe}_3\text{O}_7\text{X}$  ( $\text{X} = \text{Cl}, \text{Br}$ ),  $\text{Ag}_2\text{ZnZr}_2\text{F}_{14}$ ,  $\text{LiNaCo}[\text{PO}_4]\text{F}$ ,  $\text{CuAs}_2\text{O}_4$ ,  $\text{Bi}_3\text{Mn}_4\text{O}_{12}(\text{NO}_3)$ ,  $\text{ACo}_2\text{V}_2\text{O}_8$  ( $\text{A} = \text{Ba}, \text{Pb}, \text{Sr}$ ) and several other oxides of  $\text{Cu}^{2+}$  ions. In this document, we report results of our investigations on these magnetic materials. Our DFT studies on  $\text{FeTe}_3\text{O}_7\text{X}$  ( $\text{X} = \text{Cl}, \text{Br}$ ),  $\text{Ag}_2\text{ZnZr}_2\text{F}_{14}$ ,  $\text{LiNaCo}[\text{PO}_4]\text{F}$ ,  $\text{Mn}[\text{N}(\text{CN})_2]_2$  and  $\text{CuAs}_2\text{O}_4$  have been published. Results of our DFT calculations concerning the origin of the magnetic anisotropy of spin-half  $\text{Cu}^{2+}$  ions have been written up for publication, and our studies on  $\text{Bi}_3\text{Mn}_4\text{O}_{12}(\text{NO}_3)$  and  $\text{ACo}_2\text{V}_2\text{O}_8$  ( $\text{A} = \text{Ba}, \text{Pb}, \text{Sr}$ ) have just been completed. This dissertation is organized as follows: Section 2 provides a brief review on the general concepts necessary for understanding magnetic solids and describes the computational methods employed in this study. Results of our studies on  $\text{FeTe}_3\text{O}_7\text{X}$  ( $\text{X} = \text{Cl}, \text{Br}$ ),  $\text{Ag}_2\text{ZnZr}_2\text{F}_{14}$ ,  $\text{LiNaCo}[\text{PO}_4]\text{F}$ ,  $\text{CuAs}_2\text{O}_4$ , several magnetic oxides of  $\text{Cu}^{2+}$  ions,  $\text{Bi}_3\text{Mn}_4\text{O}_{12}(\text{NO}_3)$  and  $\text{ACo}_2\text{V}_2\text{O}_8$  ( $\text{A} = \text{Ba}, \text{Pb}, \text{Sr}$ ) are presented in Sections 3 – 9.

## 2. Theoretical considerations<sup>1</sup>

In magnetic oxides composed of transition-metal ions  $\text{M}^{n+}$  in oxidation state  $+n$ , the transition-metal elements form  $\text{MO}_m$  polyhedra with their first-coordinate O atoms, and these polyhedra are interlinked to make M-O-M and/or M-O...O-M connections between adjacent  $\text{M}^{n+}$  ions. The unpaired spins of the  $\text{M}^{n+}$  ions are accommodated in the d-levels of the  $\text{MO}_m$  polyhedra, so that the interactions between adjacent magnetic ions  $\text{M}^{n+}$  take place through

those M-O-M and/or through M-O...O-M paths to which the magnetic orbitals have non-zero orbital contributions. Thus, the effective interaction between adjacent  $M^{n+}$  ions increases by increasing the overlap of the M nd orbitals with the O 2p orbitals in the M-O bonds. In general, the nd orbital of M in zero oxidation state shows spatial extension that increases in the order  $3d < 4d < 5d$ , so the widths of the d-block bands should increase in the order  $3d < 4d < 5d$ . Furthermore, with increasing the spatial extension of the M nd orbital, the electron correlation associated with the M nd orbitals should decrease thereby decreasing their on-site repulsion  $U$  in the order  $3d > 4d > 5d$ . Consequently, magnetic insulators are more frequently found for 3d metal oxides than for 4d/5d metal oxides. Nevertheless, a number of 4d/5d metal oxides become magnetic insulators when their d-orbitals are strongly contracted, which occurs when their  $M^{n+}$  ions are in high oxidation state. In this section we will briefly survey various conceptual, theoretical and computational issues that are needed in analyzing the structure-property relationships of transition-metal magnetic oxides on the basis of electronic band structure calculations and orbital-interaction analysis.

## 2.1. Magnetic insulating versus metallic state<sup>1</sup>

The electronic properties of crystalline magnetic solids are commonly discussed on the basis of DFT electronic band structure calculations. There are several different ways of doing DFT calculations for crystalline solids, namely, the non-spin-polarized DFT, the spin-polarized DFT, and the spin-polarized DFT+U, where U refers to the on-site repulsion on magnetic ions. In the non-spin-polarized DFT method, each energy level of a given band accommodates two electrons (i.e., up-spin and down-spin electrons) so that a given band

consists of up-spin and down-spin subbands degenerate in energy (**Fig. 2.1a**). Consequently, any solid with partially filled bands has no energy gap between the highest-occupied and the lowest-unoccupied band levels, and is therefore predicted to be a non-magnetic metal. However, a solid with partially-filled bands can be a magnetic insulator,<sup>2,3</sup> in which up-spin and down-spin subbands differ in energy such that an energy gap (i.e., a band gap) occurs between the highest-occupied and the lowest-unoccupied subbands (**Fig. 2.1b**). It should be recalled that the presence of partially-filled bands is only a necessary condition for a system to become either a metal or a magnetic insulator. The failure of the non-spin-polarized DFT method in describing magnetic insulators is partly remedied by employing the spin-polarized DFT method, which allows up-spin and down-spin subbands to have different spatial orbitals and hence differ in energy. For most magnetic insulators, however, this splitting of up-spin and down-spin subbands given by the spin-polarized DFT method is not large enough to produce a band gap. Currently, this deficiency of the spin-polarized DFT method is empirically corrected by using the spin-polarized DFT+U method,<sup>4</sup> which adds on-site repulsion  $U$  on the magnetic transition-metal atoms to enhance the spin polarization of their  $d$  orbitals (**Fig. 2.2**).

At the current level of DFT, it is unfortunately impossible to predict whether a solid with partially-filled bands will be a metal or a magnetic insulator. Nevertheless, once such a solid is experimentally known to be a magnetic insulator, it is always possible to generate its magnetic insulating states in terms of spin-polarized DFT+U calculations by gradually increasing the value of  $U$ . For most cases, this empirical approach is successful. However, it is an unsettled question when to find stop increasing the  $U$  value. In short, the spin-polarized

DFT+U method, currently employed to describe magnetic insulating states, is empirical because  $U$  is an empirical parameter. In describing a magnetic insulator by this method, therefore, it is important to first establish a range of  $U$  values producing a band gap and then explore their chemistry and physics on the basis of consistent trends resulting from such  $U$  parameters.

## 2.2. Spin exchange interaction<sup>1</sup>

In analyzing experimental results (e.g., magnetic susceptibility, specific heat and spin wave dispersion) in terms of the spin Hamiltonian

$$\hat{H}_{\text{spin}} = -\sum_{i<j} J_{ij} \hat{S}_i \cdot \hat{S}_j, \quad (1)$$

the spin exchange parameters  $J_{ij}$  are numerical fitting parameters needed to reproduce these results. Consequently, the signs and magnitudes of these “experimental”  $J_{ij}$  parameters depend on the spin lattice chosen for the spin Hamiltonian, and two different sets of  $J_{ij}$  values may provide an equally acceptable fitting.<sup>5</sup> It is essential to examine the electronic structure of a magnetic solid to obtain a relevant spin lattice.

### 2.2.a. Qualitative aspect<sup>1</sup>

For a spin dimer made up of two equivalent spin sites with one electron per site, suppose that the two spin sites 1 and 2 are described by the magnetic orbitals  $\phi_1$  and  $\phi_2$ , respectively. The interaction between  $\phi_1$  and  $\phi_2$  leads to the molecular levels  $\psi_1$  and  $\psi_2$  of the dimer separated by  $\Delta e$  in energy (**Fig. 2.3**). The allowed spin states of this spin dimer are the

singlet and triplet states with the energy difference between them as  $\Delta E = E_S - E_T$ . This energy spectrum is reproduced by the spin Hamiltonian,

$$\hat{H}_{\text{spin}} = -J\hat{S}_1 \cdot \hat{S}_2, \quad (2)$$

if  $J = \Delta E$ . When the spin sites 1 and 2 are described by the magnetic orbitals  $\phi_1$  and  $\phi_2$ , respectively, then the J parameter is written as <sup>5,6</sup>

$$J = J_F + J_{AF} = 2K_{12} - \frac{(\Delta e)^2}{U^{\text{eff}}} \quad (3)$$

The FM component  $J_F$  is proportional to the exchange integral  $K_{12}$ , which increases with increasing the overlap density  $\phi_1\phi_2$ . The AFM component  $J_{AF}$  is proportional to  $(\Delta e)^2$  and is inversely proportional to the effective on-site repulsion  $U^{\text{eff}}$ . Since  $\Delta e$  is proportional to the overlap integral  $\langle \phi_1 | \phi_2 \rangle$ , the magnitude of  $J_{AF}$  increases with increasing  $\langle \phi_1 | \phi_2 \rangle$ . Therefore, a spin exchange becomes AFM when the overlap integral  $\langle \phi_1 | \phi_2 \rangle$  is large and the overlap density  $\phi_1\phi_2$  is small, but becomes FM when the overlap integral  $\langle \phi_1 | \phi_2 \rangle$  is small and the overlap density  $\phi_1\phi_2$  is large.

In magnetic solids made up of  $\text{MO}_m$  polyhedra, the interaction between spin sites, say, M1 and M2, takes place through the superexchange M1-O-M2 path or through the super-superexchange M1-O...O-M2 path. As mentioned earlier, the magnetic orbitals of  $\text{MO}_m$  have the M nd orbitals combined out-of-phase with the O 2p orbitals. Therefore, the overlap density  $\phi_1\phi_2$  and the overlap integral  $\langle \phi_1 | \phi_2 \rangle$  between the magnetic orbitals  $\phi_1$  and  $\phi_2$  are governed primarily by their O 2p orbitals located on the bridging O atom in the case of the M1-O-M2 superexchange and by those lying on the two O atoms in the case of the M1-

O...O-M2 super-superexchange. Namely, the sign and magnitude of a spin exchange interaction between two spin sites is determined primarily by the tail parts (i.e., the O 2p orbitals) of their magnetic orbitals lying only in the region between them.<sup>5</sup> This is the reason why a spin Hamiltonians defined in terms of only pair-wise spin exchange interactions can provide a good description for the excitation energy spectrum of a given magnetic solid.

It is important to recall that, for magnetic solids consisting of both M-O-M superexchange and M-O...O-M super-superexchange paths, spin exchange interactions that occur through super-superexchange paths with short O...O contact distances (i.e., around the van der Waals distance and shorter) can be much stronger than those through M-O-M paths, and hence should not be neglected.<sup>5</sup> In particular, for a M1-O...O-M2 super-superexchange path in which the O...O contact is linked through a  $d^0$  cation  $M'^{n+}$  (e.g.,  $V^{5+}$ ,  $Mo^{6+}$  and  $W^{6+}$ ) to form an O...M'...O linkage, the empty d-orbitals of  $M'$  can overlap effectively with the magnetic orbitals of both M1 and M2 and hence dramatically enhance or reduce the spin exchange interaction between M1 and M2,<sup>7,8</sup> depending on the symmetry of the linkage. Even when the O...O contact is linked through an alkaline earth cation  $A^{2+}$  (e.g.,  $Sr^{2+}$ ) to form an O...A...O linkage, whether the M1-O...A...O-M2 spin exchange is FM or AFM can be influenced by the virtual d-orbitals of  $A^{2+}$ .<sup>9</sup>

### **2.2.b. Quantitative evaluation by energy-mapping<sup>1</sup>**

Spin exchange parameters are quantitatively evaluated by performing the energy mapping analysis based on DFT+U calculations. Suppose one identifies a set of N spin exchange paths to consider for a given magnetic solid. To evaluate the values of the

associated spin exchange parameters  $J_1, J_2, \dots, J_N$ , the energy-mapping method determines the electronic energies  $E_{\text{elec}}$  of the  $N+1$  ordered spin states (i.e., broken-symmetry states) ( $i = 1, 2, \dots, N+1$ ) by DFT+U calculations so as to obtain  $N$  relative energies  $\Delta E_{\text{elec}}$ . For these calculations, it is important to make sure that all ordered-spin states are magnetic insulating states. The total spin exchange energies  $E_{\text{spin}}$  of the  $N+1$  ordered spin states can be determined by using the spin Hamiltonian  $\hat{H}_{\text{spin}}$  (Eq. 1) defined in terms of  $J_1, J_2, \dots, J_N$  (namely,  $J_{ij} = J_1 - J_N$ ) so as to determine  $N$  relative energies  $\Delta E_{\text{spin}}$  expressed in terms of  $N$  parameters  $J_1 - J_N$ . In writing the expression of the total spin exchange energy for an ordered spin state in terms of  $J_1 - J_N$ , we employ the energy expressions for the FM and AFM arrangements of a general spin dimer whose spin sites  $i$  and  $j$  possess  $N_i$  and  $N_j$  unpaired spins (hence, spins  $S_i = N_i/2$  and  $S_j = N_j/2$ ), respectively.<sup>10</sup> Given  $J_{ij}$  as the spin exchange parameter for this spin dimer, the FM and AFM arrangements of this spin dimer lead to the spin exchange energies

$$\begin{aligned}
 \text{FM arrangement:} & \quad -N_i N_j J_{ij} / 4 = -S_i S_j J_{ij} \\
 \text{AFM arrangement:} & \quad +N_i N_j J_{ij} / 4 = +S_i S_j J_{ij}
 \end{aligned} \tag{4}$$

Thus, the total spin exchange energy of an ordered spin arrangement is obtained by summing up all pair-wise interactions. Then, by mapping the  $N$  relative energies  $\Delta E_{\text{elec}}$  onto the  $N$  relative energies  $\Delta E_{\text{spin}}$ , we obtain the values of  $J_1 - J_N$ . In determining  $N$  spin exchanges  $J_1, J_2, \dots, J_N$ , one may employ more than  $N+1$  ordered spin states, hence obtaining more than  $N$  relative energies  $\Delta E_{\text{elec}}$  and  $\Delta E_{\text{spin}}$  for the mapping.<sup>5</sup> In this case, the  $N$  parameters  $J_1 - J_N$  can be determined by performing least-squares fitting analysis. In comparing the relative

strengths of spin exchange parameters  $J_{ij}$  involving spin sites with different numbers of unpaired spins, it is necessary to use the effective spin exchange parameters  $J_{ij}^{\text{eff}}$  that incorporate the values of the associated spins  $S_i$  and  $S_j$ , namely,

$$J_{ij}^{\text{eff}} = S_i S_j J_{ij} \quad (5)$$

The energy-mapping method described above is objective in that, once a set of spin exchange paths is chosen for a magnetic solid, it does not presume whether the associated spin exchange parameters should be FM or AFM. This method simply maps the electronic energy spectrum of DFT+U calculations onto the energy spectrum of the spin Hamiltonian defined by a set of spin exchange parameters. However, the values of the resulting spin exchange parameters depend on what set of exchange paths one selects. In identifying the spin lattice appropriate for a magnetic solid under consideration, therefore, energy-mapping analysis should be carried out for a set of spin exchange paths large enough to include all important ones. In particular, for magnetic solids consisting of both M-O-M and M-O...O-M spin exchange paths, those M-O...O-M paths with short O...O contact distances should not be omitted in the energy-mapping analysis.

When a set of spin exchange parameters are evaluated by performing DFT+U calculations as a function of  $U$ , it is generally found that the values of AFM spin exchanges become smaller in magnitude with increasing  $U$ .<sup>11c,12a,13</sup> For magnetic systems with well localized electrons, for which increasing  $U$  does not increase the moment on each spin site, this is expected because the AFM component  $J_{\text{AF}}$  of a spin exchange decreases in strength with increasing the effective on-site repulsion  $U^{\text{eff}}$ , i.e.,  $J_{\text{AF}} = -(\Delta e)^2/U^{\text{eff}}$ . Given several sets

of spin exchange parameters calculated for a magnetic solid from DFT+U calculations with various U values, the relative strengths of the spin exchange parameters are not strongly affected by U, hence predicting an identical spin lattice for the magnetic system. To check the proper range of U values, one may calculate the Curie-Weiss temperature  $\theta$  in the mean-field approximation, which is given by <sup>14</sup>

$$\theta = \frac{S(S+1)}{3k_B} \sum_i z_i J_i, \quad (6)$$

where the summation runs over all nearest neighbors of a given spin site,  $z_i$  is the number of nearest neighbors connected by the spin exchange parameter  $J_i$ , and  $S$  is the spin quantum number of each spin site.

### **2.2.c. Dependence of spin exchange parameters on crystal structure<sup>1</sup>**

In extracting the spin exchange parameters of a given magnetic solid, DFT+U calculations for all ordered spin states employ a crystal structure determined typically for its low-energy magnetic state. For most practical purposes, the use of a frozen crystal structure for all ordered spin states (ranging from low- to high-energy magnetic states) is reasonable because spin exchange interactions are weak so that the energy difference between low- and high-energy magnetic states is small. However, it should be noticed that the crystal structure of a high-energy magnetic state may differ, though slightly, from that of a low-energy magnetic state. If the crystal/electronic structure of a high-energy magnetic state is relaxed, the energy of this state should be lower when calculated for the relaxed structure than for the unrelaxed structure (i.e., the structure of a low-energy magnetic state).

An interesting situation occurs when a solid with AFM ground state is forced to adopt the FM state under strong magnetic field. As an example, consider a 2D square antiferromagnet described by the nearest-neighbor AFM spin exchange  $J$ . Then, the energy per site of the AFM state is given by  $2J$ , and that of the FM state by  $-2J$  (**Fig. 2.4**). When forced to be in the FM state under magnetic field, this antiferromagnet can lower the energy of the FM state by relaxing its crystal/electronic structure such that the spin exchange is weakened from  $J$  to a new value  $J'$  (namely,  $|J'| < |J|$ ) (**Fig. 2.5**).<sup>15</sup> Then, the energy of the FM state will be lowered from  $-2J$  to  $-2J'$ . For an AFM spin exchange,  $J \propto -t^2$  because  $\Delta e \propto t$ . This means that the relaxation of the crystal/electronic structure of the FM state must be such that the hopping integral is reduced from  $t$  to a smaller value  $t'$ .<sup>15</sup>

### 2.2.d. Spin frustration<sup>1</sup>

The spin Hamiltonian, Eq. 1, expresses the total energy of a magnetic system as a sum of pair-wise spin exchange interactions. Each individual term  $-J_{ij}\hat{S}_i \cdot \hat{S}_j$  forces the spins  $\vec{S}_i$  and  $\vec{S}_j$  to be collinear; the energy-lowering is maximum when the two spins are antiparallel and parallel if  $J_{ij}$  is AFM ( $J_{ij} < 0$ ) and FM ( $J_{ij} > 0$ ), respectively. A collinear spin arrangement is energetically unfavorable for a certain spin lattice composed of several different spin exchange paths, if the spin lattice generates either triangular or linear spin frustration. An archetypal example of triangular spin frustration is found for a triangular lattice made up of nearest-neighbor AFM spin exchange paths (**Fig. 2.6a**),<sup>16,17</sup> and the minimum-energy spin configuration for such a triangle is given by a non-collinear configuration (**Fig. 2.6b**).

It should be noted that the non-collinearity dictated by spin frustration deals only with the relative spin arrangement, and has nothing to say about the preferred spin orientation in space. What determines the preferred spin orientation in space is spin-orbit coupling (SOC)<sup>18</sup> and/or magnetic dipole-dipole (MDD)<sup>19</sup> interaction, which will be discussed in the next section. The electronic structures of non-collinear magnetic states are described by non-collinear spin-polarized DFT+U calculations.

For an AFM system with spin frustration, its Curie-Weiss temperature  $\theta$  is large in magnitude compared with its Néel temperature  $T_N$  (i.e., the 3D AFM ordering temperature). Some extent of spin frustration exists in most AFM systems, so that  $T_N$  is typically lower than  $|\theta|$ . Experimentally, an AFM system with the ratio  $f = |\theta|/T_N$  greater than 6 is often

regarded as spin frustrated.<sup>16</sup> For a magnetic system with high degree of spin frustration, its magnetic ground state is highly degenerate because a large number of different spin arrangements have the same energy. On lowering the temperature, such a system tends to lower its energy by undergoing a slight structural distortion and hence reducing the extent of spin frustration.

## 2.3 Spin-orbit coupling, uniaxial magnetism and magnetic dipole-dipole interactions

### 2.3.1. Spin-orbit coupling and spin orientation in space<sup>1</sup>

The SOC of a magnetic ion is discussed in terms of the Hamiltonian

$$\hat{H}_{\text{SOC}} = \lambda \hat{L} \cdot \hat{S}, \quad (7)$$

where  $\lambda$  is the SOC constant of the ion, and  $\hat{L}$  and  $\hat{S}$  are the orbital and spin angular momentum operators of the magnetic ion, respectively. For a transition-metal ion with lower than  $d^5$  electron count,  $\lambda > 0$ , so the orbital and spin moments couple antiparallel to each other to produce the lowest-energy angular momentum state  $J = -L + S$ . For a transition-metal ion with higher than  $d^5$  electron count,  $\lambda < 0$ , so the orbital and spin moments couple parallel to each other to produce the lowest-energy angular momentum state  $J = L + S$ . For a high-spin  $d^5$  metal ion,  $L = 0$ , to a first approximation (i.e., in the sense of free transition-metal ion), so the effect of SOC is expected to be weak. The  $\lambda$  value of an  $nd$  transition-metal ion  $M^{n+}$  increases in the order  $3d < 4d < 5d$ , and increases also with increasing its oxidation state.<sup>18</sup>

To understand how SOC works, it is necessary to consider the general expression of  $\hat{\mathbf{L}} \cdot \hat{\mathbf{S}}$  in which the preferred spin direction  $z'$  is allowed to differ from the orbital  $z$ -direction, that is,<sup>18,20</sup>

$$\begin{aligned} \hat{\mathbf{L}} \cdot \hat{\mathbf{S}} &= \hat{\mathbf{S}}_{z'} \left( \hat{\mathbf{L}}_z \cos \theta + \frac{1}{2} \hat{\mathbf{L}}_+ e^{-i\phi} \sin \theta + \frac{1}{2} \hat{\mathbf{L}}_- e^{i\phi} \sin \theta \right) \\ &+ \frac{1}{2} \hat{\mathbf{S}}_{z'} \left( -\hat{\mathbf{L}}_z \sin \theta - \hat{\mathbf{L}}_+ e^{-i\phi} \sin^2 \frac{\theta}{2} + \hat{\mathbf{L}}_- e^{i\phi} \cos^2 \frac{\theta}{2} \right), \\ &+ \frac{1}{2} \hat{\mathbf{S}}_{-z'} \left( -\hat{\mathbf{L}}_z \sin \theta + \hat{\mathbf{L}}_+ e^{-i\phi} \cos^2 \frac{\theta}{2} - \hat{\mathbf{L}}_- e^{i\phi} \sin^2 \frac{\theta}{2} \right) \end{aligned} \quad (8)$$

where the preferred orientation of the spin  $z'$  axis is defined by the polar angles  $\theta$  and  $\phi$  of the orbital Cartesian coordinate system  $(x, y, z)$  (**Fig. 2.7**). For a magnetic solid made up of  $\text{MO}_m$  polyhedra, the SOC allows the up-spin or down-spin occupied d-levels  $i$  ( $\psi_o \uparrow$  and  $\psi_o \downarrow$ , respectively) to interact with the up-spin or down-spin unoccupied d-levels  $j$  ( $\psi_u \uparrow$  and  $\psi_u \downarrow$ , respectively) via the matrix element  $\langle i | \hat{\mathbf{H}}_{\text{soc}} | j \rangle$ . The energy lowering associated with  $\langle i | \hat{\mathbf{H}}_{\text{soc}} | j \rangle$  depends on the polar angles  $\theta$  and  $\phi$ , so that the SOC determines the preferred direction of the spin (more precisely speaking, the preferred direction of the moment  $\vec{\mu}$ ) at the magnetic ion. The moment  $\vec{\mu}$  is related to the spin and orbital momenta ( $\vec{\mathbf{S}}$  and  $\vec{\mathbf{L}}$ , respectively) as

$$\vec{\mu} = -(\vec{\mathbf{L}} + g\vec{\mathbf{S}})\mu_B / \hbar, \quad (9)$$

where  $g$  is the electron  $g$ -factor (i.e., 2.0023) and  $\mu_B$  is the Bohr magneton. In addition, it should be noted that the SOC can lift the d-level degeneracy determined from DFT+U calculations.

To determine the easy-axis direction of a magnetic solid on the basis of DFT

calculations, its total energy including SOC interactions should be calculated as a function of the spin direction.<sup>21</sup> Then, the easy-axis direction is the spin direction with the lowest total energy. Experimentally, neutron diffraction refinements at a very low temperature provide information about the magnitudes and orientations of the moments at the spin sites of a magnetic solid.

### 2.3.2. Uniaxial magnetism<sup>1</sup>

A magnetic system with uniaxial magnetism has a nonzero magnetic moment only along one direction in space.<sup>22,23</sup> The consideration of the crystal field and SOC effects shows that, for a system with transition-metal magnetic ions to have uniaxial magnetic properties, the following three conditions should be satisfied.<sup>22</sup>

(a) The site symmetry of the transition-metal ion should have an  $n$ -fold rotational symmetry with  $n \geq 3$ , so that its d-levels have degenerate sets, i.e.,  $\{x^2-y^2, xy\}$  and  $\{xz, yz\}$  with the  $z$ -axis taken along the rotational axis.

(b) The d-electron count of the transition-metal ion should be such that one of the two degenerate d-states is occupied by three electrons, and hence the ground state of the ion is described by two degenerate electronic configurations with nonzero orbital angular momentum. As a representative example, **Fig. 2.8** shows the two degenerate electronic configurations of  $(\text{Me}_3\text{Si})_3\text{C-Fe-C}(\text{SiMe}_3)_3$ , in which the C-Fe-C frame is linear and the Fe atom exists as a high-spin  $\text{Fe}^{2+}$  ( $d^6$ ) ion.

(c) The d-states should be more than half filled so that the SOC constant is negative ( $\lambda < 0$ ).

Then, in the ground state arising from the SOC interaction  $\lambda\vec{L}\cdot\vec{S}$ ,  $\vec{L}$  and  $\vec{S}$  become parallel to each other so that the  $J = L + S$  value is large, and the  $\Delta J_z$  values becomes greater than 1 (note that  $J_z = \pm J$ ). It is important to note that the electronic structure required for uniaxial magnetism is also the condition leading to Jahn-Teller (JT) instability. The latter refers to the tendency of a system with degenerate electronic states to undergo a geometrical distortion that removes the degeneracy of the electronic state.<sup>24</sup> Thus, the JT distortion of a system with uniaxial magnetism will remove the n-fold ( $n \geq 3$ ) rotational symmetry that is responsible for the uniaxial magnetism to begin with. In other words, uniaxial magnetism and JT instability are incompatible, unless JT distortion is prevented by steric hindrance as in  $(\text{Me}_3\text{Si})_3\text{C-Fe-C}(\text{SiMe}_3)_3$ .<sup>23</sup> It is of interest to examine how these opposing factors compete in systems with no strong steric hindrance.

### 2.3.3. Magnetic dipole-dipole interactions<sup>1</sup>

The spin exchange, SOC and DM interactions are short-range interactions, whereas the MDD interaction is a long-range interaction. The MDD interaction is weak, being of the order of 0.1 meV for two spin-1/2 ions separated by 2 Å, but is responsible for the formation of various FM domains in an FM material. Given that two spins located at sites i and j are described by the distance  $r_{ij}$  with the unit vector  $\vec{e}_{ij}$  along the distance, the MDD interaction is described by<sup>19</sup>

$$\left(\frac{g^2\mu_B^2}{a_0^3}\right)\left(\frac{a_0}{r_{ij}}\right)^3 \left[ -3(\vec{S}_i \cdot \vec{e}_{ij})(\vec{S}_j \cdot \vec{e}_{ij}) + (\vec{S}_i \cdot \vec{S}_j) \right] \quad , \quad (10)$$

where  $a_0$  is the Bohr radius (0.529177 Å), and  $(g\mu_B)^2/(a_0)^3 = 0.725$  meV.

In discussing the 3D magnetic order and the spin orientation of a magnetic solid, the MDD interaction is often neglected. However, this interaction can become non-negligible especially when the spin  $S$  of a magnetic ion is large, because the MDD interaction is proportional to  $S^2$ .<sup>25</sup> The MDD effect on the preferred spin orientation of a given magnetic solid can be examined by comparing the MDD interaction energies calculated for a number of ordered spin arrangements. In summing the MDD interactions between various pairs of spin sites, it is convenient to employ the Ewald summation method.<sup>26</sup>

## 2.4. Computational methods

### 2.4.1. Density functional theory

In our work, we have applied Density functional theory (DFT) to analyze the electronic structures. In quantum mechanics,<sup>27</sup> the electronic structure of a many-electron system is described by the Schrödinger equation

$$\hat{H}\Psi(\vec{r},\vec{R}) = E\Psi(\vec{r},\vec{R}), \quad (11)$$

where  $\hat{H}$  is Hamiltonian. In the Born-Oppenheimer approximation, the Hamiltonian is written as,<sup>27</sup>

$$\hat{H}(\mathbf{r},\mathbf{R}) = -\sum_i \frac{\hbar}{2m_e} \nabla_i^2 + \frac{1}{2} \sum_j \sum_{i \neq j} \frac{e^2}{|\mathbf{r}_i - \mathbf{r}_j|} - \sum_\alpha \sum_i \frac{Ze^2}{|\mathbf{r}_i - \mathbf{R}_\alpha|}, \quad (12)$$

which describe the electronic kinetic energy, electron-electron repulsion and electron-nuclear attraction. Describing an interacting system of electrons via its electron density  $\rho$  instead of calculating its wave function is the main idea of DFT. Hohenberg and Kohn<sup>28</sup> proved that for a system with nondegenerate ground state, the ground-state energy  $E_0$  is uniquely determined by the ground-state electron density  $\rho_0(x,y,z)$ . The ground-state electronic energy  $E_0$  is a function of  $\rho_0$ , namely,  $E_0 = E_0[\rho_0]$ . According to the Hohenberg-Kohn theorem, the ground-state electronic wave function  $\psi_0$  of a many-electron system is an eigenfunction of the purely electronic Hamiltonian  $\hat{H}$ ,

$$\hat{H} = -\frac{\hbar^2}{2m} \sum_i \nabla_i^2 + \sum_i v_{\text{ext}}(\mathbf{r}_i) + \frac{1}{2} \sum_j \sum_{i \neq j} \frac{e^2}{|\mathbf{r}_i - \mathbf{r}_j|}, \quad (13)$$

where  $v_{\text{ext}}(\mathbf{r}_i)$  is the external potential acting on the electron  $i$ .

### 2.4.2. Exchange-correlation energy functionals

The exact expression of the exchange-correlation functional is not known except for the free electron gas, which is the major problem with DFT. However, one can get approximate expressions that permit the calculation of certain physical quantities quite accurately. In this article, the generalized-gradient approximation (GGA)<sup>28</sup> of Perdew, Burke and Ernzerhof<sup>29</sup> were used as the exchange-correlation functionals. The GGA depends on the local density and its gradient as,<sup>28</sup>

$$E_{xc}^{GGA} = [\rho^\alpha, \rho^\beta] = \int f(\rho^\alpha(\vec{r}), \rho^\beta(\vec{r}), \nabla\rho^\alpha(\vec{r}), \nabla\rho^\beta(\vec{r}))d(\vec{r}), \quad (14)$$

### 2.4.3. Program package employed and on-site repulsion U

In our calculations of the electronic structures for solid-state magnetic oxides, we employed the frozen-core projector augmented wave<sup>30</sup> method encoded in the Vienna Ab-initio Simulation Package (VASP).<sup>31</sup> For magnetic solids containing typically 3d transition metals, DFT calculations with GGA invariably predict metallic electronic structures (i.e., electronic structure with partially filled bands) even if spin-polarized DFT calculations are performed. To remove this deficiency of DFT calculations, one typically employs the DFT plus on-site repulsion U (i.e. DFT+U) method,<sup>32,33</sup> in which U of certain value is added to the transition metal atoms to ensure a large split between their up-spin and down-spin d-states so that the resulting electronic structure has a band gap. It is noted that DFT+U calculations are empirical because the choice of U is empirical. In our report, DFT+U calculations with GGA are referred to as GGA+U<sup>34</sup> calculations, respectively. In addition, when these calculations include SOC effects,<sup>35</sup> they are referred to as GGA+U+SOC calculations, respectively.

## References

1. Xiang, H. J.; Lee, C.; Koo, H. -J.; Gong X. G.; Whangbo, M. -H. *Dalton Trans.*, **2013**, 42, 823.
2. Mott, N. F., *Metal-Insulator Transitions*, 2nd ed.; Taylor & Francis: London, 1990.
3. Whangbo, M. -H., *J. Chem. Phys.* **1979**, 70, 4963.
4. Dudarev, S. L.; Botton, G. A.; Savrasov, S. Y.; Humphreys, C. J.; Sutton, A. P. *Phys. Rev. B* **1998**, 57, 1505.
5. Whangbo, M.-H.; Koo, H.-J.; Dai, D., *J. Solid State Chem.* **2003**, 176, 417.
6. Hay, P. J.; Thibeault, J. C.; Hoffmann, R., *J. Am. Chem. Soc.* **1975**, 97, 4884.
7. Koo, H. -J.; Whangbo, M. -H., *Inorg. Chem.* **2006**, 45, 4440.
8. (a) Dai, D.; Koo, H. -J.; Whangbo, M. -H., *Inorg. Chem.* **2004**, 43, 4026. (b) Koo, H. -J.; Lee, C.; Whangbo, M.-H.; McIntyre, G. J.; Kremer, R. K., *Inorg. Chem.*, in press.
9. Tian, C.; Wibowo, A. C.; zur Loye, H. -C.; Whangbo, M. -H., *Inorg. Chem.*, in press.
10. (a) Dai, D.; Whangbo, M.-H. *J. Chem. Phys.* **2001**, 114, 2887. (b) Dai, D.; Whangbo, M.-H. *J. Chem. Phys.* **2003**, 118, 29.
11. (a) Miura, Y.; Hirai, R.; Kobayashi, Y.; Sato, M., *J. Phys. Soc. Jpn.* **2006**, 75, 84707. (b) Derakhshan, S.; Cuthbert, H. L.; Greedan, J. E.; Rahman, B.; Saha-Dasgupta, T., *Phys. Rev. B* **2007**, 76, 104403. (c) Koo, H. -J.; and Whangbo, M. -H., *Inorg. Chem.* **2008**, 47, 128. (d) Sakurai, H.; Yoshimura, K.; Kosuge, K.; Tsujii, N.; Abe, H.; Kitazawa, H.; Kido, G.; Michor, H.; Hilscher, G., *J. Phys. Soc. Jpn.* **2002**, 71, 1161.
12. (a) Sakurai, H.; Yoshimura, K.; Kosuge, K.; Tsujii, N.; Abe, H.; Kitazawa, H.; Kido, G.; Michor, H.; Hilscher, G., *J. Phys. Soc. Jpn.* **2002**, 71, 1161. (b) Okamoto, K.; Tonegawa,

- T.; Kaburagi, M., *J. Phys. Condens. Matter* **2003**, *15*, 5979. (c) Koo, H. -J.; Whangbo, M. -H., *Inorg. Chem.* **2008**, *47*, 4779.
13. Xiang, H. J.; Lee, C.; Whangbo, M.-H. *Phys. Rev. B* **2007**, *76*, 220411(R).
  14. Smart, J. S.; *Effective Field Theory of Magnetism*: Saunders, Philadelphia, 1966.
  15. Musfeldt, J. L.; Vergara, L. I.; Brinzari, T. V.; Lee, C.; Tung, L. C.; Kang, J.; Wang, Y. J.; Schlueter, J. A.; Manson, J. L.; Whangbo, M. -H., *Phys. Rev. Lett.* **2009**, *103*, 157301.
  16. Greedan, J. E., *J. Mater. Chem.* **2001**, *11*, 37, and the references cited therein.
  17. Dai, D.; Whangbo, M.-H., *J. Chem. Phys.* **2004**, *121*, 672.
  18. Dai, D.; Xiang, H. J.; Whangbo, M. -H., *J. Comput. Chem.* **2008**, *29*, 2187.
  19. Koo, H.-J. X., H.; Lee, C.; Whangbo, M-H., *Inorg. Chem.* **2009**, *48*, 9051.
  20. Wang, X.; Wu, R.; Wang, D.-S.; Freeman, A. J., *Phys. Rev. B* **1996**, *54*, 61.
  21. Kunes 2001: Kuneš, J.; Novák, P.; Diviš, M.; Oppeneer, P. M. *Phys Rev B* **2001**, *63*, 205111.
  22. Dai, D.; Xiang, H. J.; Whangbo, M. -H., *J. Comput. Chem.* **2008**, *29*, 2187.
  23. Dai, D.; Whangbo, M.-H., *Inorg. Chem.* **2005**, *44*, 4407.
  24. Jahn, H. A.; Teller, E. *Proc. Roy. Soc. A* **1937**, *161*, 220.
  25. Bramwell, S. T.; Gingras, M. J. P., *Science* **2001**, *294*, 1495.
  26. (a) Ewald, P. P., *Ann. Phys.* **1921**, *64*, 253. (b) Darden, T.; York, D.; Pedersen, L., *J. Chem. Phys.* **1993**, *98*, 10089.. (c) Wang, H.; Dommert, F.; Holm, C., *J. Chem. Phys.* **2010**, *133*, 034117.
  27. Zeng, J *Quantum Mechanics*, Kexue press, Beijing, **2000**.

28. Levine, I. N. *Quantum Chemistry*, Prentice-Hall, India, **2006**.
29. Perdew, J. P.; Burke, K.; Ernzerhof, M., Generalized Gradient Approximation Made Simple. *Phys. Rev. Lett.* **1996**, 77 (18), 3865.
30. Kresse, G.; Joubert, D., From ultrasoft pseudopotentials to the projector augmented-wave method. *Phys. Rev. B: Condens. Matter* **1999**, 59 (3), 1758.
31. (a) Kresse, G.; Hafner, J., Ab initio molecular dynamics for liquid metals. *Phys. Rev. B: Condens. Matter* **1993**, 47 (1), 558. (b) Kresse, G.; Furthmüller, J., *Efficiency of abinitio total energy calculations for metals and semiconductors using a plane-wave basis set. Comput. Mater. Sci.* **1996**, 6 (1), 15. (c) Kresse, G.; Furthmüller, J., *Efficient iterative schemes for ab initio total-energy calculations using a plane-wave basis set. Phys. Rev. B: Condens. Matter* **1996**, 54 (16), 11169.
32. Anisimov, V. I.; Aryasetiawan, F.; Lichtenstein, A. I. *J. Phys.: Condensed Matter* **1997**, 9, 767.
33. Dudarev, S. L.; Botton, G. A.; Savrasov, S. Y.; Humphreys, C. J.; Sutton, A. P. *Phys. Rev. B* **1998**, 57, 1505.
34. Dudarev, S. L.; Botton, G. A.; Savrasov, S. Y.; Humphreys, C. J.; Sutton, A. P., *Electronenergy-loss spectra and the structural stability of nickel oxide: An LSDA+U study. Phys. Rev. B: Condens. Matter* **1998**, 57 (3), 1505.
35. Kuneš, J.; Novák, P.; Diviš, M.; Oppeneer, P. M. *Phys Rev B* **2001**, 63, 205111.

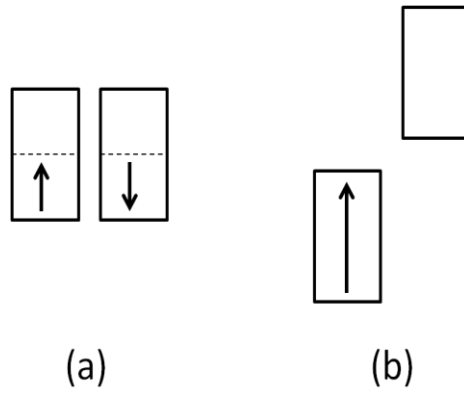


**Fig. 2.1** Two electronic states that a system with a half-filled band can have: (a) Non-magnetic metallic state, in which both the up-spin and down-spin states are half-filled. (b) Magnetic insulating state, in which the up-spin band is completely filled, but the down-spin band, separated from the up-spin band by a band gap, is empty.

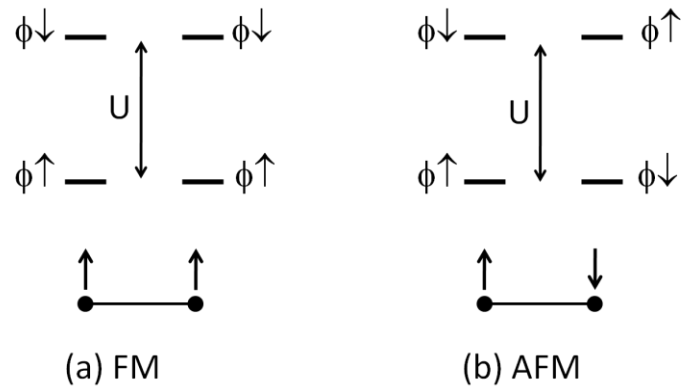


**Fig. 2.2** Split patterns of the up-spin and down-spin levels ( $\phi\uparrow$  and  $\phi\downarrow$ , respectively) for the two extreme cases of spin arrangements for a 1D chain with one orbital per site: (a) FM state in which all sites have up-spins. (b) AFM state in which up-spin and down-spin sites alternate. Only two adjacent spin sites of the chain are shown for simplicity.

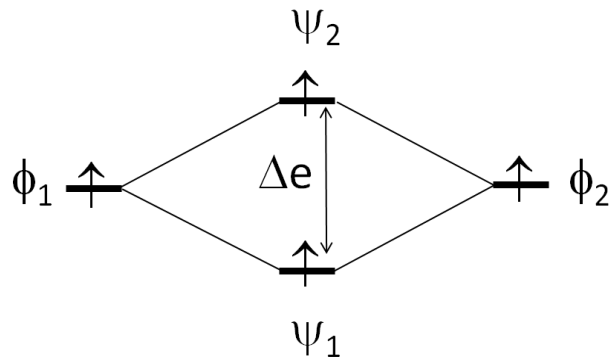


**Fig. 2.3** Orbital interaction between two spin sites described by the magnetic orbitals  $\phi_1$  and  $\phi_2$  leading to the dimer levels  $\psi_1$  and  $\psi_2$  separated by the energy gap  $\Delta e$ .

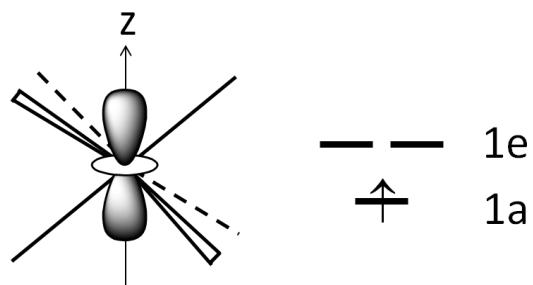


**Fig. 2.4** Weak JT distortion of a  $\text{MO}_6$  octahedron with  $(t_{2g})^1$  configuration leading to a distorted  $\text{MO}_6$  octahedron with  $C_3$ -rotational symmetry. This distortion splits the  $t_{2g}$  level into the pattern of  $1a < 1e$  pattern, where the  $1a$  level is described by the  $z^2$  orbital, when the local  $z$ -axis is taken along the  $C_3$ -rotational axis.

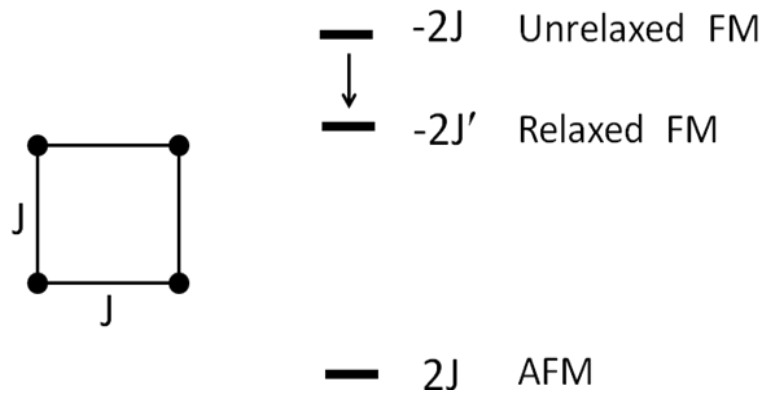


**Fig. 2.5** Energies of the AFM, the unrelaxed FM and the relaxed FM states of a 2D square-lattice antiferromagnet described by the nearest-neighbor AFM spin exchange  $J$  ( $< 0$ ). The relaxed FM state is described by a new nearest-neighbor spin exchange  $J'$  for which  $|J'| < |J|$ .

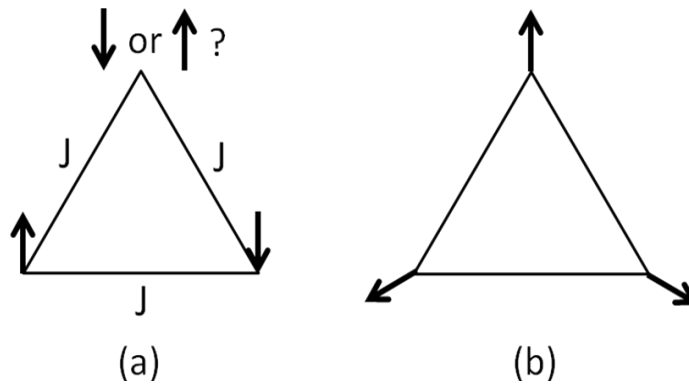


**Fig. 2.6** Triangular spin frustration and non-collinear spin arrangement in a triangle of spin sites described by the nearest-neighbor AFM spin exchange  $J$  ( $< 0$ ): (a) Spin frustration that occurs when the spins are collinear. (b) Compromised non-collinear spin arrangement that minimizes the total spin exchange interactions.

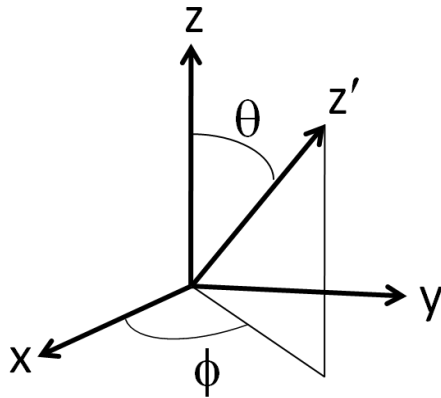


**Fig. 2.7** Two coordinate systems used to describe the spin-orbit coupling  $\hat{H}_{\text{SOC}} = \lambda \hat{L} \cdot \hat{S}$ , where the spin  $z'$ -axis (i.e., the preferred spin direction) is defined in terms of the angles ( $\theta$ ,  $\phi$ ) with respect to the Cartesian coordinate system describing the orbital angular momentum.

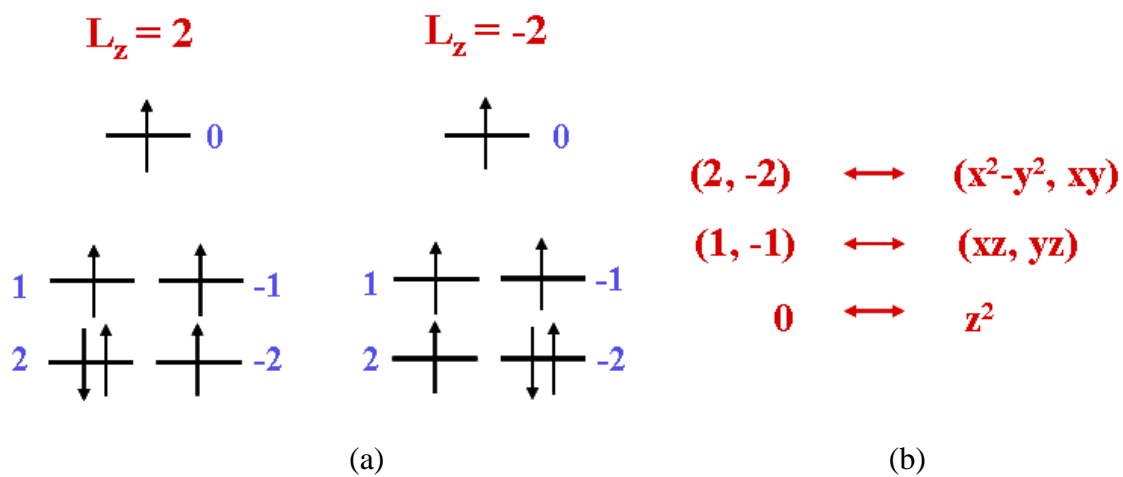


**Fig. 2.8** (a) Two degenerate electron configurations of  $(\text{Me}_3\text{Si})_3\text{C-Fe-C}(\text{SiMe}_3)_3$  containing a high-spin  $\text{Fe}^{2+}$  ( $d^6$ ) ion in the linear two-coordinate site. (b) Correspondence between the Cartesian and the spherical-harmonics representations for the split d-states of the linear-two coordinate  $\text{Fe}^{2+}$  ( $d^6$ ) ion.

### 3. Spin exchange interactions and magnetic structure of $\text{FeTe}_3\text{O}_7\text{X}$ ( $\text{X} = \text{Cl}, \text{Br}$ )<sup>1</sup>

The two isostructural compounds  $\text{FeTe}_3\text{O}_7\text{Cl}$  (**1**) and  $\text{FeTe}_3\text{O}_7\text{Br}$  (**2**) crystallize in the monoclinic system, space group  $P2_1/c$ .  $\text{FeTe}_3\text{O}_7\text{X}$  ( $\text{X} = \text{Cl}, \text{Br}$ ) is made up of covalently bonded Fe-Te-O slabs with halide ions located between them so that only weak van der Waal interactions are present between adjacent Fe-Te-O slabs. A projection view of the Fe-Te-O slabs and halide ions along the  $b$ -axis is shown in **Fig. 3.1a**. There is one kind of crystallographically unique  $\text{Fe}^{3+}$  cations forming distorted  $\text{FeO}_5$  trigonal bipyramids, which share their edges to form  $\text{Fe}_2\text{O}_8$  dimer units (**Fig. 3.2**). In each Fe-Te-O slab the  $\text{Fe}_2\text{O}_8$  dimers are well isolated by the Te-O framework made up of corner-sharing  $\text{TeO}_4$  and  $\text{TeO}_3$  units containing  $\text{Te}^{4+}$ -cations (**Fig. 3.1b**). The halide ions are not considered as fully integrated into the covalent Fe-Te-O network but act more as counter anions as found in other oxohalides such as  $(\text{TeO}_3)_6\text{Cl}_2$  and  $\text{Fe}_3(\text{TeO}_3)_3\text{OCl}$ .<sup>2,3</sup>

Experimentally, the magnetic susceptibilities of **1** and **2** are characterized by a broad maximum at about  $\sim 102$  K for **1** and  $\sim 94$  K for **2** (**Fig. 3.3**),<sup>1</sup> a Curie-Weiss behavior above these temperatures, and a very steep decrease below the maximum. Experimentally, these magnetic properties of the compounds are described by an isolated antiferromagnetic spin dimer model.<sup>1</sup> In order to confirm this experimental conclusion, we evaluate the spin exchange interactions of **1** and **2** by DFT calculations with the GGA. Our spin-polarized DFT calculations predict **1** and **2** to be magnetic insulating even without adding on-site repulsion  $U$  on  $\text{Fe}^{3+}$ , as can be seen from the DOS plots calculated for the ferromagnetic state of **1** (**Fig. 3.4**). Thus, we did not use the DFT+ $U$  calculations for our evaluations of the spin exchange interactions.<sup>4</sup>

For **1** and **2** we consider three spin exchange interactions  $J_1 - J_3$  defined in **Fig. 3.5**, where  $J_1$  is the intra-dimer spin exchange while  $J_2$  and  $J_3$  are inter-dimer spin exchanges. To evaluate these interactions, we determine the relative energies of the four ordered spin states, FM, AF1, AF2 and AF3, using a (a, 2b, c) supercell (**Fig. 3.6**). The relative energies of these states calculated by performing spin-polarized GGA calculations are also summarized in **Fig. 3.6**. To extract the values of  $J_1 - J_3$ , we express the total spin exchange interaction energies of the four ordered spin states in terms of the spin Hamiltonian,  $\hat{H} = -\sum_{i<j} J_{ij} \hat{S}_i \cdot \hat{S}_j$ , where  $J_{ij} = J_1 - J_3$  is the spin exchange constant for the interaction between the spins  $\hat{S}_i$  and  $\hat{S}_j$  at the sites  $i$  and  $j$ , respectively. By applying the energy expression obtained for spin dimers consisting of two spin sites with  $N$  unpaired spins (i.e.,  $N = 5$  for  $\text{Fe}^{3+}$ ), the total spin exchange energies, per supercell, i.e., per eight formula units (FUs), of the four ordered spin states are written as

$$E_{\text{FM}} = (-4J_1 - 8J_2 - 16J_3)(N^2 / 4)$$

$$E_{\text{AF1}} = (+4J_1 + 8J_2)(N^2 / 4)$$

$$E_{\text{AF2}} = (+4J_1 - 8J_2 + 16J_3)(N^2 / 4)$$

$$E_{\text{AF3}} = (-4J_1 - 8J_2 + 16J_3)(N^2 / 4)$$

Then, by mapping the relative energies of the four ordered spin states determined from GGA calculations onto the corresponding relative energies determined from the above expressions, we obtain the values of  $J_1 - J_3$  listed in **Table 3.1**. The antiferromagnetic intra-dimer exchange  $J_1$  dominates. The inter-dimer spin exchanges are weak but are not negligible. This supports the description of the magnetic properties of **1** and **2** in terms of an antiferromagnetic isolated dimer model. For **1** and **2**, the calculated  $J_1$  values are essentially

the same, and so are the inter-dimer exchange  $J_3$ . However, **1** and **2** differ mainly in the inter-dimer exchange  $J_2$ . We note that the calculated  $J_1$  values are greater than the experimental values by a factor of approximately 4.<sup>5-7</sup> In general, GGA calculations are known to overestimate spin exchange constants.

Experimentally, the magnetic properties of  $\text{FeTe}_3\text{O}_7\text{X}$  ( $\text{X} = \text{Cl}, \text{Br}$ ) are well described by an isolated antiferromagnetic spin dimer model with spin gaps of approximately 17.5 K and 15.8 K for  $\text{X} = \text{Cl}$  and  $\text{Br}$ , respectively.<sup>1</sup> High-field magnetization experiments suggest the presence of some inter-dimer interactions of the order of  $\sim 1$  K.<sup>1</sup> These observations are supported by the spin exchange interactions of  $\text{FeTe}_3\text{O}_7\text{X}$  ( $\text{X} = \text{Cl}, \text{Br}$ ) obtained from our GGA calculations.

## References

1. Zhang, D.; Kremer, R.K.; Lemmens, P.; Choi, K-Y.; Liu, J.; Whangbo, M-H.; Berger, H.; Skourski, Y.; Johnsson, M. *Inorg. Chem.* **2011**, 50, 12877-12885.
2. Becker, R.; Johnsson, M. *J. Solid State Chem.* **2007**, 180, 1750-1758.
3. Zhang, D.; Johnsson, M.; Berger, H.; Kremer, R.K.; Wulferding, D.; Lemmens, P. *Inorg. Chem.* **2009**, 48, 6599-6603.
4. Dudarev, S. L.; Botton, G. A.; Savrasov, S. Y.; Humphreys, C. J.; Sutton, A. P. *Phys. Rev. B* **1998**, 57, 1505.
5. Dai, D.; Whangbo, M.-H. *J. Chem. Phys.* **2001**, 114, 2887.
6. Dai, D.; Koo, H.-J.; Whangbo, M.-H. *J. Solid State Chem.* **2003**, 175, 341.
7. Dai, D.; Whangbo, M.-H.; Koo, H.-J.; Rocquefelte, X.; Jovic, S.; Villesuzanne, A. *Inorg. Chem.* **2005**, 44, 2407.

**Table 3.1.** Spin exchange constants (in meV) of  $\text{FeTe}_3\text{O}_7\text{Cl}$  and  $\text{FeTe}_3\text{O}_7\text{Br}$  obtained from GGA calculations

	$J_1$	$J_2$	$J_3$
$\text{FeTe}_3\text{O}_7\text{Cl}$	-6.54	+1.62	-0.83
$\text{FeTe}_3\text{O}_7\text{Br}$	-6.55	+0.62	-0.80

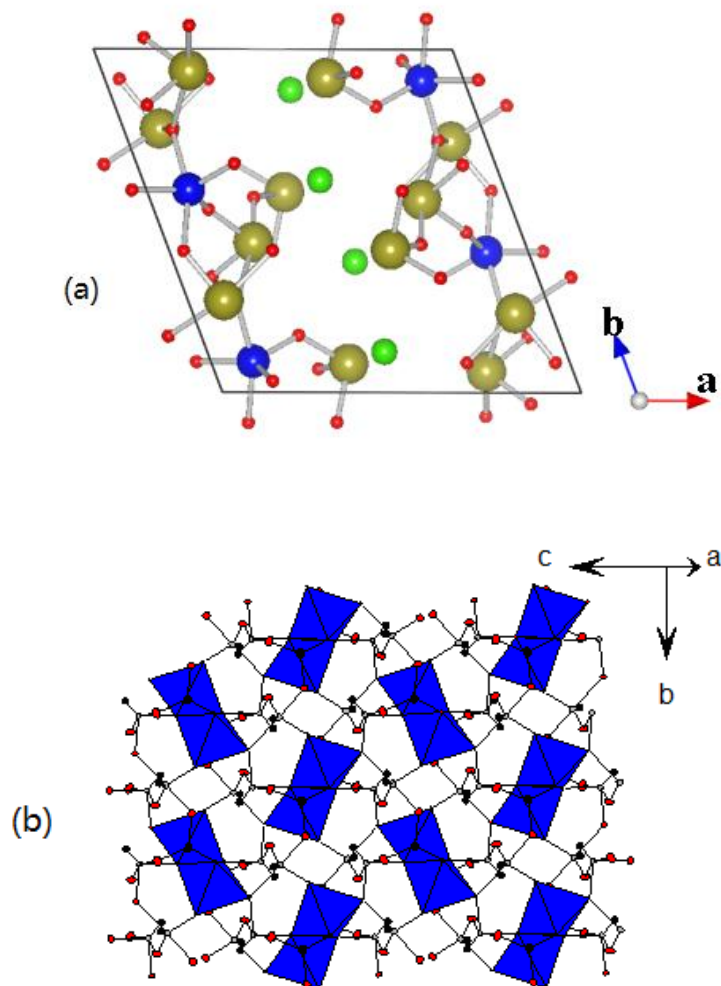
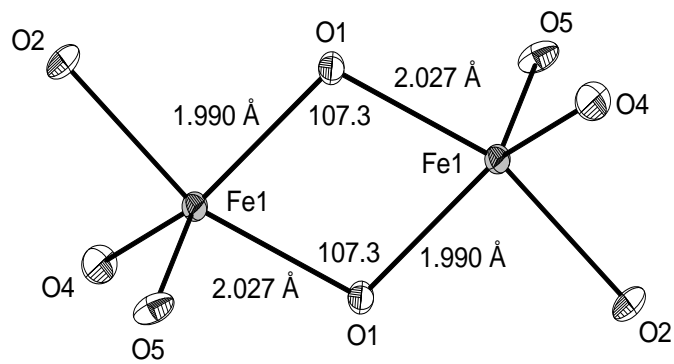
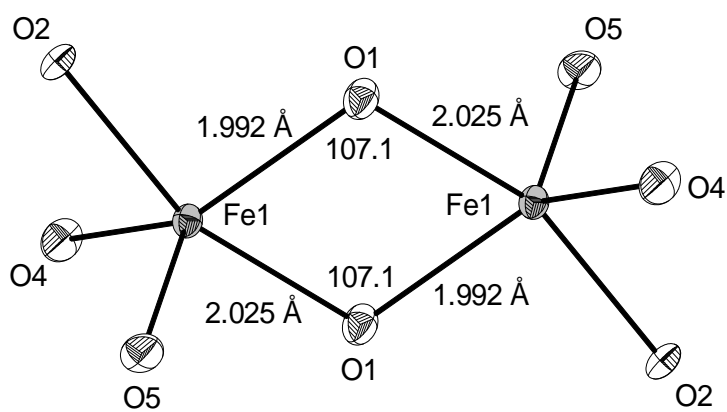


**Fig. 3.1** (a) Projection view of the crystal structure of  $\text{FeTe}_3\text{O}_5\text{X}$  ( $\text{X} = \text{Cl}, \text{Br}$ ) along b-axis, where the blue, yellow, red and green spheres represent  $\text{Fe}^{3+}$ ,  $\text{Te}^{4+}$ ,  $\text{O}^{2-}$  and  $\text{X}^-$  ions, respectively. (b) An Fe-Te-O slab showing how the  $\text{Fe}_2\text{O}_8$  dimer units (blue polyhedra) are isolated from each other by the Te (grey) and O (red) atoms. The lone pair on  $\text{Te}^{4+}$  is marked as a black circle.



(a)



(b)

**Fig. 3.2** Structures of the  $\text{Fe}_2\text{O}_8$  dimer units in (a)  $\text{FeTe}_3\text{O}_7\text{Cl}$  (1) and (b)  $\text{FeTe}_3\text{O}_7\text{Br}$  (2).

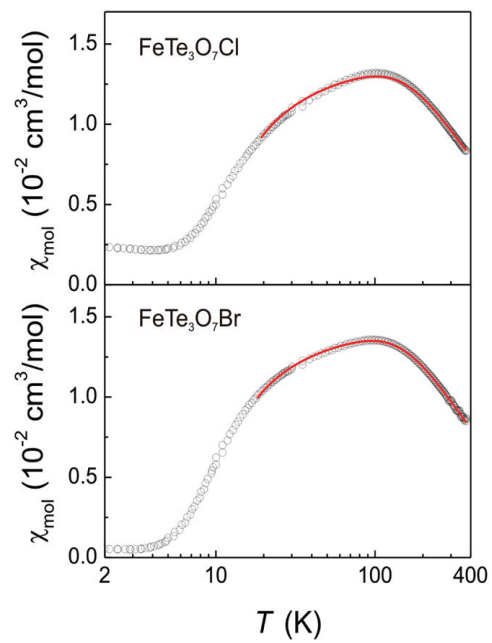


**Fig. 3.3** Magnetic susceptibilities of FeTe<sub>3</sub>O<sub>7</sub>X (X = Cl, Br) measured with a field of 0.1 T. The solid (red) lines are fits to the susceptibility of a spin dimer of Fe<sup>3+</sup> (S = 5/2) cations.

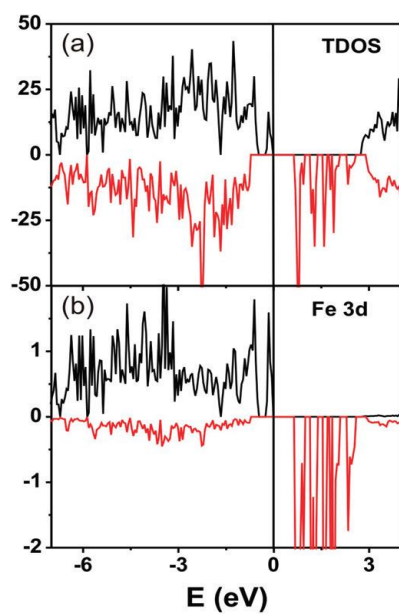


**Fig. 3.4** Spin polarized electronic density of states (states/electron FU) of FeTe<sub>3</sub>O<sub>7</sub>Cl in the FM configuration (see Fig. 12). (a) Total density of states. (b) Projected density of states of the Fe d electrons.

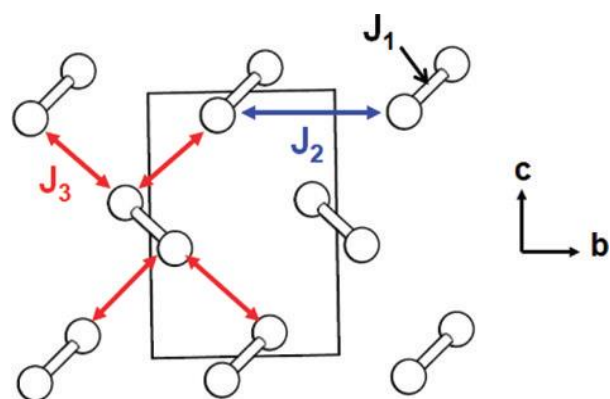


**Fig. 3.5** Definition of the three spin exchange parameters  $J_1$ (intradimer),  $J_2$ , and  $J_3$  (both interdimer) in  $\text{FeTe}_3\text{O}_7\text{X}$  ( $\text{X} = \text{Cl}, \text{Br}$ ).

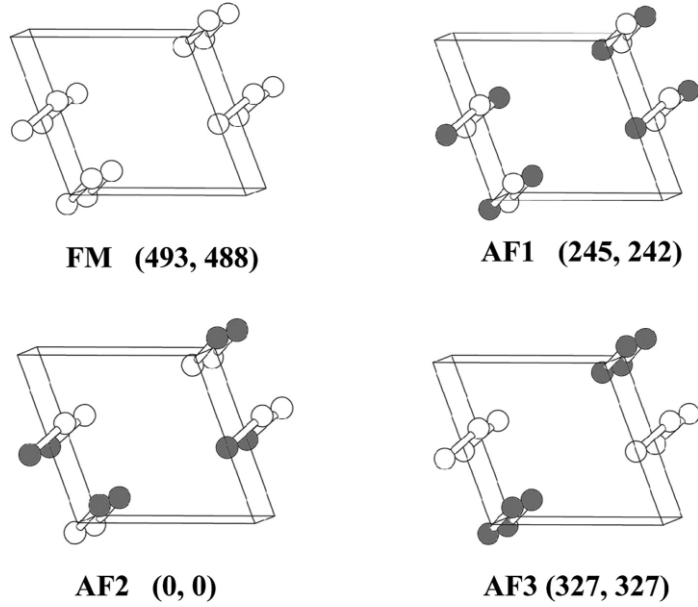


**Fig. 3.6** Four ordered spin states FM, AF1, AF2, and AF3 in a (a, 2b, c) supercell employed to extract the values of  $J_1$ ,  $J_2$ , and  $J_3$ , where only the Fe atoms are shown for simplicity. The up-spin and down-spin  $\text{Fe}^{3+}$  sites are represented by spheres of different colors. The numbers in parentheses give the relative energies (in meV) obtained from the GGA calculations with for 1 and 2, respectively.

#### 4. Magnetic structure and spin exchange interactions of $\text{Ag}_2\text{ZnZr}_2\text{F}_{14}$ <sup>1</sup>

Compounds containing  $\text{Ag}^{2+}$  ( $d^9$ ) ions are rare and have interesting magnetic properties such as the strong antiferromagnetically coupled one-dimensional (1D) chain of  $\text{Ag}^{2+}$  ions in  $\text{AgSO}_4$ ,<sup>2</sup> the two-dimensional (2D) ferromagnetic square net of  $\text{Ag}^{2+}$  ions in  $\text{Cs}_2\text{AgF}_4$ .<sup>3</sup>  $\text{Ag}_2\text{ZnZr}_2\text{F}_{14}$  was synthesized to study the magnetic properties of the discrete  $\text{Ag}_2\text{F}_7$  dimers.<sup>1</sup> This deep blue-violet colored compound crystallizes in the space group  $C2/m$  and each  $\text{Ag}^{2+}$  forms a square planar geometry with surrounding F atoms (**Fig. 4.1**). The  $\text{AgF}_4$  units form  $\text{Ag}_2\text{F}_7$  dimers by sharing a corner, which are connected by  $\text{ZnF}_6$  octahedra and  $\text{ZrF}_7$  pentagonal bipyramids to provide the 3D framework of  $\text{Ag}_2\text{ZnZr}_2\text{F}_{14}$ . The  $\text{Ag}_2\text{F}_7$  dimers are running along b-axis and result in two-leg ladders of the  $\text{Ag}^{2+}$  ions as depicted in **Fig. 4.2**.

The magnetic susceptibility of  $\text{Ag}_2\text{ZnZr}_2\text{F}_{14}$  (**Fig. 4.3**) shows that at room temperature more than ~95 % of the spins are antiferromagnetically coupled. The value of  $\chi_{\text{mol}}$  at 300 K under a field of 1 T is very small (i.e.,  $\sim 0.9 \times 10^{-4} \text{ cm}^3 \text{ mol}^{-1}$ ). Due to the thermal instability of the compound, measurements of the magnetic susceptibility at higher temperatures cannot be performed. Consequently, no useful information can be gained from experiments as to what kind of an AFM spin lattice is responsible for the very weak magnetic of  $\text{Ag}_2\text{ZnZr}_2\text{F}_{14}$  at room temperature.

In order to understand the magnetic properties of  $\text{Ag}_2\text{ZnZr}_2\text{F}_{14}$ , we determine the three spin exchange interactions, namely, the rung exchange  $J_1$  and the leg exchange  $J_2$  as well as the inter-ladder exchange  $J_3$  defined in **Fig. 4.4a**. To determine the values of  $J_1 - J_3$ , we consider the four ordered spin states AF1 – AF4 shown in **Fig. 4.4b** in terms of a (a, 2b,

c) supercell. The relative energies of these states per supercell, i.e., per eight formula units (FUs), calculated by performing GGA+U calculations are summarized in **Table 4.1**. In terms of the spin Hamiltonian,  $\hat{H} = -\sum_{i<j} J_{ij} \hat{S}_i \cdot \hat{S}_j$ , where  $J_{ij}$  ( $= J_1 - J_3$ ) is the spin exchange constant for the interaction between the sites  $i$  and  $j$ ,<sup>4</sup> the total spin exchange energies, per eight formula FUs, of the three ordered spin states are written as

$$E_{AF_1} = (4J_1 - 8J_2 + 8J_3)(1/4)$$

$$E_{AF_2} = (-4J_1 + 8J_2)(1/4)$$

$$E_{AF_3} = (4J_1 + 8J_2)(1/4)$$

$$E_{AF_4} = (4J_1 - 8J_2 - 8J_3)(1/4)$$

Thus, by mapping the relative energies of the four ordered spin states determined from GGA+U calculations onto the corresponding relative energies determined from the above expressions, we obtain the values of  $J_1 - J_3$  listed in **Table 4.2**. Clearly, the rung exchange  $J_1$  dominates over the leg exchange  $J_2$  and the inter-ladder exchange  $J_3$  for all values  $U = 2 - 6$  eV. To a first approximation, therefore, the magnetic properties of  $Ag_2ZnZr_2F_{14}$  can be described by an isolated antiferromagnetic dimer.

## References

1. Tong, J.W.; Kraus, F.; Köhler, J.; Simon, A; Liu, J.; Whangbo, M-H. *Z. Anorg. Allg. Chem.* **2011**, *637*, 1118-1121.
2. a) P. J. Malinowski, M. Derzsi, Z. Mazej, Z. Jaglicic, B. Gawel, W. Lasocha, W. Grochala, *Angew. Chem. Int. Ed. Engl.* **2010**, *49*, 1683-1686. b) M. Derzsi, K. Dymkowski, W. Grochala, *Inorg. Chem.* **2010**, *49*, 2735-2742. c) J. Köhler, *Angew. Chem. Int. Ed. Engl.* **2010**, *49*, 3114-3115.
3. a) R. H. Odenthal, D. Paus, R. Hoppe, *Z. Anorg. Allg. Chem.* **1974**, *407*, 144-150. b) S. E. McLain, D.A. Tennant, J. F. C. Turner, T. Barnes, M. R. Dolgos, T. Proffen, B. C. Sales and R. I. Bewley, *Nature Materials* **2006**, *5*, 561-565. c) D. Dai, M.-H. Whangbo, J. Köhler, C. Hoch, A. Villesuzanne, *Chem. Mat.* **2006**, *18*, 3281-3286. d) J. Tong, R. K. Kremer, J. Köhler, A. Simon, C. Lee, E. Kan, M.-H. Whangbo, *Z. Kristallogr.* **2010**, *225*, 498-503.
4. a) D. Dai, M.-H. Whangbo, *J. Chem. Phys.* **2001**, *114*, 2887-2893. b) D. Dai, M.-H. Whangbo, *J. Chem. Phys.* **2003**, *118*, 29-39.

**Table 4.1** Relative energies (in meV) of the ordered spin states AF1 – AF4 of  $\text{Ag}_2\text{ZnZr}_2\text{F}_{14}$  obtained from GGA+U calculations as a function of U (in eV).

<b>U</b>	<b>2</b>	<b>3</b>	<b>4</b>	<b>5</b>	<b>6</b>
<b>AF1</b>	64.53	61.06	54.48	47.16	39.87
<b>AF2</b>	1164.1	997.91	856.74	754.62	656.69
<b>AF3</b>	0	0	0	0	0
<b>AF4</b>	62.74	59.74	53.52	46.43	39.28

**Table 4.2** Values (in meV) of the spin exchanges  $J_1 - J_3$  of  $\text{Ag}_2\text{ZnZr}_2\text{F}_{14}$  obtained from GGA+U calculations as a function of U (in eV).

<b>U</b>	<b>2</b>	<b>3</b>	<b>4</b>	<b>5</b>	<b>6</b>
<b>J<sub>1</sub></b>	-36.4	-31.2	-27.1	-23.6	-20.5
<b>J<sub>2</sub></b>	-1.0	-0.9	-0.8	-0.7	-0.6
<b>J<sub>3</sub></b>	0.03	0.02	0.02	0.01	0.01

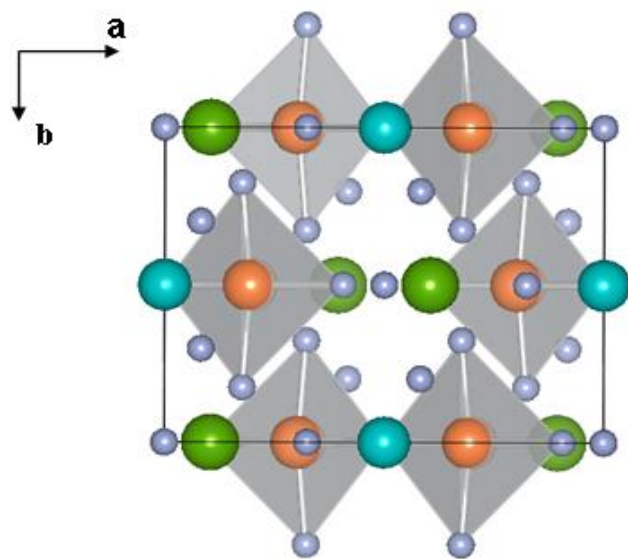


**Fig. 4.1** Perspective view of the crystal structure of  $\text{Ag}_2\text{ZnZr}_2\text{F}_{14}$ . The orange, green, blue and grey represent silver, zirconium, zinc and fluorine atoms, respectively. The  $\text{AgF}_4$  units are highlighted (in grey).

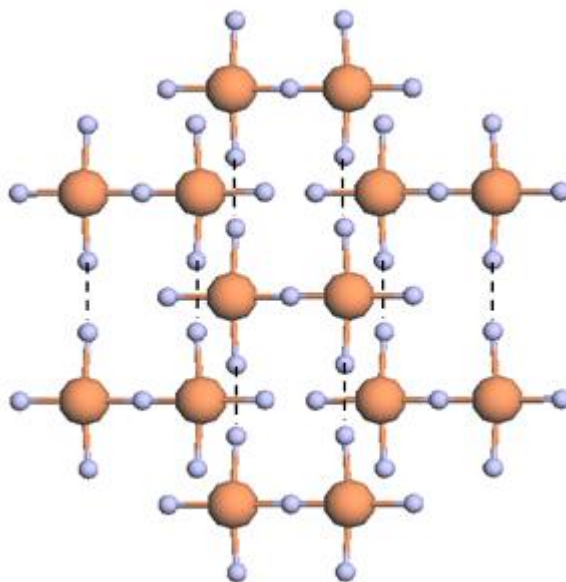


**Fig. 4.2** Two-leg ladders of  $\text{Ag}^{2+}$  ions resulting from  $\text{Ag}_2\text{F}_7$  dimers. The dotted lines running along the b-axis represent the short F...F contacts ( $2.275 \text{ \AA}$ ) between  $\text{Ag}_2\text{F}_7$  dimers.

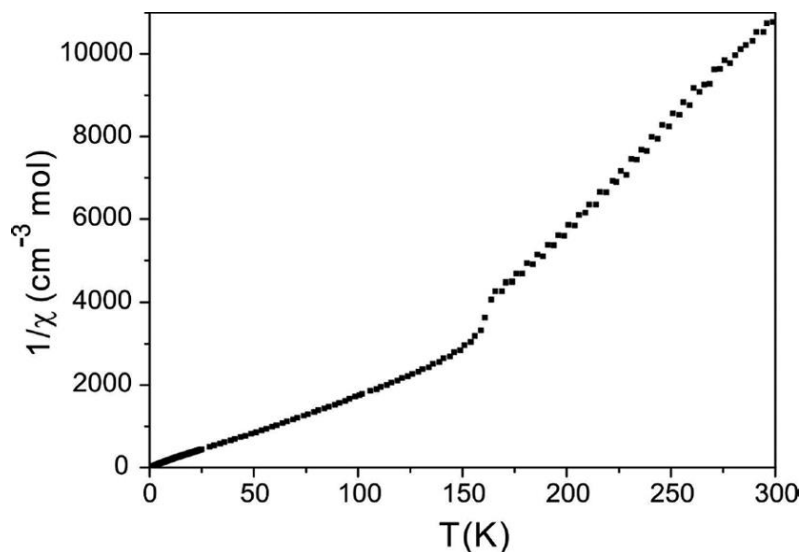


**Fig. 4.3** Temperature dependence of the inverse molar susceptibility of  $\text{Ag}_2\text{ZnZr}_2\text{F}_{14}$  at a magnetic field of 1T. The transition at around 163K is caused by a small amount of  $\text{AgF}_2$  in the sample.

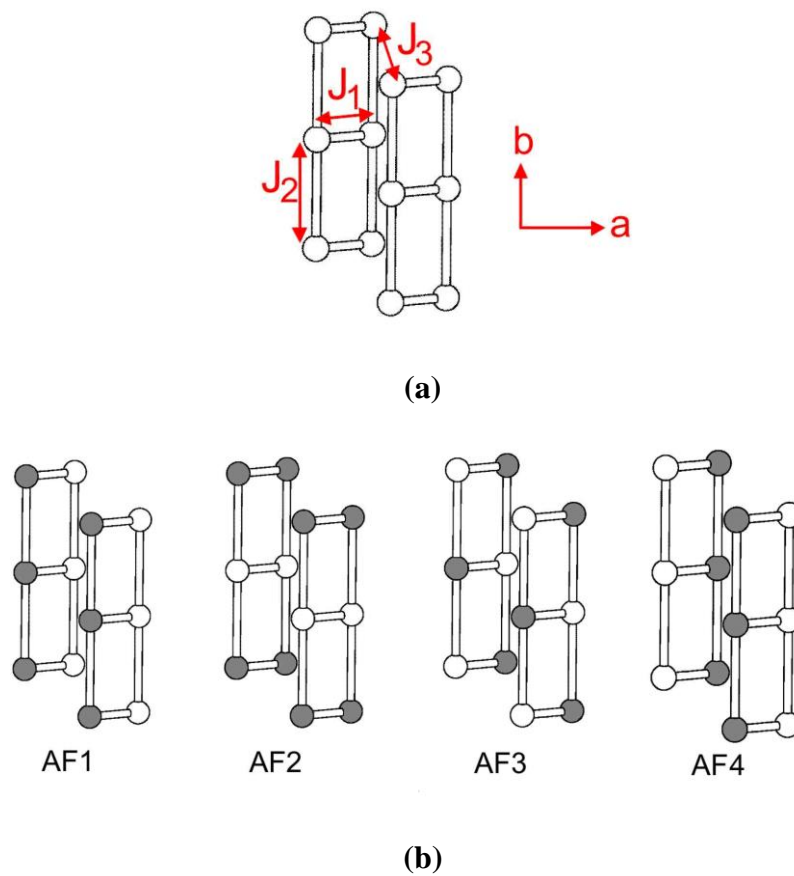


**Fig. 4.4** (a) Intra-ladder spin and inter-ladder spin exchange ( $J_1 - J_3$ )  $\text{Ag}_2\text{ZnZr}_2\text{F}_{14}$ , where the circles represent the  $\text{Ag}^{2+}$  ions. (b) Four ordered spin arrangements used for GGA+U calculations to extract the values of  $J_1 - J_3$ .

## 5. Magnetic structure and spin orientation in LiNaCo[PO<sub>4</sub>]F<sup>1</sup>

LiNaCo[PO<sub>4</sub>]F<sup>1</sup> has two non-equivalent Co atoms, Co1 and Co2, forming Co1F<sub>2</sub>O<sub>4</sub> and Co2F<sub>2</sub>O<sub>4</sub> octahedra Co<sup>2+</sup> (d<sup>7</sup>, S = 3/2) ions. The Co1F<sub>2</sub>O<sub>4</sub> octahedra share their edges to form the CoFO<sub>3</sub> chains running along the *b* axis, and so do the Co2F<sub>2</sub>O<sub>4</sub> octahedra (**Fig. 5.1**), such that each Co1FO<sub>3</sub> chain is surrounded by four Co2FO<sub>3</sub> chains, and vice versa. In direction, the shared O...F edges of the Co1FO<sub>3</sub> chains (close to the *c*-axis) are almost orthogonal to those of the Co2FO<sub>3</sub> chains (close to the *a*-axis). These chains are interlinked by PO<sub>4</sub> tetrahedra forming the 3D framework of LiNaCo[PO<sub>4</sub>]F with the Li<sup>+</sup> and Na<sup>+</sup> ions occupying the cavities of the framework.

The magnetic susceptibility of LiNaCo[PO<sub>4</sub>]F (**Fig. 5.2a**) follows a Curie-Weiss behavior above 50 K with Curie-Weiss temperature  $\theta = -21$  K, suggesting the presence of dominant AFM interactions.<sup>1</sup> The magnetic susceptibility data plus the specific heat measurements (**Fig. 5.2b**) show that LiNaCo[PO<sub>4</sub>]F undergoes a 3D AFM ordering at  $T_N = 10.2(5)$  K. The 3D magnetic structure determined by powder neutron diffraction measurements<sup>1</sup> is shown in **Fig. 5.3**, which reveals that the spins in each CoFO<sub>3</sub> chain along the *b*-direction are ferromagnetically coupled, and these FM chains in the *ab*-planes are antiferromagnetically coupled. However, the FM chains in the *bc*-plane have a non-collinear arrangement ( $\sim 136^\circ$  between adjacent spin vectors (**Fig. 5.3**), which implies the presence of spin frustration along the *c*-direction. This is apparently surprising because the index of spin frustration  $f = |\theta|/T_N \approx 2$  is rather small.<sup>2</sup>

To gain insight into the observed magnetic properties of LiNaCo[PO<sub>4</sub>]F, we evaluate the six spin exchange interactions,  $J_1, J_1', J_2, J_2', J_3, J_3'$ , shown in **Fig. 5.4** by performing

energy-mapping analysis based on DFT electronic structure calculations.<sup>3</sup> We consider the seven ordered spin states FM – AF6 shown in **Fig. 5.4** and determine their relative energies per eight FUs by performing GGA+U calculations with  $U = 1$  and  $2$  eV (**Table 5.1**). Here the ground state (GS) refers to the observed magnetic structure, and our calculations show that the GS is indeed found to be the lowest energy state of the nine ordered spin states. The GS is not calculated to be the lowest-energy state for  $U = 3$  eV or greater. In terms of the spin Hamiltonian,  $\hat{H} = -\sum_{i<j} J_{ij} \hat{S}_i \cdot \hat{S}_j$ , where  $J_{ij}$  ( $= J_1 - J_4$ ) is the spin exchange constant for the interaction between the sites  $i$  and  $j$ . Then by using the expressions of the spin exchange interactions for spin dimers with  $N$  unpaired spins per site ( $N=3$  in the present case),<sup>4</sup> the total spin exchange energies, per eight FUs, of the seven ordered spin states are written as

$$\begin{aligned}
\text{FM} &= -(4J_1 + 4J_{1'} + 8J_2 + 8J_{2'} + 16J_3 + 16J_{3'} + 8J_4 + 8J_{4'}) (N^2/4) \\
\text{AF1} &= -(-4J_1 + 4J_{1'} + 8J_4 + 8J_{4'}) (N^2/4) \\
\text{AF2} &= -(-4J_1 - 4J_{1'} + 8J_4 + 8J_{4'}) (N^2/4) \\
\text{AF3} &= -(-4J_1 - 4J_{1'} - 8J_2 + 8J_{2'} + 16J_3 - 16J_{3'} - 8J_4 - 8J_{4'}) (N^2/4) \\
\text{AF4} &= -(-4J_1 - 4J_{1'} + 8J_2 + 8J_{2'} - 16J_3 - 16J_{3'} + 8J_4 + 8J_{4'}) (N^2/4) \\
\text{AF5} &= -(-4J_1 - 4J_{1'} + 8J_2 - 8J_{2'} - 16J_3 + 16J_{3'} - 8J_4 - 8J_{4'}) (N^2/4) \\
\text{AF6} &= -(8J_{2'}) (N^2/4) \\
\text{AF7} &= -(4J_1 + 4J_{1'} + 8J_4 - 8J_{4'}) (N^2/4) \\
\text{GS} &= -(4J_1 + 4J_{1'} - 8J_2 - 8J_{2'} - 16J_3 - 16J_{3'} + 8J_4 + 8J_{4'}) (N^2/4)
\end{aligned}$$

Thus, by mapping the relative energies of the seven ordered spin states determined from GGA+U calculations onto the corresponding relative energies determined from the above expressions, we obtain the values of  $J_1 - J_3$  listed in **Table 5.2**.

To check the proper range of  $U$  values, we calculate the Curie-Weiss temperature  $\theta$  in the mean-field approximation by using the calculated spin exchange parameters.<sup>5</sup> Since there are two non-equivalent Co sites in the 50:50 ratio,  $\theta$  can be written as

$$\begin{aligned}\theta &= \frac{S(S+1)}{3k_B} \sum_i z_i J_i \\ &= \frac{S(S+1)}{3k_B} [0.5(2J_1 + 2J_2 + 2J_{2'} + 4J_3 + 4J_{3'}) + 0.5(2J_{1'} + 2J_2 + 2J_{2'} + 4J_3 + 4J_{3'})]\end{aligned}$$

The  $\theta$  determined by using the calculated  $J$  values are also listed in **Table 5.2**. The calculated  $\theta$  is greater than the experimental value (-21 K) by a factor of  $\sim 2$  for all the GGA+ $U$  calculations with  $U = 1$  and 2 eV. Thus, in our analysis of the experimental magnetic properties in terms of our calculated spin exchanges, it is necessary to consider the trends that are independent of the  $U$  values used to calculate them.

We now discuss the observed magnetic structure of LiNaCo[PO<sub>4</sub>]F on the basis of the calculated  $J$  values listed in Table 2. The dominant spin exchanges are  $J_1$ ,  $J_{3'}$ ,  $J_3$ ,  $J_4$ , and  $J_4'$ . Due to the strong FM exchange  $J_1$ , the spins of each Co<sub>2</sub>FO<sub>3</sub> chain become ferromagnetically ordered. Because of the strong AFM interchain exchange  $J_3$  and the weak intrachain exchange  $J_1$ , the spins of each Co<sub>1</sub>FO<sub>3</sub> chain also become ferromagnetically ordered. Along the  $a$ -direction, each FM Co<sub>2</sub>FO<sub>3</sub> chain becomes antiferromagnetically coupled with its adjacent FM Co<sub>1</sub>FO<sub>3</sub> chains due to the strong AFM exchange  $J_3$ . Now let us consider the noncollinear spin arrangement between the FM CoFO<sub>3</sub> chains along the  $c$ -direction. If only the interchain AFM exchange  $J_{3'}$  is considered, an AFM arrangement between them would be predicted. However, the interchain FM exchange  $J_2$  is comparable in

magnitude with the intrachain FM exchange  $J_1$ . Thus, the  $(J_1, J_2, J_3)$  triangles lead to spin conflict between adjacent FM  $\text{CoFO}_3$  chains along the  $c$ -direction.<sup>2</sup> Consequently, the FM  $\text{CoFO}_3$  chains adopt the noncollinear spin arrangement along the  $c$ -direction. In the  $(J_2, J_2', J_4)$  and  $(J_2, J_2, J_4')$  triangles, the extent of spin conflict is negligible because  $J_2$  is weak.

## References

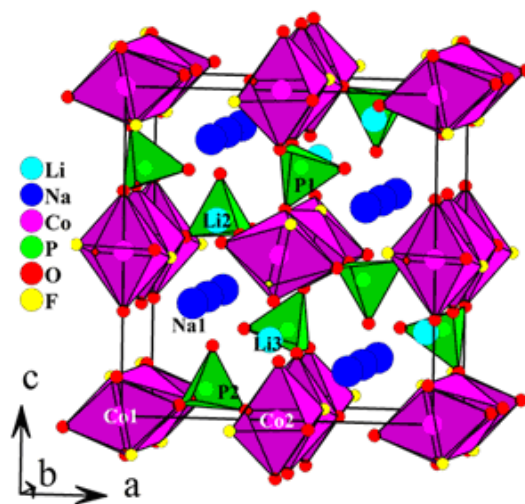
1. Yahia, H.B.; Shikano, M.; Kobayashi, H.; Koike, S.; Tatsumi, K.; Kawaji, H.; Avdeev, M.; Liu, J.; Whangbo, M.-H. *Inorg. Chem.* **2012**, 51, 8729-8738.
2. (a) Greedan, J. E. *J. Mater. Chem.* **2001**, 11, 37 and the references cited therein. (b) Dai, D.; Whangbo, M.-H. *J. Chem. Phys.* **2004**, 121, 672.
3. Whangbo, M.-H.; Koo, H.-J.; Dai, D. *J. Solid State Chem.* **2003**, 176, 417.
4. (a) Dai, D.; Whangbo, M.-H. *J. Chem. Phys.* **2001**, 114, 2887. (b) Dai, D.; Whangbo, M.-H. *J. Chem. Phys.* **2003**, 118, 29.
5. Smart, J. S.; *Effective Field Theory of Magnetism*: Saunders, Philadelphia, **1966**.

**Table 5.1** Relative energies (in meV) of the ordered spin states FM – AF6 of LiNaCo[PO<sub>4</sub>]F obtained from GGA+U calculations as a function of U (in eV).

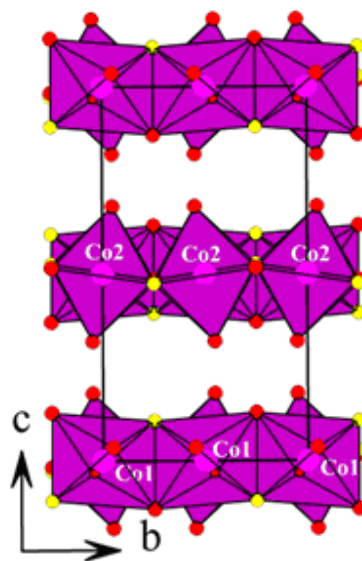
<b>U/eV</b>	<b>FM</b>	<b>AF1</b>	<b>AF2</b>	<b>AF3</b>	<b>AF4</b>	<b>AF5</b>	<b>AF6</b>	<b>AF7</b>	<b>GS</b>
<b>1</b>	76.32	44.12	51.55	57.89	9.88	49.06	47.84	53.84	0
<b>2</b>	57.70	28.59	34.04	36.29	2.12	31.78	31.31	45.56	0

**Table 5.2** Values (in K) of the spin exchanges  $J_1 - J_4'$  of  $\text{LiNaCo[PO}_4\text{]F}$  along with the calculated Curie-Weiss temperature  $\theta$  (in K) obtained from GGA+U calculations as a function of U (in eV).

<b>U (eV)</b>	<b>J1</b>	<b>J1'</b>	<b>J2</b>	<b>J2'</b>	<b>J3</b>	<b>J3'</b>	<b>J4'</b>	<b>J4'</b>	<b><math>\theta</math>/K</b>
<b>1</b>	3.84	8.63	-1.79	4.84	-8.10	-5.73	-6.84	5.05	-50
<b>2</b>	-0.17	3.35	0.08	0.79	-4.68	-5.06	-4.34	4.42	-42

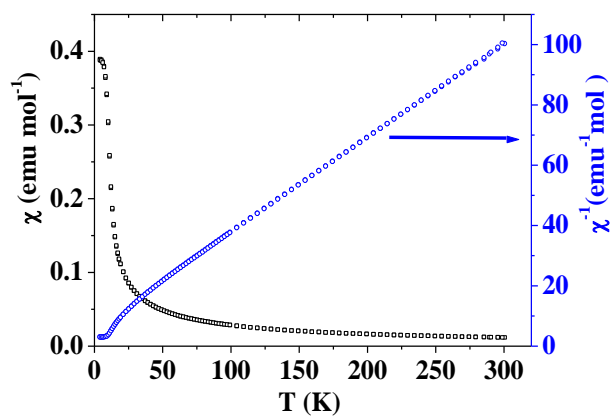


(a)

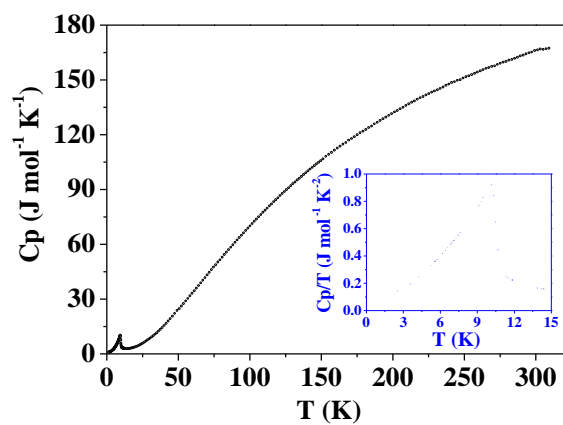


(b)

**Fig. 5.1** Perspective views of the LiNaCo[PO<sub>4</sub>]F structure (a) with and (b) without the phosphorus and alkali metal atoms.



(a)



(b)

**Fig. 5.2** (a) Magnetic susceptibility  $\chi$  vs. Temperature and the corresponding  $\chi^{-1}$  vs. T plots of  $\text{LiNaCo}[\text{PO}_4]\text{F}$  measured with the applied field  $H = 10$  kOe. (b) Heat capacities  $C_p(T)$  of  $\text{LiNaCo}[\text{PO}_4]\text{F}$ . The inset displays  $C_p/T$  in the region of the phase transition at  $10.2(5)$  K.

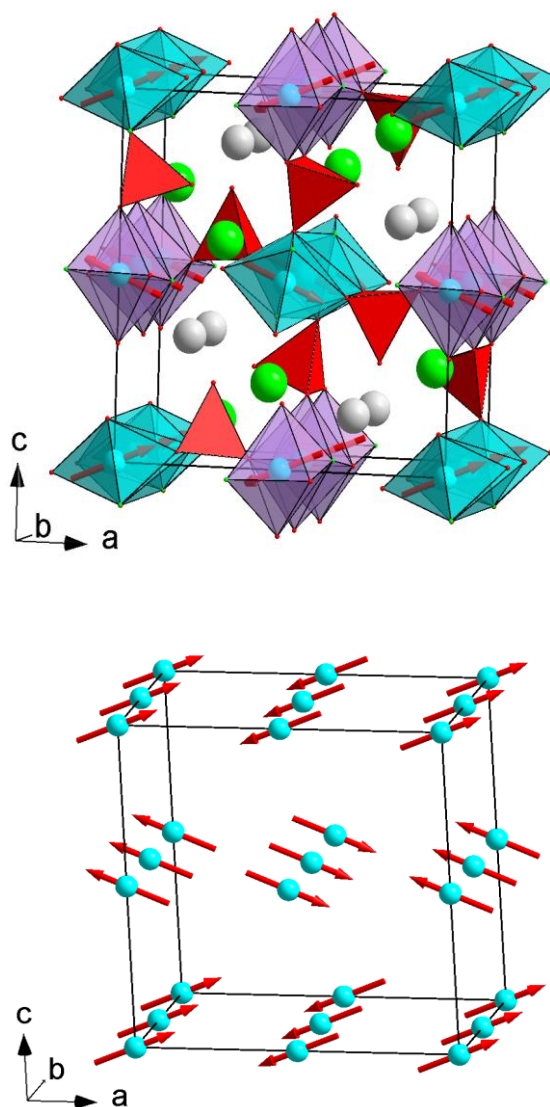


**Fig. 5.3** The magnetic structure of LiNaCo[PO<sub>4</sub>]F at 3K. The components of the moment along x, y, and z axes are 2.13(2), 0, and 0.87(2)  $\mu_B$ , respectively. The total moment is 2.30(2)  $\mu_B$ , and the angle between the moment direction and ab-plane is 22.2°.

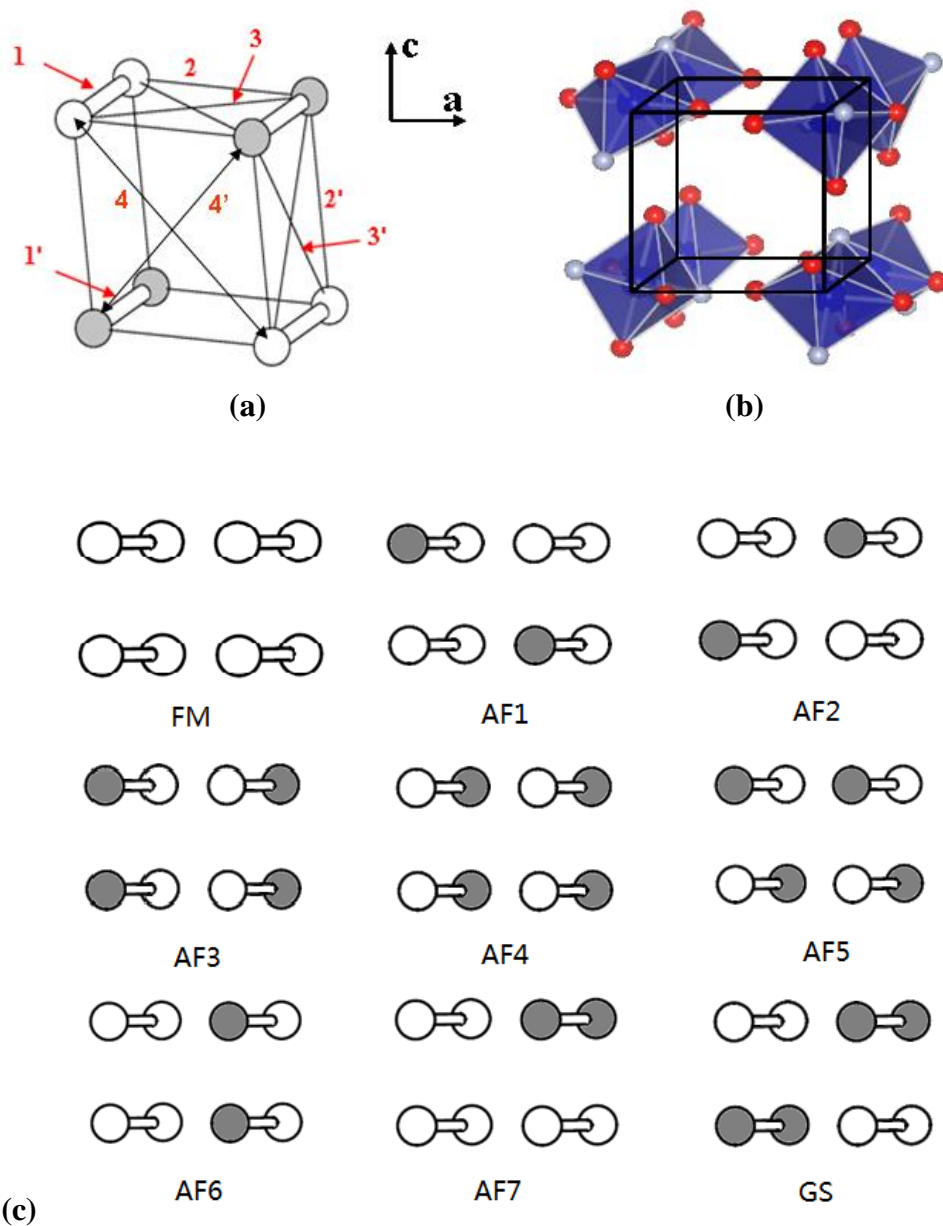


**Fig. 5.4** (a, b) Definitions of the spin exchange paths  $J_1$ ,  $J_2$ ,  $J_3$ ,  $J_{1'}$ ,  $J_{2'}$ , and  $J_{3'}$ . The Co1 and Co2 atoms are indicated as empty and filled circles, respectively. The numbers 1, 2, 3, 1', 2' and 3' refer to the spin exchanges  $J_1$ ,  $J_2$ ,  $J_3$ ,  $J_{1'}$ ,  $J_{2'}$ , and  $J_{3'}$ , respectively. (c) Ordered spin

arrangements of the Co1 and Co2 spin sites used to extract the values of  $J_1$ ,  $J_2$ ,  $J_3$ ,  $J_{1'}$ ,  $J_{2'}$ , and  $J_{3'}$  by GGA+U calculations. The positions of the Co1FO<sub>3</sub> and Co2FO<sub>3</sub> chains are identical with those of (a, b), and the up-spin and down-spin Co<sup>2+</sup> sites are indicated by empty and filled circles, respectively.

## 6. Spin frustration and field-induced magnetic order in $\text{Bi}_3\text{Mn}_4\text{O}_{12}(\text{NO}_3)$

### 6.1 Experimental observations

The neutron diffraction measurements of  $\text{Bi}_3\text{Mn}_4\text{O}_{12}(\text{NO}_3)$  (BMNO) showed that it has a trigonal structure ( $P3$ ),<sup>1</sup> which consists of 2D honeycomb  $\text{Mn}_2\text{O}_6$  layers made up of edge-sharing  $\text{MnO}_6$  octahedra containing  $\text{Mn}^{4+}$  ( $d^3$ ,  $S = 3/2$ ) ions shown in **Fig. 6.1a**. As depicted in **Fig. 6.1b**, a unit cell has two slightly different  $\text{Mn}_2\text{O}_6$  layers, one made up of  $\text{Mn}(1)\text{O}_6$  and  $\text{Mn}(2)\text{O}_6$  octahedra forming  $\text{Mn}(1)\text{Mn}(2)\text{O}_6$  layers, and the other made up of  $\text{Mn}(3)\text{O}_6$  and  $\text{Mn}(4)\text{O}_6$  octahedra forming  $\text{Mn}(3)\text{Mn}(4)\text{O}_6$  layers. The  $\text{Bi}_3\text{Mn}_4\text{O}_{12}$  slab of BMNO is obtained by combining  $\text{Mn}(1)\text{Mn}(2)\text{O}_6$  and  $\text{Mn}(3)\text{Mn}(4)\text{O}_6$  layers with three different Bi atoms; the Bi(1) atoms occupy the hexagonal holes between the two  $\text{Mn}_2\text{O}_6$  layers forming  $\text{BiO}_6$  octahedra (**Figs. 6.1b, 6.1c and 6.1d**), and the Bi(2) and Bi(3) atoms cap the hexagonal holes on the lower and upper  $\text{Mn}_2\text{O}_6$  layers of the  $\text{Bi}_3\text{Mn}_4\text{O}_{12}$  slab forming  $\text{BiO}_3$  trigonal pyramids. The 3D structure of BMNO is obtained by stacking the  $\text{Bi}_3\text{Mn}_4\text{O}_{12}$  slabs along the  $c$ -direction with  $\text{NO}_3^-$  ions intercalated between the slabs as depicted in **Fig. 6.1e**.

The magnetic susceptibility measurements show that the Curie-Weiss temperature  $\theta$  of BMNO is -257 K, revealing the presence of dominant AFM interactions.<sup>1</sup> However, the neutron diffraction experiments show no long-range magnetic ordering down to 0.4 K.<sup>1,2</sup> ESR experiments also found no magnetic order down to 1.9 K.<sup>3</sup> A honeycomb lattice with only AFM nearest-neighbor (NN) spin exchange  $J_1$  is not spin-frustrated. However, if the next NN (NNN) spin exchange  $J_2$  is also AFM and if the  $J_2/J_1$  ratio is greater than the critical value of 0.15, then the  $(J_1, J_1, J_2)$  triangles of the honeycomb lattice (made up of spin-3/2

ions) are spin-frustrated so that the magnetic structure is disordered.<sup>4-7</sup> The honeycomb spin lattice of BMNO has received much attention because it was considered as the realization of a spin-frustrated honeycomb lattice. However, Matsuda *et al.*<sup>2</sup> found that BMNO undergoes a long-range AFM order, with the spin moments lying in the *ab*-plane, when it is subject to magnetic fields higher than 6 T. So far, the origin of this field-induced magnetic ordering is not well understood.

The magnetic properties of BMNO are discussed by considering various intra- and inter-layer spin exchange interactions (**Fig. 6.2**). From their neutron scattering experiments, Matsuda *et al.*<sup>2</sup> deduced that the inter-layer exchange  $J_c \approx J_1/2$  under the assumption that  $J_2/J_1 \approx 0.15$ . This indicates that the inter-layer interaction is substantial. There are several inter-layer spin exchange paths as can be seen from **Fig. 6.2b**. The work of Matsuda *et al.*<sup>2</sup> does not provide any information whether or not the inter-layer spin exchanges are spin-frustrated, because they considered only one inter-layer spin exchange  $J_c$ . A recent density functional study by Kandpal and van den Brink,<sup>8</sup> in which the intra-layer exchanges  $J_1 - J_3$  as well as the direct inter-layer spin exchange  $J_c$  and the effective inter-layer spin exchange  $J_c + 3J_c$  were evaluated, showed that the  $J_2/J_1$  ratio is smaller than the critical value of 0.15, that the exchange  $J_3$  is stronger than  $J_2$  providing additional intra-layer spin frustration due to the spin frustration of the  $(J_1, J_2, J_3)$  triangles, and that the inter-layer exchange is as strong as, or stronger than,  $J_1$ . In this density functional study as well, it is unclear whether or not the inter-layer spin exchanges are spin-frustrated. Very recently a rather different picture of the intra-layer spin frustration emerged from the X-ray absorption spectroscopy study by Wadati *et al.*,<sup>9</sup> who suggested that  $J_1$  and  $J_4$  are AFM but  $J_2$  and  $J_3$  are FM, so the intra-layer spin

frustration is caused by the ( $J_1, J_2, J_3$ ) triangles (**Fig. 6.2**). In view of the conflicting pictures concerning the intra- and inter-layer spin frustration, we carry out density functional calculations to determine the intra- and inter-layer spin exchanges ( $J_1 - J_3$  and  $J_c - J_c''$ , respectively) of BMNO.

## 6.2. Structure optimization and spin exchange interactions

With the experimental crystal structure of BMNO,<sup>1</sup> our GGA calculations show that it has no band gap at the Fermi level, as can be seen from the DOS plots of **Fig. 6.3a**. Since this suggests that BMNO is a metal rather than a magnetic insulator, in disagreement with the experimental observations, we optimized the crystal structure with GGA to see if the optimized structure has a band gap. The DOS plots calculated for the optimized structure (**Fig. 6.3b**) has an insulating gap at the Fermi level. It is of interest to examine why the optimized structure has a band gap while the experimental structure does not. We note that the Bi(1), Bi(2) and Bi(3) atoms form straight  $[\text{Bi}(2)\dots\text{Bi}(1)\dots\text{Bi}(3)\dots\text{Bi}(2)\dots]_\infty$  chains along the c-direction. In the experimental structure,  $\text{Bi}(2)\dots\text{Bi}(1) = 4.633 \text{ \AA}$ ,  $\text{Bi}(1)\dots\text{Bi}(3) = 4.699 \text{ \AA}$  and  $\text{Bi}(3)\dots\text{Bi}(2) = 3.830 \text{ \AA}$ . In the optimized crystal structure,  $\text{Bi}(2)\dots\text{Bi}(1) = 4.723 \text{ \AA}$ ,  $\text{Bi}(1)\dots\text{Bi}(3) = 4.723 \text{ \AA}$  and  $\text{Bi}(3)\dots\text{Bi}(2) = 3.716 \text{ \AA}$ . In essence, the  $\text{Bi}_3\text{Mn}_4\text{O}_{12}$  slab becomes more symmetrical and thicker and the inter-slab Bi...Bi contact becomes smaller in the optimized structure, so that the extent of this long-long-short alternation of the Bi...Bi contacts is stronger in the optimized structure. In our subsequent calculations for BMNO, we employ the optimized structure.

For the spin exchange interactions of BMNO, we consider the three intra-layer exchanges  $J_1 - J_3$  and the four inter-layer exchanges  $J_c - J_{c''}$  defined in **Fig. 6.2**. To evaluate these interactions, we determine the relative energies of the eight ordered spin states FM and AF1 – AF7 defined using a (2a, b, 2c) supercell (**Fig. 6.4**). The relative energies of these states calculated by performing GGA+U calculations with  $U = 0, 1, 2, 3$  and 4 eV are summarized in **Table 6.1**. To extract the values of seven  $J$ 's, we express the total spin exchange interaction energies of the eight ordered spin states in terms of the spin Hamiltonian,  $H = -\sum_{i<j} J_{ij} \hat{S}_i \cdot \hat{S}_j$  where  $J_{ij} = J_1 - J_3$  and  $J_c - J_{c''}$ . By applying the energy expression obtained for spin dimers consisting of two spin sites with  $N$  unpaired spins (i.e.,  $N = 3$  for  $Mn^{4+}$ ), the total spin exchange energies per supercell, i.e., per four formula units (FUs), of the eight ordered spin states are written as

$$\begin{aligned}
E_{\text{FM}} &= -(24J_1 + 48J_2 + 24J_3 + 8J_c + 48J_{c'} + 48J_{c''} + 48J_{c''})(N^2/4) \\
E_{\text{AF1}} &= -(-24J_1 + 48J_2 - 24J_3 + 8J_c - 48J_{c'} + 48J_{c''} - 48J_{c''})(N^2/4) \\
E_{\text{AF2}} &= -(-8J_1 - 16J_2 + 24J_3 + 8J_c - 16J_{c'} - 16J_{c''} + 48J_{c''})(N^2/4) \\
E_{\text{AF3}} &= -(16J_2 + 8J_c + 16J_{c''})(N^2/4) \\
E_{\text{AF4}} &= -(-24J_1 + 48J_2 - 24J_3 - 8J_c + 48J_{c'} - 48J_{c''} + 48J_{c''})(N^2/4) \\
E_{\text{AF5}} &= -(-8J_1 + 16J_2 + 24J_3 - 8J_c + 16J_{c'} + 16J_{c''} - 48J_{c''})(N^2/4) \\
E_{\text{AF6}} &= -(-8J_1 + 16J_2 - 24J_3)(N^2/4) \\
E_{\text{AF7}} &= -(16J_2 + 8J_c + 16J_{c''})(N^2/4)
\end{aligned}$$

Then, by mapping the relative energies of the four ordered spin states determined from GGA+U calculations onto the corresponding relative energies determined from the above expressions, we obtain the values of the spin exchanges listed in **Table 6.2**. The Curie-Weiss temperatures calculated on the basis of the mean field theory by using the calculated spin

exchanges are also listed in **Table 6.2**, which shows that the set of the spin exchanges obtained from the GGA+U calculations with  $U = 0$  and 1 eV reproduce the experimental Curie-Weiss temperature reasonably (i.e., -388 and 200 K, respectively, versus the experimental value of -257 K). Thus, in our further analysis of the magnetic properties of BMNO, we used this set of the spin exchanges obtained from our GGA calculations (i.e., GGA+U calculations with  $U = 0$ ).

We note from **Table 6.2** that the  $J_2/J_1$  ratio is smaller than the critical value of 0.15, and  $J_3$  is stronger than  $J_2$  providing extra spin frustration within each honeycomb layer. These two observations are in agreement with the density functional study of Kandpal and van den Brink,<sup>8</sup> and do not support the speculation by Wadati *et al.*<sup>9</sup> Our calculations show that  $J_c/J_1 \approx 0.5$  in agreement with the estimate of Matsuda *et al.*<sup>2</sup>, and do not support the conclusion by Kandpal and van den Brink<sup>8</sup> that  $J_c/J_1 \geq 1$ . **Table 6.2** shows that all inter-layer spin exchanges in the  $(J_c, J_1, J_{c'})$ ,  $(J_c, J_2, J_{c''})$ , and  $(J_c, J_3, J_{c'''})$  triangles are spin-frustrated. It is clear that the inter-layer spin frustration is as important as the intra-layer spin frustration in BMNO.

## References

1. Smirnova, O.; Azuma, M.; Kumada N.; Kusano, Y.; Matsuda M.; Shimakawa, Y.; Takei, T.; Yonesaki, Y.; Kinomura, N. *J. Am. Chem. Soc.* **2009**, *131*, 8313-3615.
2. Matsuda, M.; Azuma, M.; Tokunaga, M.; Shimakawa, Y.; Kumada, N. *Phys. Rev. Lett.* **2010**, *105*, 187201.
3. Okubo, S.; Elmasry, F.; Zhang, W.; Fujisawa, M.; Sakurai, T.; Ohta, H.; Azuma, M.; Sumirnova, O.; Kumada, N. *J. Phys.: Conf. Ser.* **2010**, *200*, 022042.
4. Katsura, S.; Ide, T.; Morita, T. *J. Stat. Phys.* **1986**, *42*, 381.
5. Takano, K. *Phys. Rev. B* **2006**, *74*, 140402.
6. Okumura, S.; Kawamura, H.; Okubo, T. *J. Phys. Soc. Jpn.* **2010**, *79*, 114705.
7. Ganesh, R.; Sheng, D.N.; Kim, Y.; Paramakanti, A. *Phys. Rev. B* **2011**, *83*, 144414.
8. Kandpal, H.C.; Brink, J.v.d. *Phys. Rev. B* **2011**, *83*, 140412.
9. Wadati, H.; Kato, K.; Wakisaka, Y.; Sudayama, T.; Hawthorn, D.G.; Regier, T.Z.; Onishi, N.; Azuma, M.; Shimakawa, Y.; Mizokawa, T.; Tanaka, A.; Sawatzky, G.A. *arXiv:1101.2847v1* **2011**.

**Table 6.1** Relative energies of eight spin ordered states (in meV/8FUs) with GGA+U calculations with  $U = 0 - 4$  eV.

<b>U (eV)</b>	<b>FM</b>	<b>AF1</b>	<b>AF2</b>	<b>AF3</b>	<b>AF4</b>	<b>AF5</b>	<b>AF6</b>	<b>AF7</b>
<b>0</b>	659.7	0.3	220.5	302.2	0	147.7	207.1	283.1
<b>1</b>	388.3	0	138.5	181.7	0.1	82.7	121.6	164.0
<b>2</b>	188.2	0	78.5	92.5	0.03	34.0	57.7	75.3
<b>3</b>	33.8	8.0	37.3	27.5	7.7	0	12.4	10.1
<b>4</b>	0	117.8	102.8	71.9	117.1	70.0	73.2	53.6

**Table 6.2** Values (in meV) of the spin exchanges  $J_1 - J_{c''''}$  of  $\text{Bi}_3\text{Mn}_4\text{O}_{12}(\text{NO}_3)$  obtained from GGA calculations.

<b>U (eV)</b>	<b><math>J_1</math></b>	<b><math>J_2</math></b>	<b><math>J_3</math></b>	<b><math>J_c</math></b>	<b><math>J_{c'}</math></b>	<b><math>J_{c''}</math></b>	<b><math>J_{c''''}</math></b>	<b><math>\theta/\text{K}</math></b>
<b>0</b>	-4.39	-0.18	-0.48	-2.48	-0.94	-0.21	-0.30	-388
<b>1</b>	-2.44	-0.08	-0.32	-1.95	-0.68	-0.09	-0.16	-200
<b>2</b>	-0.99	-0.02	-0.21	-1.59	-0.50	-0.01	-0.05	-101
<b>3</b>	0.25	0.07	-0.07	-1.39	-0.44	0.02	0.02	-23
<b>4</b>	1.32	0.06	-0.07	-1.23	-0.25	0.13	0.10	45

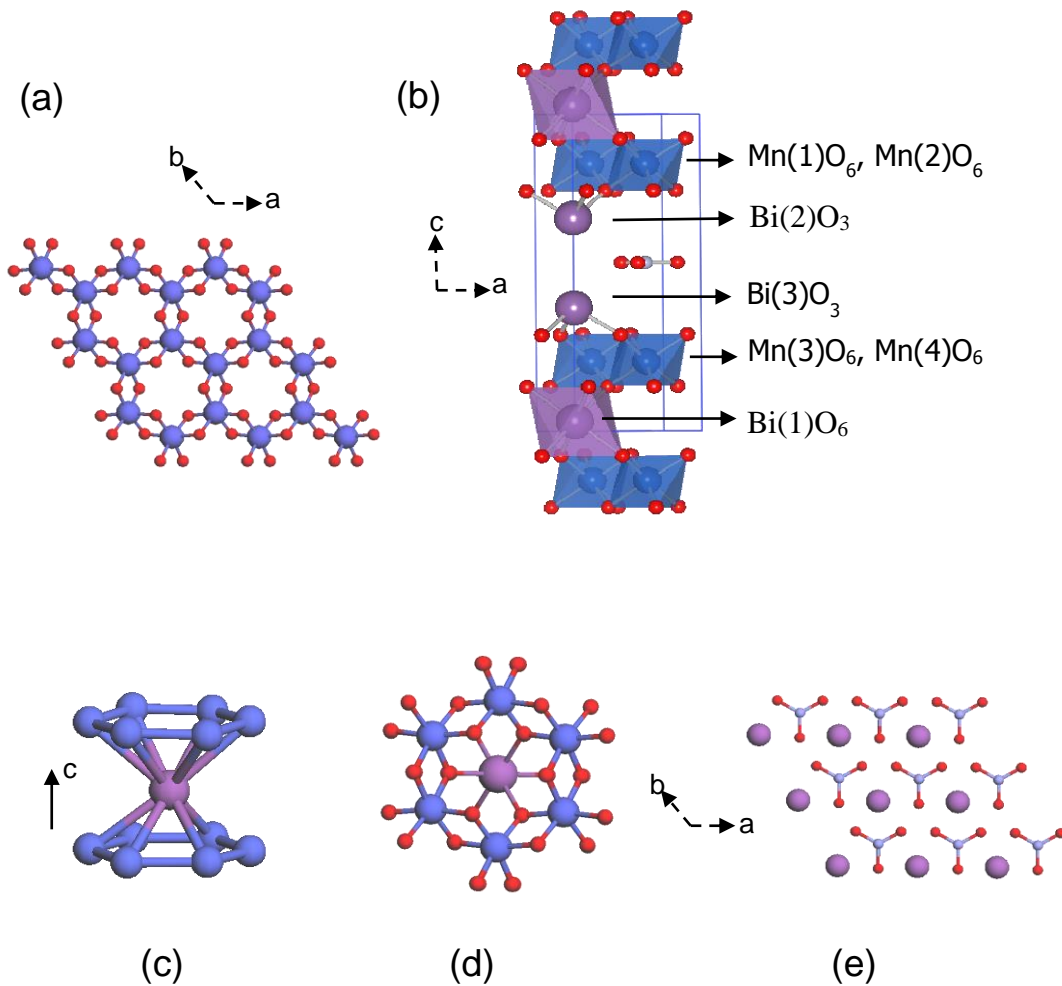


**Fig. 6.1** unit cell view of the  $\text{Bi}_3\text{Mn}_4\text{O}_{12}(\text{NO}_3)$  (a) along  $c$ -axis. (b) along  $b$ -axis with polyhedron shown. (c) Projection view of extended cell. (d) One  $\text{MnO}_6$  layer in  $ab$ -plane. (e) Two layers of  $\text{MnO}_6$  hexagon with  $\text{BiO}_6$  octahedron in between in  $ab$ -plane. (f) Side view of  $\text{Bi-Mn}_{12}$  unit.

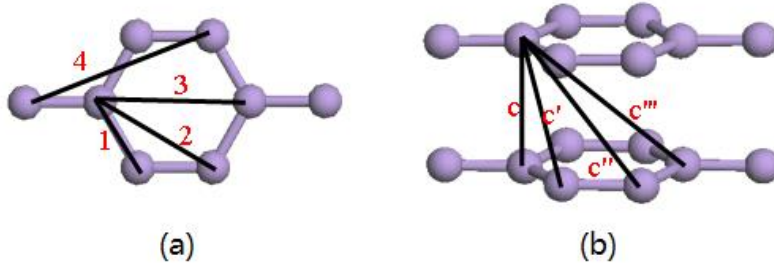


**Fig. 6.2** (a) Intra-layer spin exchange paths  $J_1 - J_4$ . (b) Inter-layer spin exchange paths  $J_c - J_{c''}$ . The number 1 - 4 refer to  $J_1 - J_4$ , respectively, and the symbols  $c - c'''$  to  $J_c - J_{c''}$ , respectively.

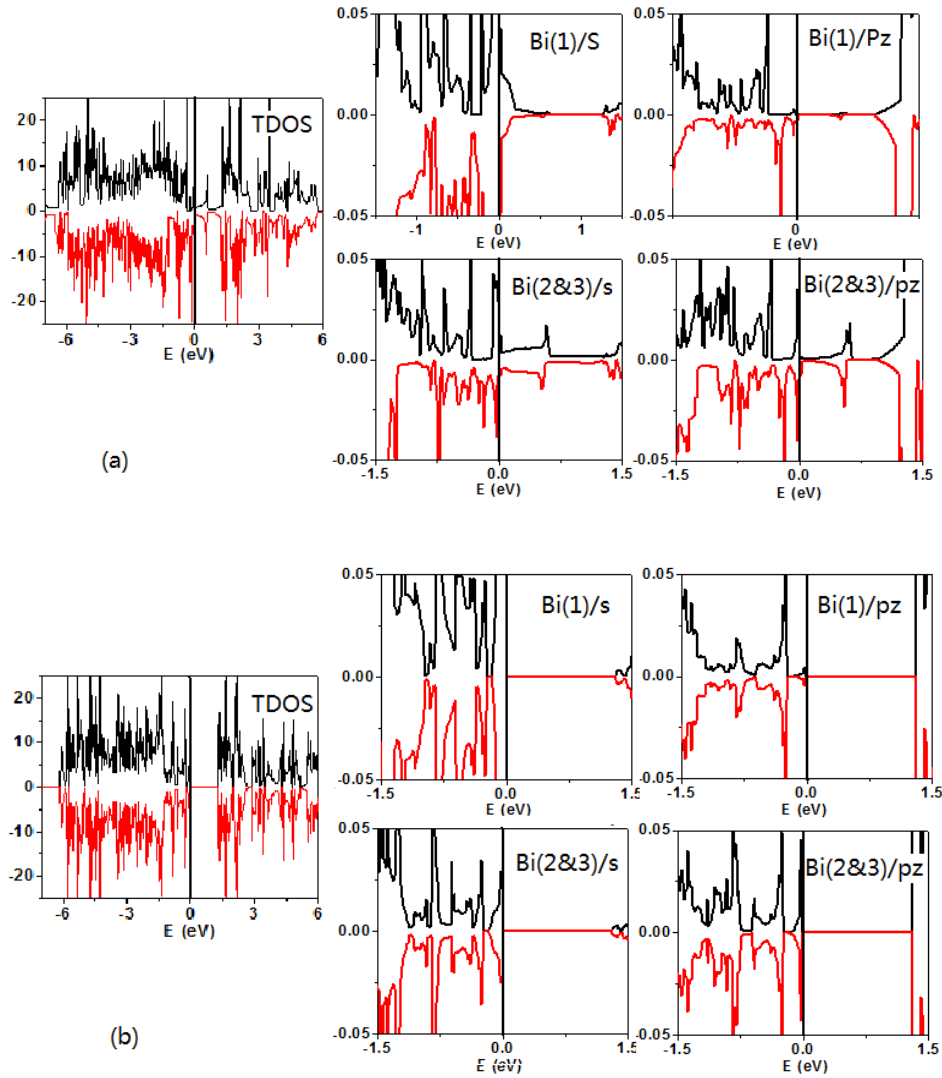


**Fig. 6.3** Total and projected density of state (DOS) plots of (a) experimental and (b) optimized structure.

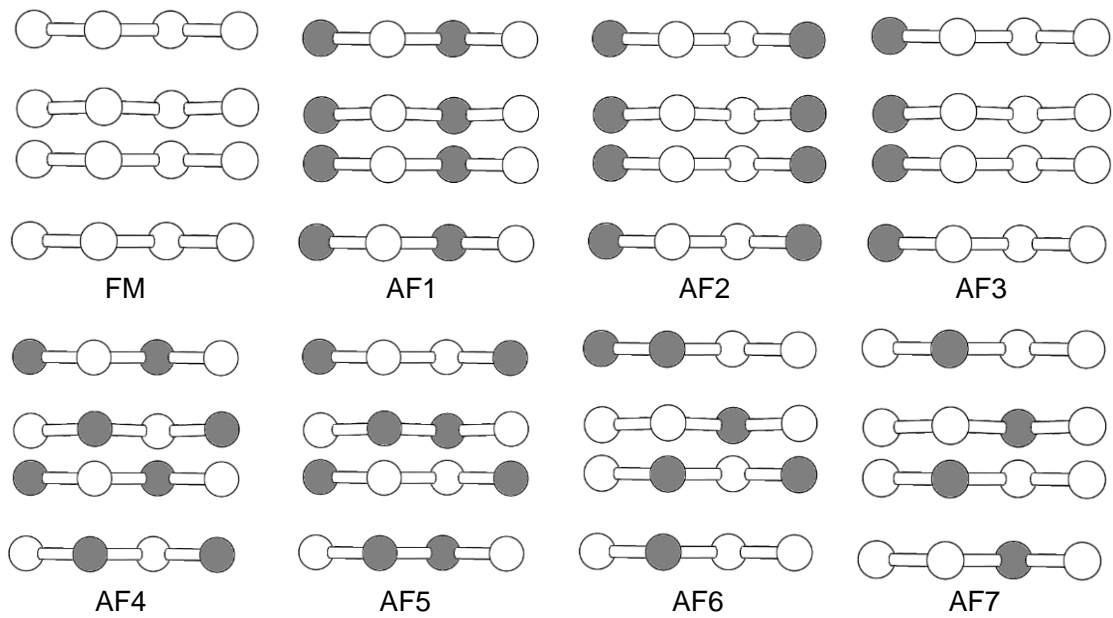


**Fig. 6.4** Eight spin ordered states from FM – AF7 for (2a, b, 2c) supercell.

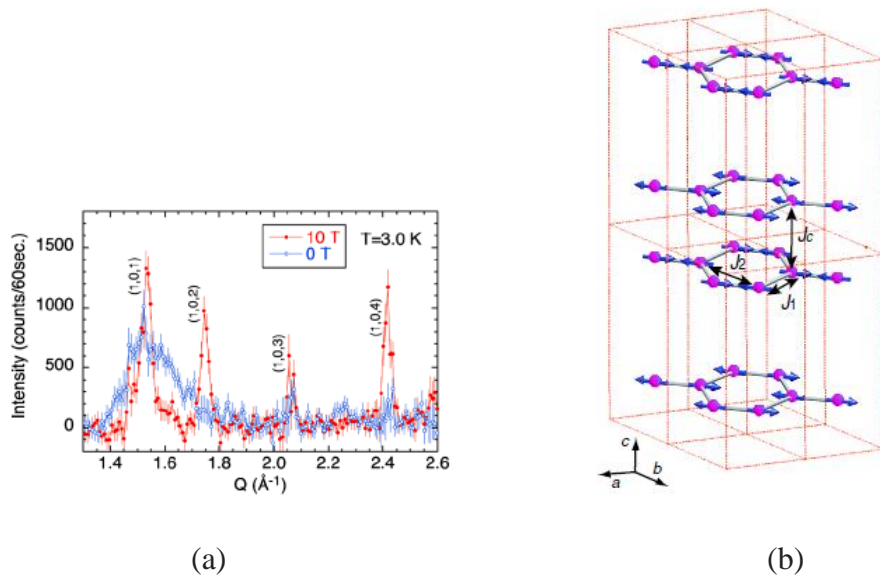


**Fig. 6.5** (a) Neutron powder diffraction patterns in  $\text{Bi}_3\text{Mn}_4\text{O}_{12}(\text{NO}_3)$   $E = 1.7$  meV at  $H = 0$  and 10 T and at  $T = 3$  K. At 10 T the broad magnetic peak is reduced and sharp magnetic peaks appear. (b) Magnetic structure in the magnetic field-induced phase. The  $\text{Mn}^{4+}$  ions in a  $2 \times 2 \times 2$  supercell are shown. The magnetic moments lie in the  $ab$  plane, although the direction of the magnetic moments in the plane cannot be determined uniquely. Magnetic interactions  $J_1$ ,  $J_2$ , and  $J_c$  are also shown.

## 7. Characterization of the spin-1/2 linear-chain ferromagnet $\text{CuAs}_2\text{O}_4$ <sup>1</sup>

Low dimensional magnetic  $\text{Cu}^{2+}$  systems containing  $\text{CuX}_2$  ribbon chains have attracted a great deal of attention because of their unusual intrachain nearest- and next-nearest-neighbor spin exchange relations. In such compounds it is frequently found that the spin exchange interactions between the  $\text{Cu}^{2+}$  ( $S = 1/2$ ) ions are such that the next-nearest-neighbor (NNN) exchange is antiferromagnetic (AFM), the nearest-neighbor (NN) exchange is ferromagnetic (FM), and the NNN spin exchange is often considerably stronger than the NN spin exchange. Due to the inherent competition of the NN and NNN spin exchange interactions, the  $\text{CuX}_2$  ribbon chains tend to develop unusual AFM incommensurate spiral spin structures<sup>1-9</sup> and sometimes concomitantly multiferroic behavior.<sup>10-13</sup> These  $\text{CuX}_2$  ribbon chains are formed by linking  $\text{CuX}_4$  basal-square planes of axially elongated  $\text{CuX}_6$  ( $X=\text{O}, \text{Cl}, \text{Br}, \dots$ ) octahedra together via their trans edges.

The magnetic properties of the  $\text{CuX}_2$  ribbon chains are primarily determined by the ratio of the NN to NNN spin exchange parameters,  $J_{\text{nn}}$  and  $J_{\text{nnn}}$ , with  $\alpha = J_{\text{nn}}/J_{\text{nnn}}$ . However, at low temperatures additional interactions (e.g., smaller interchain spin exchange interactions) also become important. Interchain interactions usually drive the systems to long-range magnetic order, the exact details of which are often determined by additional weak magnetic anisotropies.<sup>2,14,15</sup>

Here we describe the magnetic and lattice properties of a new system, trippkeite,<sup>16</sup> featuring edge-sharing  $\text{CuO}_2$  ribbon chains. Trippkeite is an exceptional ribbon chain system because it shows a FM ground state below  $\sim 7.4$  K. Trippkeite is a natural mineral with the chemical composition  $\text{CuAs}_2\text{O}_4$ .

Trippkeite crystallizes in a tetragonal structure (space group  $P4_2/mbc$ ) with lattice parameters  $a = b = 8.592(4) \text{ \AA}$  and  $c = 5.573(4) \text{ \AA}$ .<sup>17</sup> The Cu atoms are coordinated by elongated oxygen octahedra (**Fig. 7.1a**), which connect via trans edges to form corrugated  $\text{CuO}_2$  ribbons. The O1 and O2 atoms are located at the apical and basal positions of the octahedra, respectively (**Fig. 7.1b**). The As atoms form  $\text{AsO}_3$  pyramids, which link the oxygen atoms in the basal planes with the apical oxygen atoms of neighboring chains such that the basal planes of neighboring chains are perpendicular to each other.<sup>17</sup>

Experimentally, inverse susceptibility was obtained shown in the (red) solid line in **Fig. 7.2**. The Curie-Weiss temperature was found to be  $39 \pm 1 \text{ K}$ , indicating predominant FM spin exchange interactions, as also found by the EPR measurement. Below  $\sim 8 \text{ K}$  the magnetization rises sharply (**Fig. 7.2**) indicative of a FM transition. The Curie temperature  $T_C$  obtained from the inflection point of the susceptibility curve amounts to  $T_C = 7.6 \pm 0.2 \text{ K}$ . An isothermal magnetization measured at  $1.85 \text{ K}$ , plotted in the upper inset of **Fig. 7.2**, reveals saturation of the magnetization above a field of  $\sim 2.5 \text{ T}$  with a value of  $1.05 \pm 0.01 \mu_B$ . This saturation moment is in good agreement with the expected  $\sim 1 \mu_B$  value for a  $S = 1/2$  system.

In our theoretical study, the intrachain spin exchange interactions,  $J_{nn}$  and  $J_{nnn}$ , of  $\text{CuAs}_2\text{O}_4$  were evaluated by performing energy-mapping analyses<sup>18,19</sup> based on first-principles DFT calculations for the three ordered spin states depicted in **Fig. 7.3**. The energies of the three order states can be written in terms of the Heisenberg spin Hamiltonian

$$H = -\sum_{ij} J_{ij} \hat{S}_i \cdot \hat{S}_j, \quad (1)$$

where  $J_{ij}$  are the exchange parameters for the coupling between spin sites  $i$  and  $j$ . According to the energy expressions for spin dimers with  $N$  ( $=1$  in this case) unpaired spins per spin site,<sup>20,21</sup> the total spin exchange energies of the three ordered spin states, per eight formula units (FUs), are expressed as following:

$$\begin{aligned} \text{FM} &= 8J_1 + 8J_2 \\ \text{AF1} &= -8J_1 + 8J_2 \\ \text{AF2} &= 0J_1 - 8J_2 \end{aligned}$$

We calculated the electronic energies of the three ordered spin states by employing the projected augmented-wave (PAW) method<sup>22,23</sup> encoded in the Vienna *ab initio* simulation package (VASP)<sup>24</sup> and the generalized gradient approximation (GGA) for the exchange and correlation functional.<sup>25</sup> The plane-wave cutoff energy was set to 400 eV, and a set of 18 k points for the irreducible Brillouin zone was used. To probe the effect of electron correlations associated with the Cu 3d state, we performed DFT plus on-site repulsion (DFT+U) calculations with  $U_{\text{eff}} = 0, 4, 6$  and 8 eV for Cu.<sup>26</sup> By mapping the relative energies of the three ordered spin states obtained from our DFT+U calculations onto the corresponding Heisenberg Hamiltonian [**Equation (1)**], we obtain the values of the nearest- and next-nearest-neighbor spin exchange parameters,  $J_{\text{nn}} (\equiv J_1)$  and  $J_{\text{nnn}} (\equiv J_2)$ .

The results summarized in **Table 7.1** show that the FM-NN spin exchange dominates over the AFM-NNN spin exchange. As shown in **Fig. 7.4**, the ratio of the NN over the NNN spin exchanges increases with increasing  $U_{\text{eff}}$  values used in the DFT+U calculations. In general, the spin exchange  $J$  between two spin sites (say, 1 and 2 represented by the magnetic orbitals  $\phi_1$  and  $\phi_2$ , respectively) is written as  $J = J_{\text{F}} + J_{\text{AF}}$ . The FM component

$J_F$  increases when increasing the overlap density  $\phi_1 \phi_2$  while the AFM component  $J_{AF}$  is proportional to  $t^2$  and inversely proportional to  $U_{\text{eff}}$ .<sup>18, 19</sup> The magnetic orbital,  $x^2 - y^2$  orbital, of the  $\text{Cu}^{2+}$  ion has large O  $2p$  contributions. The strong FM-NN interaction in  $\text{CuAs}_2\text{O}_4$  is traced to the fact that the bond angle of the Cu-O-Cu superexchange path is close to  $90^\circ$  ( $\sim 91.5^\circ$ ) and the magnetic orbitals of the NN  $\text{Cu}^{2+}$  ions lead to a large overlap density around the bridging oxygen atoms.<sup>19</sup> The weaker AFM-NNN interaction is a consequence of the twisting of the  $\text{CuO}_2$  ribbon chains since it reduces the hopping integral between the NNN  $\text{Cu}^{2+}$  ions.

The Curie Weiss temperatures listed in **Table 7.1** were calculated with the equation

$$\Theta_{\text{CW}} = \frac{1}{3} S(S+1) \sum_i z_i J_i \quad (2)$$

The  $J_i$ 's represent the NN and the NNN spin exchange interactions along the ribbon chains,  $J_{\text{nn}}$  and  $J_{\text{nnn}}$ , respectively.  $z_i$  is the number of neighbors with spin exchange  $J_i$  in the NN and NNN shell,  $z_{\text{nn}} = z_{\text{nnn}} = 2$  for  $\text{CuAs}_2\text{O}_4$ .  $\Theta_{\text{CW}}$  is positive if the spin exchange is predominantly FM. The calculated Curie-Weiss temperatures are positive, consistent with the experimental findings.

In summary, we have investigated the magnetic and lattice properties of  $\text{CuAs}_2\text{O}_4$ , a system characterized by axially elongated  $\text{CuO}_6$  octahedra linking to form  $\text{CuO}_2$  ribbon chains. *Ab initio* DFT calculations show that the nearest-neighbor intrachain spin exchange interaction is FM with a magnitude  $\sim 4$  times larger than the next-nearest-neighbor AFM spin exchange interaction. Long-range FM ordering due to smaller interchain spin exchange

interactions is found below  $\sim 7.4$  K in the magnetization and heat capacity measurements. We observe that an application of external pressure increases the Curie temperature by a rate of  $\sim 1.4$  K/GPa, possibly due to an increase of the ferromagnetic nearest-neighbor spin exchange interaction. Raman scattering measurements show that the crystal structure is preserved across the  $T_C$  and down to 4 K.

## References

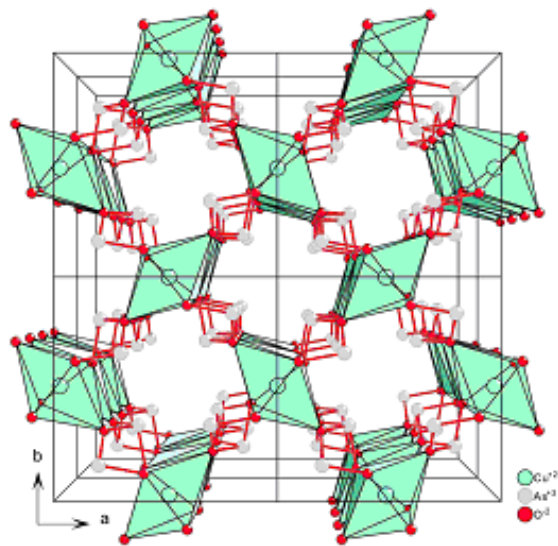
1. B. J. Gibson, R. K. Kremer, A. V. Prokofiev, W. Assmus, G. J. McIntyre. *Physica B*, **2004**, 350, e253.
2. M. Enderle, C. Mukherjee, B. Fåk, R. K. Kremer, J.-M. Broto, H. Rosner, S.-L. Drechsler, J. Richter, J. Malek, A. Prokofiev, W. Assmus, S. Pujol, J.-L. Raggazzoni, H. Rakoto, M. Rheinstädter, H. M. Rønnow. *Europhys. Lett.* **2005**, 70, 237.
3. L. Capogna, M. Mayr, P. Horsch, M. Raichle, R. K. Kremer, M. Sofin, A. Maljuk, M. Jansen, B. Keimer. *Phys. Rev. B.* **2005**, 71, 140402(R).
4. M. G. Banks, R. K. Kremer, C. Hoch, A. Simon, B. Ouladdiaf, J.-M. Broto, H. Rakoto, C. Lee, M.-H. Whangbo, *Phys. Rev. B.* **2009**, 80, 024404.
5. J. M. Law, P. Reuvekamp, R. Glaum, C. Lee, J. Kang, M.-H. Whangbo, R. K. Kremer, *Phys. Rev. B.* **2011**, 84, 014426.
6. S.-L. Drechsler, J. Richter, R. Kuzian, J. Malek, N. Tristan, B. Büchner, A. S. Moskvine, A. A. Gippius, A. Vasiliev, O. Volkova, A. Prokofiev, H. Rakoto, J.-M. Broto, W. Schnelle, M. Schmitt, A. Ormeci, C. Loison, H. Rosner. *J. Mag. Mater.* **2007**, 316, 306.
7. C. Lee, Jia Liu, M.-H. Whangbo, H.-J. Koo, R. K. Kremer, A. Simon. *Phys. Rev. B.* **2012**, 86, 060407.
8. B. Willenberg, M. Schäpers, K. C. Rule, S. Söllow, M. Reehuis, H. Ryll, B. Klemke, K. Kiefer, W. Schottenhamel, B. Büchner, B. Ouladdiaf, M. Uhlarz, R. Beyer, J. Wosnitza, A. U. B. Wolter. *Phys. Rev. Lett.* **2012**, 108, 117202.
9. A. U. B. Wolter, F. Lipps, M. Schäpers, S.-L. Drechsler, S. Nishimoto, R. Vogel, V.

- Kataev, B. B üchner, H. Rosner, M. Schmitt, M. Uhlarz, Y. Skourski, J. Wosnitza, S. Süllo, K. C. Rule. *Phys. Rev. B.* **2012**, 85, 014407.
10. Y. Naito, K. Sato, Y. Yasui, Y. Kobayashi, M. Sato. *J. Phys. Soc. Jpn.* **2007**, 76, 023708.
  11. F. Schrettle, S. Krohns, P. Lunkenheimer, J. Hemberger, N. B üttgen, H.-A. Krug von Nidda, A. V. Prokofiev, A. Loidl. *Phys. Rev. B.* **2008**, 77, 144101.
  12. Y. Yasui, Y. Naito, K. Sato, T. Moyoshi, M. Sato, K. Kakurai. *J. Phys. Soc. Jpn.* **2008**, 77, 023712.
  13. L. Zhao, T.-L. Hung, C.-C. Li, Y.-Y. Chen, M.-K. Wu, R. K. Kremer, M. G. Banks, A. Simon, M.-H. Whangbo, C. Lee, J. S. Kim, I. Kim, K. H. Kim. *Adv. Mater.* **2012**, 24, 2469.
  14. M. Mourigal, M. Enderle, R. K. Kremer, J. M. Law, B. Fåk. *Phys. Rev. B.* **2011**, 83, 100409(R).
  15. M. Mourigal, M. Enderle, B. Fåk, R. K. Kremer, J. M. Law, A. Schneidewind, A. Hiess, A. Prokofiev. *Phys. Rev. Lett.* **2012**, 109, 027203.
  16. K. Caslin, R. K. Kremer, F. S. Razavi, A. Schulz, A. Muñoz, F. Pertlik, J. Liu, M.-H. Whangbo, J. M. Law. *Phys. Rev. B.* **2014**, 89, 014412.
  17. F. Pertlik. *TMPM Tschermaks Min. Petr. Mitt.* **1975**, 22, 211.
  18. M. Whangbo, H. Koo, and D. Dai. *J. Solid State Chem.* **2003**, 176, 417.
  19. H. J. Xiang, C. Lee, H.-J. Koo, X. G. Gong, and M.-H. Whangbo, *Dalton Trans.* **2013**, 42, 823.
  20. D. Dai and M. Whangbo. *J. Chem. Phys.* **2001**, 114, 2887.
  21. D. Dai and M. Whangbo. *J. Chem. Phys.* **2003**, 118, 29.

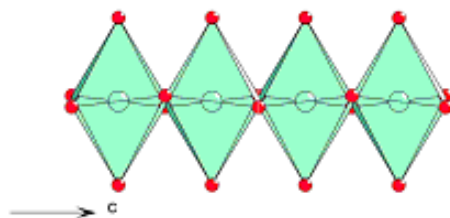
22. P. E. Blöchl. *Phys. Rev. B.* **1994**, 50, 17953.
23. G. Kresse and D. Joubert. *Phys. Rev. B.* **1999**, 59, 1758.
24. G. Kresse and J. Furthmüller. *Phys. Rev. B.* **1996**, 54, 11169.
25. J. P. Perdew, A. Ruzsinszky, G. I. Csonka, O. A. Vydroz, G. E. Scuseria, L. A. Constantin, X. L. Zhou, K. Burke, *Phys. Rev. Lett.* **2008**, 100, 136406.
26. S. L. Dudarev, G. A. Botton, S. Y. Savrasov, C. J. Humphreys, and A. P. Sutton, *Phys. Rev. B.* **1998**, 57, 1505.

**Table 7.1** Values of the NN and NNN spin exchange constants,  $J_{nn}$  and  $J_{nnn}$ , respectively, obtained from the DFT+ $U$  calculations along with the Curie-Weiss temperatures.

$U_{\text{eff}}$ (eV)	$J_{nn}$ (K)	$J_{nnn}$ (K)	$\Theta_{\text{CW}}$ (K)
<b>0</b>	42.3	-25.9	8.2
<b>4</b>	38.8	-13.5	12.7
<b>6</b>	34.0	-10.0	12.0
<b>8</b>	27.5	-7.1	10.2



(a)



(b)

**Fig. 7.1** (a) Projection along the [001] direction of the trippkeite crystal structure. The  $\text{Cu}^{2+}$  atoms are represented by the large (green) spheres, the oxygen atoms by small (red) spheres, and the As atoms by (gray) medium spheres. (b) A corrugated chain of trans-edge connected  $\text{CuO}_6$  octahedra highlighting the twisted basal planes of the octahedra in  $\text{CuAs}_2\text{O}_4$ , which lead to a corrugation of the  $\text{CuO}_2$  ribbon chains.

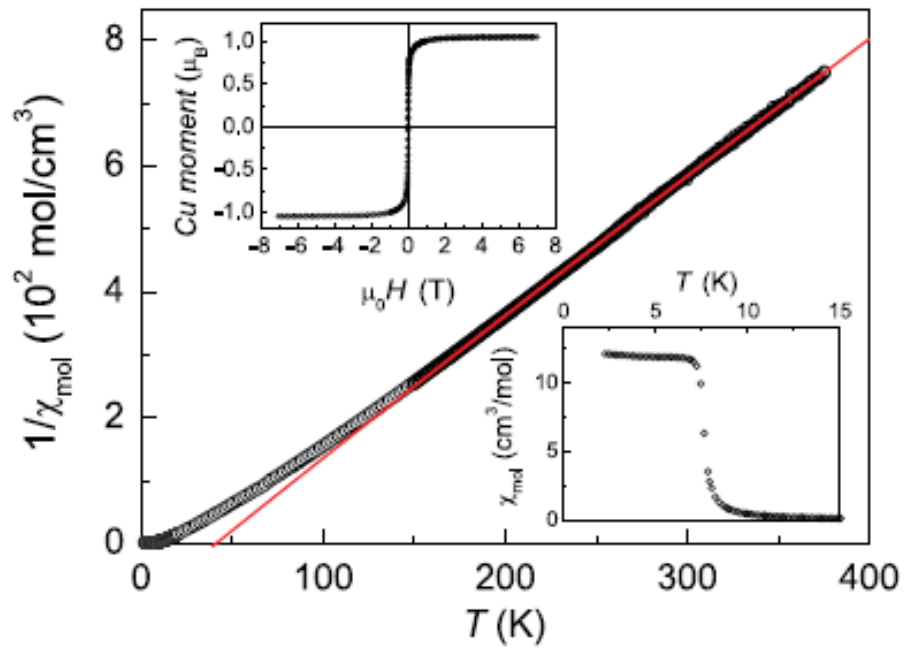


**Fig. 7.2** Reciprocal magnetic susceptibility of a polycrystalline  $\text{CuAs}_2\text{O}_4$  sample measured in a field of 1 T. The solid (red) line is a fit of the Curie-Weiss law to the data above 150 K. The lower inset shows the data below 20 K, collected at 0.01 T, in an enlarged scale. The upper inset displays the magnetization versus field collected at 1.85 K.

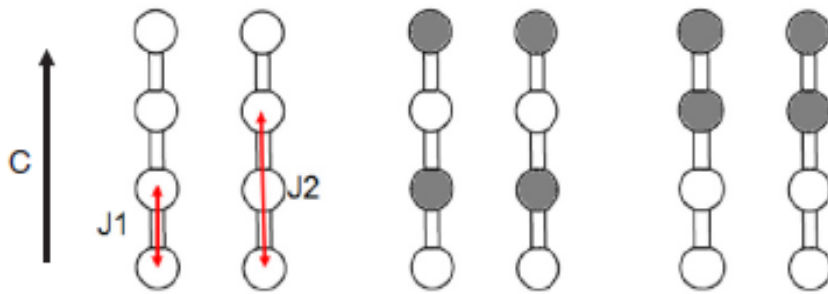


**Fig. 7.3** Three order spin states of  $\text{CuAs}_2\text{O}_4$  used to determine the values of  $J_{nn}$  ( $\equiv J_1$ ) and  $J_{nnn}$  ( $\equiv J_2$ ) by DFT+U calculations. Only the Cu sites are shown for simplicity. The unfilled and filled circles represent up-spin and down-spin  $\text{Cu}^{2+}$  sites, respectively.

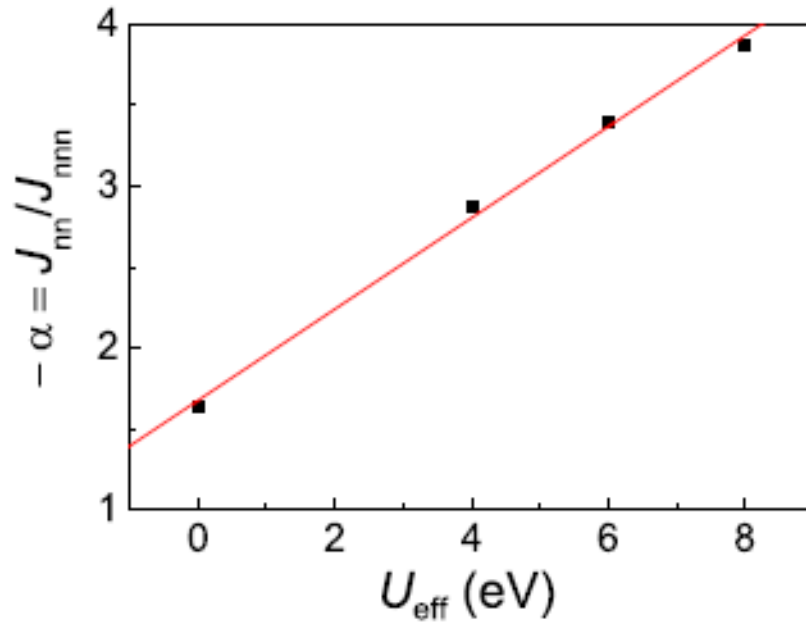


**Fig. 7.4** The ratio of the NN to NNN spin exchange constants of  $\text{CuAs}_2\text{O}_4$  calculated from the DFT+U calculations as a function of  $U_{\text{eff}}$ . The plot displays the dominance of the FM  $J_{\text{nn}}$  term over the AFM  $J_{\text{nnn}}$  term.

## 8. Quasi-one-dimensional spin chain system $\text{ACo}_2\text{V}_2\text{O}_8$ (A = Sr, Ba, Pb)

$\text{ACo}_2\text{V}_2\text{O}_8$  (A = Sr, Ba, Pb) consists of axially-compressed  $\text{CoO}_6$  octahedra and  $\text{VO}_4$  tetrahedra. The  $\text{CoO}_6$  octahedra containing  $\text{Co}^{2+}$  ( $d^7$ ,  $S = 3/2$ ) share their *cis* edges to form spiral chains running along the c-axis (**Figs. 8.1a** and **8.1b**) such that the short Co-O axial bonds are nearly parallel to the c-axis, and the  $\text{CoO}_6$  octahedra within and between spiral chains are connected by  $\text{VO}_4$  tetrahedra containing  $\text{V}^{5+}$  ions to form the 3D framework of  $\text{ACo}_2\text{V}_2\text{O}_8$  (**Figs. 8.1a** and **8.1c**) while the  $\text{A}^{2+}$  ions located at the cavities of the framework.<sup>1,2</sup>

The magnetic susceptibility and the specific heat data of  $\text{SrCo}_2\text{V}_2\text{O}_8$  and  $\text{BaCo}_2\text{V}_2\text{O}_8$  (**Figs. 8.2** and **8.3**, respectively)<sup>1</sup> show that they undergo a 3D AFM ordering below 6 K.<sup>1</sup> The high field magnetization data for  $\text{BaCo}_2\text{V}_2\text{O}_8$  indicated that the intra-chain NN spin exchange  $J$  is  $-62.5$  K, whereas the intra-chain NNN exchange  $J'$  is  $+4.1$  K.<sup>3</sup> In the case of  $\text{SrCo}_2\text{V}_2\text{O}_8$ , the magnetic susceptibility, dc magnetization and heat capacity experiments by He *et al.* suggested that there occur two AFM transitions with spin canting leading to non-collinear spin arrangement at  $\sim 5$  and  $\sim 3$  K.<sup>4</sup> They suggested that the Dzyaloshinskii-Moriya (DM) interactions might be responsible for the canted spin arrangement.  $\text{PbCo}_2\text{V}_2\text{O}_8$  was found to undergo a canted AFM transition at 4 K,<sup>2</sup> which is believed to arise from the DM interactions as in  $\text{SrCo}_2\text{V}_2\text{O}_8$ . However, recently, Lejay *et al.* reported that  $\text{SrCo}_2\text{V}_2\text{O}_8$  undergoes only one AFM transition with no spin canting at 5 K, as in the case of  $\text{BaCo}_2\text{V}_2\text{O}_8$ .<sup>1</sup>

Here, we are primarily interested in the magnetic anisotropy of the three compounds  $\text{ACo}_2\text{V}_2\text{O}_8$  (A = Sr, Ba, Pb). The  $\text{CoO}_6$  octahedra with  $\text{Co}^{2+}$  ( $d^7$ ,  $S = 3/2$ ) ions are axially

compressed. If these octahedra are approximated by idealized octahedra with  $C_4$ -rotation along the axially-compressed Co-O bonds, the 3d states are split as indicated in **Fig. 8.4** so that the high-spin  $Co^{2+}$  ion leads to an unequally-filled degenerate level. The latter leads to uniaxial magnetism.<sup>5,6</sup> The real  $CoO_6$  octahedra do not possess  $C_4$ -rotational symmetry, so that the above reasoning is not exactly applicable. However, the magnetic susceptibility of  $ACo_2V_2O_8$  for  $H//c$  is much higher than that for  $H\perp c$ , with the  $c$ -axis corresponding the easy magnetic axis. Since the axially-compressed Co-O bonds are nearly parallel to the  $c$ -axis, it appears that the uniaxial magnetism expected from the idealized  $CoO_6$  octahedra (**Fig. 8.4**) provides the essential cause for the strong magnetic anisotropies observed for  $ACo_2V_2O_8$ . We have tested the validity of this reasoning by performing DFT+U and DFT+U+SOC calculations for  $ACo_2V_2O_8$ .

Our spin-polarized DFT calculations employed the projector augmented wave method encoded in the Vienna ab initio simulation package<sup>7</sup> and the generalized gradient approximation<sup>8</sup> for the exchange-correlation functionals with the plane wave cutoff energies of 400 eV, and the threshold of self-consistent-field (SCF) energy convergence of  $10^{-6}$  eV. To describe the electron correlation associated with the Co 3d states, we employed the DFT plus on-site repulsion U (DFT+U) method of Liechtenstein et al.<sup>9</sup> with an effective U = 2, 4 and 6 eV on the Co to examine the Projected Density of States (PDOS) (**Figs. 8.5, 8.6, 8.7**). Preferred spin orientations were also examined by DFT + U + SOC energy calculations and the results are shown in **Table 8.1**.

From our computational results, there is no doubt that the easy-axis anisotropy of the  $Co^{2+}$  spin in  $ACo_2V_2O_8$  (A = Sr, Ba, Pb) is an intrinsic property that is associated with SOC.

By using the coordinate systems  $(x, y, z)$  and  $(x', y', z')$  for the orbital and spin, respectively, the SOC Hamiltonian  $\hat{H}_{\text{SO}} = \lambda \hat{\mathbf{S}} \cdot \hat{\mathbf{L}}$  is expressed as <sup>10, 11</sup>

$$\begin{aligned} \hat{H}_{\text{SO}} = & \lambda \hat{\mathbf{S}}_{z'} \left( \hat{\mathbf{L}}_z \cos \theta + \frac{1}{2} \hat{\mathbf{L}}_+ e^{-i\varphi} \sin \theta + \frac{1}{2} \hat{\mathbf{L}}_- e^{i\varphi} \sin \theta \right) \\ & + \frac{\lambda}{2} \hat{\mathbf{S}}_{+'} \left( -\hat{\mathbf{L}}_z \sin \theta - \hat{\mathbf{L}}_+ e^{-i\varphi} \sin^2 \frac{\theta}{2} + \hat{\mathbf{L}}_- e^{i\varphi} \cos^2 \frac{\theta}{2} \right) \\ & + \frac{\lambda}{2} \hat{\mathbf{S}}_{-'} \left( -\hat{\mathbf{L}}_z \sin \theta + \hat{\mathbf{L}}_+ e^{-i\varphi} \cos^2 \frac{\theta}{2} - \hat{\mathbf{L}}_- e^{i\varphi} \sin^2 \frac{\theta}{2} \right) \end{aligned} \quad (1)$$

Thus  $\hat{H}_{\text{SO}}$  is rewritten as  $\hat{H}_{\text{SO}} = \hat{H}_{\text{SO}}^0 + \hat{H}'_{\text{SO}}$ , where  $\hat{H}_{\text{SO}}^0$  is the spin-conserving term (i.e., the first line of Eq. 1), and  $\hat{H}'_{\text{SO}}$  is the spin-non-conserving term (i.e., the second and third lines of Eq. 1). The preferred spin orientation (i.e., the  $z'$  axis) is along the  $z$ -axis (i.e.,  $\theta = 0^\circ$ ) for the easy-axis anisotropy, but perpendicular to the  $z$ -axis (i.e.,  $\theta = 90^\circ$ ) for the easy-plane anisotropy. The easy-plane anisotropy of the high-spin  $\text{Fe}^{2+}$  ( $d^6$ ,  $S = 2$ ) ions in  $\text{SrFeO}_2$  <sup>12</sup> and  $\text{Sr}_3\text{Fe}_2\text{O}_5$  <sup>13</sup> and the easy-axis anisotropy of the high-spin  $\text{Mn}^{3+}$  ( $d^4$ ,  $S = 2$ ) ions in  $\text{TbMnO}_3$  <sup>14</sup> and  $\text{Ag}_2\text{MnO}_2$  <sup>15</sup> are well explained on the basis of perturbation theory analysis using  $\hat{H}_{\text{SO}} = \lambda \hat{\mathbf{S}} \cdot \hat{\mathbf{L}}$  as perturbation and the crystal-field split  $d$ -states of a magnetic ion as unperturbed states. For example, when an occupied down-spin  $d$ -level  $i = \psi_o \downarrow$  with energy  $e_i$  interacts with an unoccupied down-spin  $d$ -level  $j = \psi_u \downarrow$  with energy  $e_j$  via the matrix element  $\langle i | \hat{H}_{\text{SO}}^0 | j \rangle$ , the associated energy lowering is given by

$$\Delta E_{\text{SOC}} = - \left| \langle i | \hat{H}_{\text{SO}}^0 | j \rangle \right|^2 / |e_i - e_j|.$$

In determining the preferred spin orientation, the most important interaction is the one with the smallest energy gap ( $e_i - e_j$ ). **Fig. 8.4** shows the approximate splitting pattern of the 3d level of  $\text{Co}^{2+}$  ion, in reality the  $xz$  and  $yz$  levels are not exactly equal in energy due to the different bond lengths in the  $\text{CoO}_6$  octahedra in all three compounds. As a result, the empty  $xz\downarrow$  and  $yz\downarrow$  states have the smallest energy gap with the filled  $xz\downarrow$  and  $yz\downarrow$  states. The interaction between these two states through  $\hat{H}_{\text{SO}}^0$  predicts the easy-axis anisotropy, because the matrix element  $\langle xz\downarrow | \hat{H}_{\text{SO}}^0 | yz\downarrow \rangle$  can be nonzero via the  $\hat{L}_z$  term of  $\hat{H}_{\text{SO}}^0$ , which come with the coefficient  $\cos\theta$ .

Results of our DFT + U + SOC in **Table 8.1** show that the SOC effect is more profound in the case of  $\text{BaCo}_2\text{V}_2\text{O}_8$  than in the  $\text{PbCo}_2\text{V}_2\text{O}_8$  and  $\text{SrCo}_2\text{V}_2\text{O}_8$ , which arises from the difference in the local  $\text{CoO}_6$  octahedra of the three compounds. The projected density of states (PDOS) plots obtained for the three compounds from DFT + U calculations are presented in **Figs. 8.5-8.7**, which show that the energy separation between the filled and empty  $xz\downarrow/yz\downarrow$  states is much smaller for  $\text{BaCo}_2\text{V}_2\text{O}_8$  than for  $\text{PbCo}_2\text{V}_2\text{O}_8$  and  $\text{SrCo}_2\text{V}_2\text{O}_8$ . Therefore, the associated energy gain  $\Delta E_{\text{SOC}} = -\frac{|\langle i | \hat{H}_{\text{SO}}^0 | j \rangle|^2}{|e_i - e_j|}$  is greater for  $\text{BaCo}_2\text{V}_2\text{O}_8$  than for  $\text{PbCo}_2\text{V}_2\text{O}_8$  and  $\text{SrCo}_2\text{V}_2\text{O}_8$  leading to a stronger easy axis anisotropy for  $\text{BaCo}_2\text{V}_2\text{O}_8$ .

## References

1. Lejay, P.; Canevet, E.; Srivastava, S.K.; Grenier, B.; Klanjsek, M.; Berthier, C. *Journal of Crystal Growth* **2011**, *317*, 128-131.
2. He, Z.; Ueda, Y.; Itoh, M. *Journal of Solid State Chem.* **2007**, *180*, 1770-1774.
3. Kimura, S.; Yashiro, H.; Okunishi, K; Hagiwara, M.; He, Z.; Kindo, K.; Taniyama, T.; Itoh, M. *Phys. Rev. Lett.* **2007**, *99*, 087602.
4. He, Z.; Ueda, Y.; Itoh, M. *Solid State Comm.* **2007**, *142*, 404-406.
5. Dai, D; Whangbo, M.-H. *Inorg. Chem.* **2005**, *44*, 4407- 4414.
6. Zhang. Y.; Xiang, H.J.; Whangbo, M.-H. *Phys. Rev. B.* **2009**, *79*, 054432.
7. (a) G. Kresse and J. Hanfner, *Phys. Rev. B.* **1993**, *47*, 558. (b) G. Kresse and J. Furthmüller, *Comput. Mater. Sci.* **1996**, *6*, 15. (c) G. Kresse and J. Furthmüller, *Phys. Rev. B.* **1996**, *54*, 11169.
8. J. P. Perdew, S. Burke and M. Ernzerhof, *Phys. Rev. Lett.* **1996**, *77*, 3865.
9. A. I. Liechtenstein, V. I. Anisimov and J. Zaanen, *Phys. Rev. B.* **1995**, *52*, 5467.
10. D. Dai, H. J. Xiang and M.-H. Whangbo, *J. Comput. Chem.* **2008**, *29*, 2187.
11. X. Wang, R. Wu, D.-S. Wang and A. J. Freeman, *Phys. Rev. B.* **1996**, *54*, 61.
12. H. J. Xiang, S.-H. Wei and M.-H. Whangbo, *Phys. Rev. Lett.* **2008**, *100*, 167207.
13. H.-J. Koo, H. J. Xiang, C. Lee and M.-H. Whangbo, *Inorg. Chem.* **2009**, *48*, 9051.
14. H. J. Xiang, S.-H. Wei, M.-H. Whangbo and J. L. F. Da Silva, *Phys. Rev. Lett.* **2008**, *101*, 037209.
15. S. Ji, E. J. Kan, M.-H. Whangbo, J.-H. Kim, Y. Qiu, M. Matsuda, H. Yoshida, Z. Hiroi, M. A. Green, T. Ziman, and S.-H. Lee, *Phys. Rev. B.* **2010**, *81*, 094421.

**Table. 8.1** Energy difference ( $E_{\perp c} - E_{//c}$ ), in meV/Co, obtained from DFT+U+SOC (with  $U = 2, 4, 6$  eV) calculations for the FM states ( $\uparrow\uparrow\uparrow\uparrow$ ) of  $\text{BaCo}_2\text{V}_2\text{O}_8$ ,  $\text{PbCo}_2\text{V}_2\text{O}_8$  and  $\text{SrCo}_2\text{V}_2\text{O}_8$ , where ( $E_{\perp c} - E_{//c}$ ) refer to the energies for the  $\perp c$  and  $//c$  spin orientations, respectively.

	<b>U = 2 eV</b>	<b>U = 4 eV</b>	<b>U = 6 eV</b>
<b>BaCo<sub>2</sub>V<sub>2</sub>O<sub>8</sub></b>	1.59	1.34	1.25
<b>PbCo<sub>2</sub>V<sub>2</sub>O<sub>8</sub></b>	0.46	0.24	0.14
<b>SrCo<sub>2</sub>V<sub>2</sub>O<sub>8</sub></b>	0.93	0.56	0.39

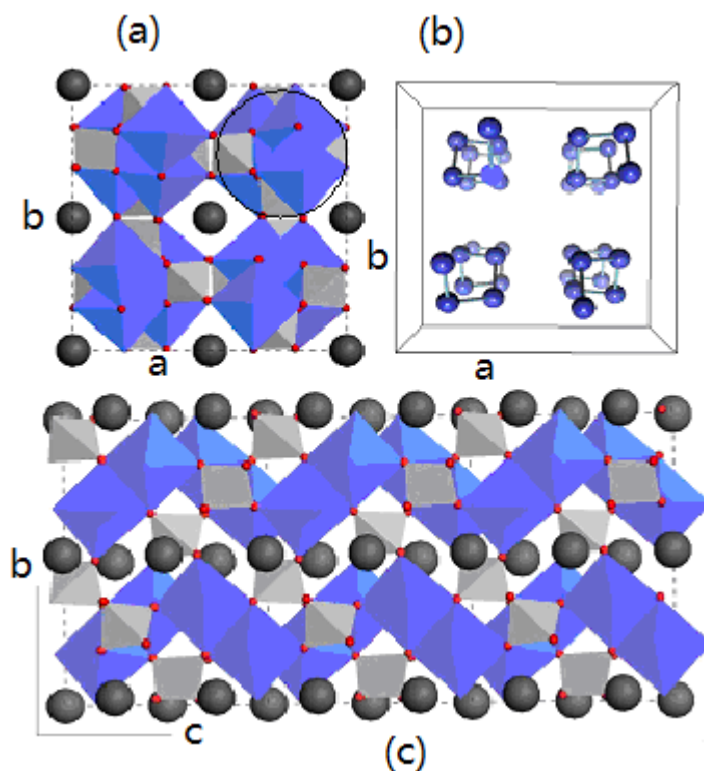


**Fig. 8.1** (a) Projection view of  $\text{ACo}_2\text{V}_2\text{O}_8$  ( $A = \text{Sr}, \text{Ba}, \text{Pb}$ ) on the  $ab$ -plane. The octahedra, tetrahedra, large ball and small ball represent  $\text{CoO}_6$ ,  $\text{VO}_4$ ,  $A$ , and  $\text{O}$ , respectively. The circle shows the  $\text{Co}_4\text{V}_4\text{O}_{16}$  cluster of a unit cell. (b) Perspective view of the  $\text{Co}^{2+}$  arrangements along the  $c$ -direction. (c) Projection view of  $\text{ACo}_2\text{V}_2\text{O}_8$  on the  $bc$ -plane.

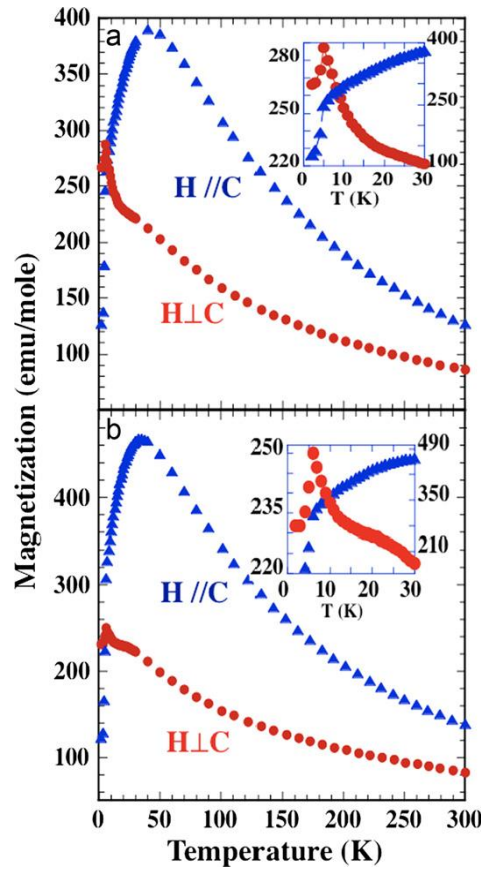


**Fig. 8.2** Temperature variation of magnetization for (a) SrCo<sub>2</sub>V<sub>2</sub>O<sub>8</sub> and (b) BaCo<sub>2</sub>V<sub>2</sub>O<sub>8</sub> in an applied magnetic field of 5 KOe. The inset shows a zoomed-in view in 2 – 30 K range.

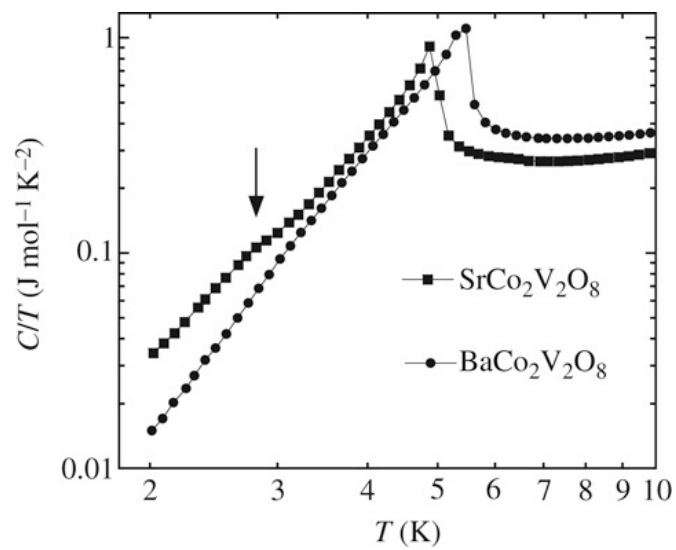


**Fig. 8.3** Specific heats of  $\text{SrCo}_2\text{V}_2\text{O}_8$  and  $\text{BaCo}_2\text{V}_2\text{O}_8$  measured in zero magnetic field.

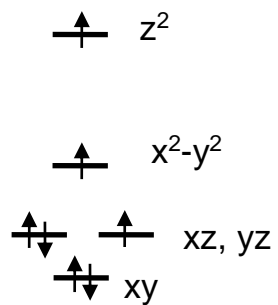


**Fig. 8.4** Split pattern of the d-states of a high-spin  $\text{Co}^{2+}$  ion in an axially-compressed  $\text{CoO}_6$  octahedron with the  $C_4$ -rotational symmetry.

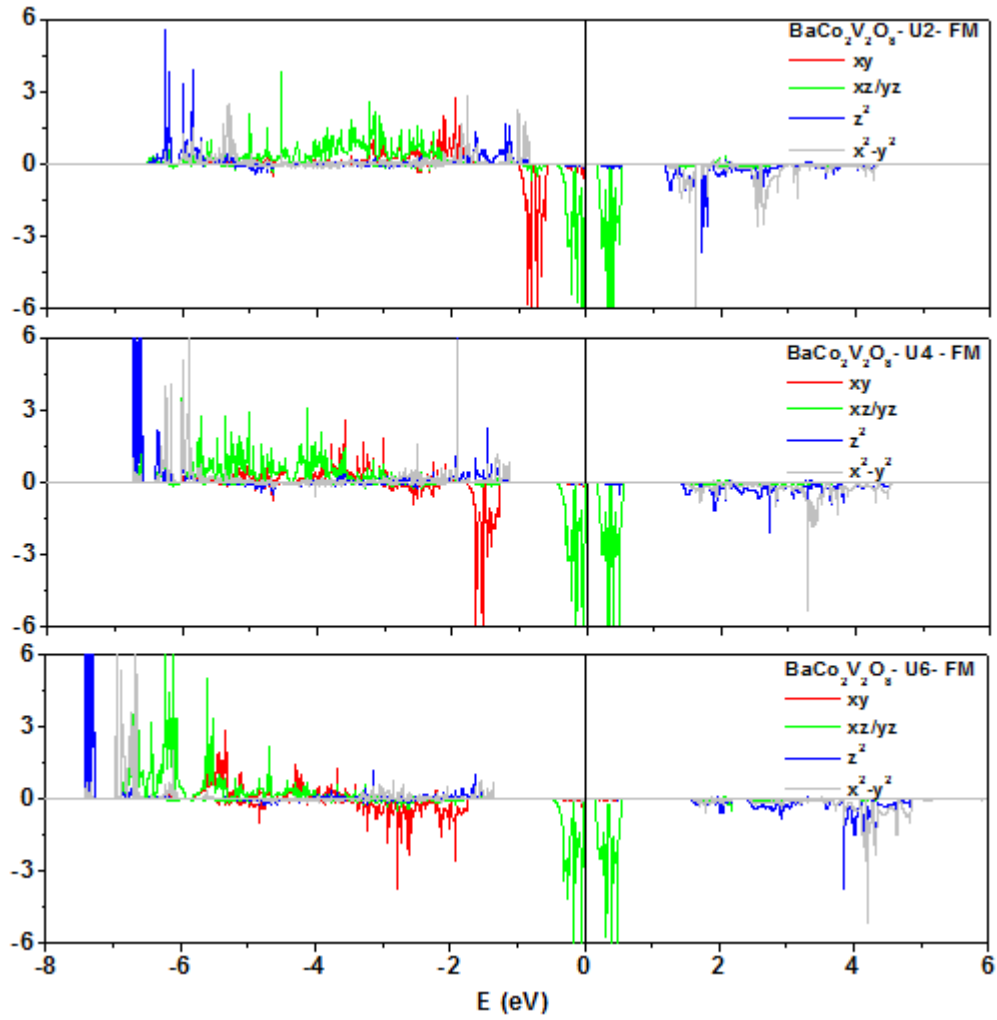


**Fig. 8.5** PDOS plots obtained for the Co 3d states of  $\text{BaCo}_2\text{V}_2\text{O}_8$  from DFT+ $U$  ( $U = 2, 4, 6$  eV) calculations for the FM state.

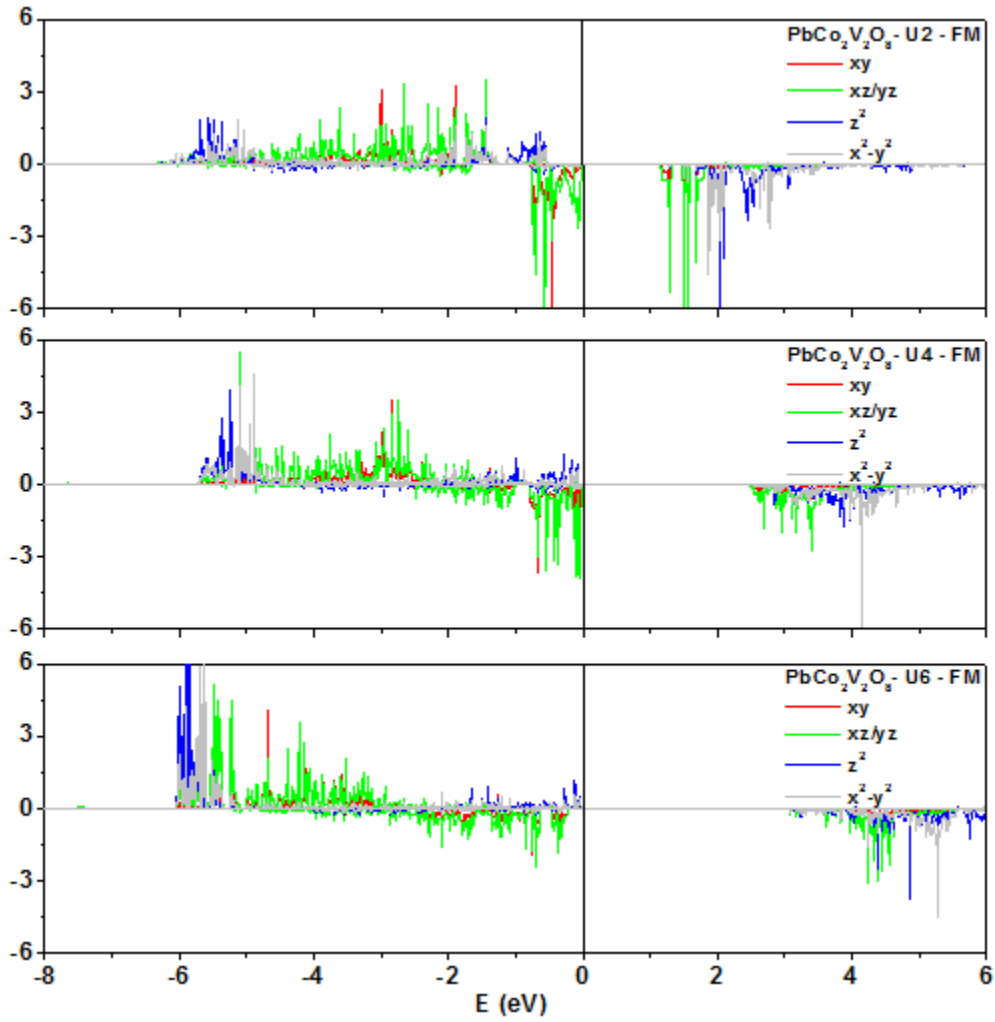


**Fig. 8.6** PDOS plots obtained for the Co 3d states of  $\text{PbCo}_2\text{V}_2\text{O}_8$  from DFT+U ( $U = 2, 4, 6$  eV) calculations for the FM state.

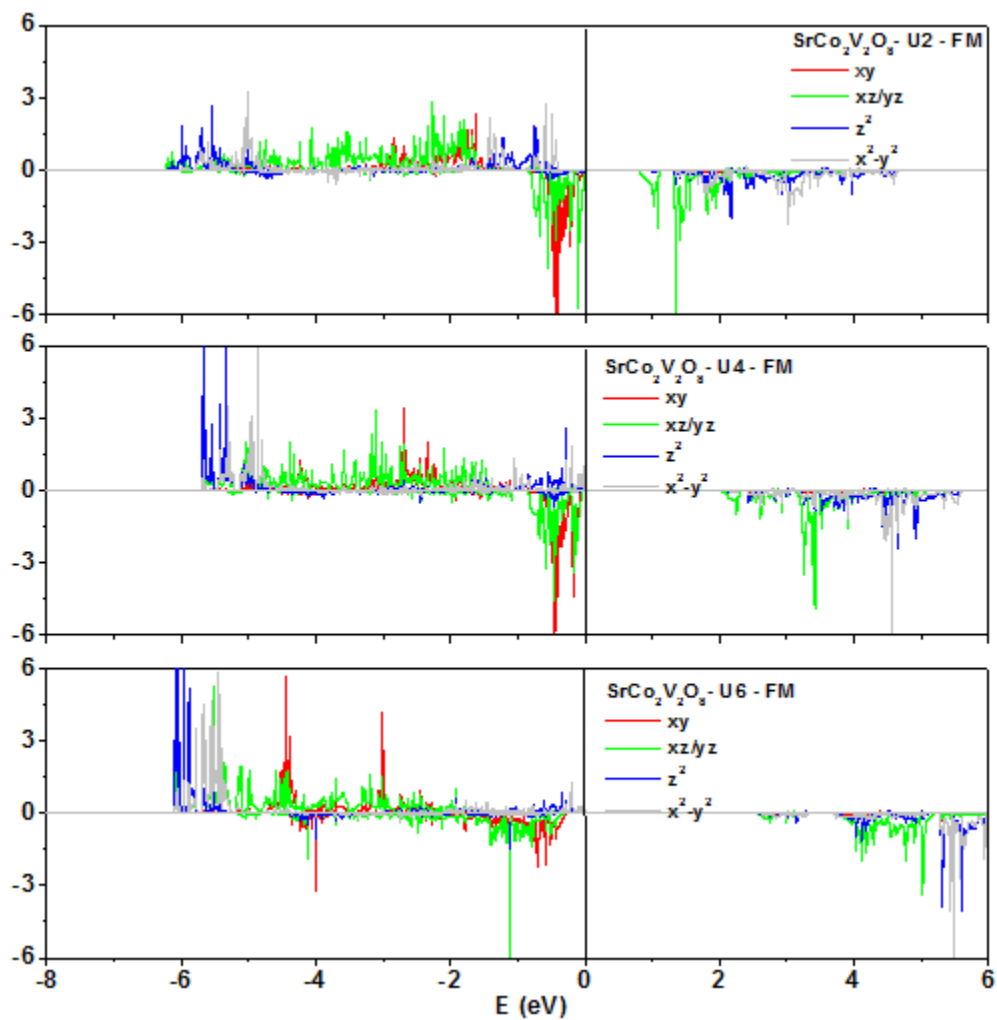


**Fig. 8.7** PDOS plots obtained for the Co 3d states of  $\text{SrCo}_2\text{V}_2\text{O}_8$  from DFT+U ( $U = 2, 4, 6$  eV) calculations for the FM state.

## 9. Single ion anisotropy of spin-1/2 systems

It is commonly believed that spin-1/2 transition-metal ions have no single-ion anisotropy (SIA), i.e., the spin-orbit coupling (SOC) associated with their crystal-field split d-states leads to no preferred spin orientation.<sup>1</sup> Thus the spin orientation observed for such ions is explained by invoking anisotropic spin exchange (ASE) or magnetic dipole-dipole (MDD) interactions between these ions, as found in the classic study of the  $\text{Cu}^{2+}$  ( $S = 1/2$ ) spin orientation in  $\text{CuCl}_2 \cdot 2\text{H}_2\text{O}$ .<sup>1a</sup> This conventional belief arises from the effective spin approximation,<sup>2</sup> in which magnetic ions are treated as spin-only ions and the effect of their remnant orbital moments is included in anisotropic g-factors.<sup>2,3</sup> For a magnetic ion with nondegenerate magnetic orbital (e.g.,  $\text{Cu}^{2+}$ ), the effective spin approximation reduces the SOC Hamiltonian  $\hat{H}_{\text{SO}} = \lambda \hat{S} \cdot \hat{L}$  to the zero-field Hamiltonian,

$$\hat{H}_{\text{zf}} = D \left( \hat{S}_z^2 - \frac{1}{3} \hat{S}^2 \right) + \frac{1}{2} E \left( \hat{S}_+ \cdot \hat{S}_+ + \hat{S}_- \cdot \hat{S}_- \right),$$

where the constants D and E are related to the unquenched orbital angular momenta along the three local directions of the ion.<sup>3</sup> For a spin-1/2 ion, the up-spin state  $|\uparrow\rangle = \left| \frac{1}{2}, \frac{1}{2} \right\rangle$  does not interact with the down-spin state  $|\downarrow\rangle = \left| \frac{1}{2}, -\frac{1}{2} \right\rangle$  under  $\hat{H}_{\text{zf}}$  so that the two states remain degenerate (as demanded by Kramers degeneracy theorem for odd-spin ions,<sup>4</sup> leading to the belief that spin-1/2 ions do not possess SIA. That the effective spin approximation cannot describe the magnetocrystalline anisotropy of a spin-1/2 ion was already pointed out in the study<sup>5</sup> of  $\text{Y}_2\text{V}_2\text{O}_7$  containing  $\text{V}^{4+}$  ( $d^1$ ,  $S = 1/2$ ) ions at slightly-distorted octahedral sites. Surprisingly, there has been no systematic investigation concerning whether a spin-1/2 ion

has no SIA in the absence of the effective spin approximation. In this section we probe this question by examining the cause for the observed spin orientations of the  $\text{Cu}^{2+}$  ( $S = 1/2$ ) ions in  $\text{CuCl}_2 \cdot 2\text{H}_2\text{O}$ ,  $\text{LiCuVO}_4$ ,  $\text{CuCl}_2$  and  $\text{CuBr}_2$ , in which the  $\text{Cu}^{2+}$  ions are located at square-planar sites. On the basis of density functional theory (DFT) calculations, MDD energy calculations, and perturbation theory analysis using  $\hat{H}_{\text{SO}}$  as perturbation, we show that the preferred orientation of the  $\text{Cu}^{2+}$  spins is not caused by their ASE interactions, nor by their MDD interactions, but by their SIA.

Our spin-polarized DFT calculations employed the projector augmented wave method encoded in the Vienna ab initio simulation package <sup>6</sup> and the generalized gradient approximation <sup>7</sup> for the exchange-correlation functionals with the plane wave cutoff energies of 400 eV, and the threshold of self-consistent-field (SCF) energy convergence of  $10^{-8}$  eV. To describe the electron correlation associated with the Cu 3d states, we employed the DFT plus on-site repulsion U (DFT+U) method of Liechtenstein et al. <sup>8</sup> with an effective  $U_{\text{eff}} = U - J = 4, 5$  and 6 eV on the Cu atom and the exchange-correction  $J = 1$  eV since our calculations include noncollinear magnetic structures as well. <sup>9</sup> Preferred spin orientations were also examined by MDD energy calculations. <sup>10</sup> In summing the MDD interactions between various pairs of spin sites, we employed the Ewald summation method. <sup>11</sup>

In the Pmna setting of the crystal structure of  $\text{CuCl}_2 \cdot 2\text{H}_2\text{O}$ , isolated  $\text{CuCl}_2(\text{OH}_2)_2$  complexes form skewed stacks along the b-direction (**Fig. 9.1a**), <sup>12</sup> and in each  $\text{CuCl}_2(\text{OH}_2)_2$  complex the linear O-Cu-O unit is perpendicular to the linear Cl-Cu-Cl unit. The spin at each  $\text{Cu}^{2+}$  site is oriented along the Cu-O bond (i.e., lies in the  $\text{CuCl}_2\text{O}_2$  plane), and the  $\text{Cu}^{2+}$  spins

have an antiferromagnetic (AFM) coupling within each skewed stack but a ferromagnetic (FM) coupling between adjacent stacks (**Fig. 9.1b**).<sup>13</sup> We examine the cause for this easy-plane anisotropy as described below.

(1) We design an “isolated  $\text{Cu}^{2+}$  ion” model (Model I) by substituting  $\text{Mg}^{2+}$  ions for  $\text{Cu}^{2+}$  ions such that a  $2 \times 3 \times 2$  supercell containing one  $\text{Cu}^{2+}$  ion repeats. The local coordinate axes of an isolated  $\text{CuCl}_2(\text{OH}_2)_2$  complex were chosen as depicted in **Fig. 9.1c**. Our DFT+U+SOC calculations for the “isolated  $\text{Cu}^{2+}$  ion” model with the spin orientations taken along the Cu-O bonds (i.e.,  $\parallel xy$ ) and perpendicular to the  $\text{CuCl}_2\text{O}_2$  plane (i.e.,  $\perp xy$ ) show that the  $\parallel xy$  orientation is more stable than the  $\perp xy$  orientation (**Table 9.1**). This indicates that the easy-plane anisotropy is an intrinsic property of an isolated  $\text{CuCl}_2(\text{OH}_2)_2$  complex, because both the spin exchange and MDD interactions between adjacent  $\text{Cu}^{2+}$  ions are negligible in this “isolated  $\text{Cu}^{2+}$  ion” model.

(2) We construct an “isolated  $\text{Cu}^{2+}$  chain” model in which, of two chains per unit cell, all  $\text{Cu}^{2+}$  ions in one chain are replaced with nonmagnetic  $\text{Mg}^{2+}$  ions, and examine the  $\uparrow\downarrow\uparrow\downarrow$  and  $\uparrow\uparrow\downarrow\downarrow$  spin arrangements along the “isolated  $\text{Cu}^{2+}$  chain” (Models II and III, respectively). For each of these two spin arrangements, we carry out DFT+U+SOC calculations for the  $\parallel xy$  and  $\perp xy$  spin orientations. (In the  $\parallel xy$  spin orientation, the spin is aligned along the Cu-O bond, as found experimentally. See below for further discussion.) As for the spin exchange of the “isolated  $\text{Cu}^{2+}$  chain”, we consider only the nearest-neighbor exchange  $J_{nn}$  since the next-nearest-neighbor exchange  $J_{n nn}$  would be negligible owing to the long Cu...Cu distance involved. Given the AFM spin order along the stacking direction, we assume that the components  $J_{nn-x}$ ,  $J_{nn-y}$  and  $J_{nn-z}$  of the nearest-neighbor exchange are all AFM and use the

convention that a negative spin exchange constant represents an AFM interaction. The spin exchange interaction energy per spin site for the  $\uparrow\downarrow\uparrow\downarrow$  arrangement is given by

$$-J_{nn-x}S_{1x}S_{2x} - J_{nn-y}S_{1y}S_{2y} - J_{nn-z}S_{1z}S_{2z},$$

where two adjacent spin sites are labeled as 1 and 2 for convenience. Then, the  $\parallel xy$  spin orientation is explained if  $|J_{nn-x}|, |J_{nn-y}| > |J_{nn-z}|$ . In the  $\uparrow\uparrow\downarrow\downarrow$  arrangement the sum of the nearest-neighbor spin exchange interaction energies is zero, so the  $\parallel xy$  and  $\perp xy$  spin orientations would be similar in energy if the ASE interactions were the cause for the spin orientation. However, **Table 9.1** shows that the preference for the in-plane spin orientation is practically identical in both  $\uparrow\downarrow\uparrow\downarrow$  and  $\uparrow\uparrow\downarrow\downarrow$  arrangements, so the ASE interactions are not responsible for the easy-plane anisotropy of the  $\text{Cu}^{2+}$  ion.

(3) We use the “isolated  $\text{Cu}^{2+}$  chain” model to evaluate the values of  $J_{nn-x}$ ,  $J_{nn-y}$  and  $J_{nn-z}$  by using the energy-mapping analysis.<sup>14</sup> To obtain  $J_{nn-x}$ , we consider the FM and AFM spin arrangements with spins collinear to the x-direction. Representing the energies of these two state by  $E(\uparrow\uparrow)_x$  and  $E(\uparrow\downarrow)_x$ , respectively, we obtain  $J_{nn-x} = [E(\uparrow\uparrow)_x - E(\uparrow\downarrow)_x]/2$ . Thus  $J_{nn-x}$  is determined by obtaining the energy difference,  $E(\uparrow\uparrow)_x - E(\uparrow\downarrow)_x$ , on the basis of DFT+U+SOC calculations. The values of  $J_{nn-y}$  and  $J_{nn-z}$  are similarly determined;  $J_{nn-y} = [E(\uparrow\uparrow)_y - E(\uparrow\downarrow)_y]/2$ , and  $J_{nn-z} = [E(\uparrow\uparrow)_z - E(\uparrow\downarrow)_z]/2$ . Our results summarized in **Table 9.2**, show that there is practically no anisotropy in the spin exchange constants.

(4) The two spin directions of interest in the  $\parallel xy$  spin orientation are the Cu-O and Cu-Cl bond directions. Our DFT+U+SOC calculations for the “isolated  $\text{Cu}^{2+}$  chain” with FM spin arrangement show that the spin orientation along the Cu-O bond is more stable than that

along the Cu-Cl bond by 0.10, 0.08 and 0.07 meV/Cu for effective  $U_{\text{eff}} = 4, 5$  and 6 eV, respectively. The preference for the spin to orient along the Cu-O bond is in agreement with experiment.<sup>13</sup>

(5) We examine the MDD energies for two spin arrangements, namely, the  $\uparrow\downarrow\uparrow\downarrow$  and  $\uparrow\uparrow\downarrow\downarrow$  arrangements within each skewed stack of  $\text{Cu}^{2+}$  ions but with FM spin arrangement between adjacent stacks. For each of these spin arrangements, we calculate the MDD energies with the  $\parallel_{xy}$  and  $\perp_{xy}$  spin orientations to find that the energy difference,  $E_{\parallel xy} - E_{\perp xy}$ , between the two spin orientations is negligibly small (i.e., +0.005 and -0.014 meV/Cu for the  $\uparrow\downarrow\uparrow\downarrow$  and  $\uparrow\uparrow\downarrow\downarrow$  arrangements, respectively), which shows that MDD interactions cannot be responsible for the easy-plane anisotropy of the  $\text{Cu}^{2+}$  spin in  $\text{CuCl}_2 \cdot 2\text{H}_2\text{O}$ .

The above discussion shows beyond any doubt that the easy-plane anisotropy of the  $\text{Cu}^{2+}$  spin in  $\text{CuCl}_2 \cdot 2\text{H}_2\text{O}$  is an intrinsic property of an isolated  $\text{CuCl}_2(\text{OH}_2)_2$  complex that is associated with SOC. By using the coordinate systems  $(x, y, z)$  and  $(x', y', z')$  for the orbital and spin, respectively, the SOC Hamiltonian  $\hat{H}_{\text{SO}} = \lambda \hat{\mathbf{S}} \cdot \hat{\mathbf{L}}$  is expressed as<sup>3,15</sup>

$$\begin{aligned} \hat{H}_{\text{SO}} = & \lambda \hat{\mathbf{S}}_{z'} \left( \hat{L}_z \cos \theta + \frac{1}{2} \hat{L}_+ e^{-i\varphi} \sin \theta + \frac{1}{2} \hat{L}_- e^{i\varphi} \sin \theta \right) \\ & + \frac{\lambda}{2} \hat{\mathbf{S}}_{+'} \left( -\hat{L}_z \sin \theta - \hat{L}_+ e^{-i\varphi} \sin^2 \frac{\theta}{2} + \hat{L}_- e^{i\varphi} \cos^2 \frac{\theta}{2} \right) \\ & + \frac{\lambda}{2} \hat{\mathbf{S}}_{-'} \left( -\hat{L}_z \sin \theta + \hat{L}_+ e^{-i\varphi} \cos^2 \frac{\theta}{2} - \hat{L}_- e^{i\varphi} \sin^2 \frac{\theta}{2} \right) \end{aligned} \quad (1)$$

Thus  $\hat{H}_{\text{SO}}$  is rewritten as  $\hat{H}_{\text{SO}} = \hat{H}_{\text{SO}}^0 + \hat{H}'_{\text{SO}}$ , where  $\hat{H}_{\text{SO}}^0$  is the spin-conserving term (i.e., the first line of **Eq. 1**), and  $\hat{H}'_{\text{SO}}$  is the spin-non-conserving term (i.e., the second and third lines

of **Eq. 1**). Then the preferred spin orientation (i.e., the  $z'$  axis) is along the  $z$ -axis (i.e.,  $\theta = 0^\circ$ ) for the easy-axis anisotropy, but perpendicular to the  $z$ -axis (i.e.,  $\theta = 90^\circ$ ) for the easy-plane anisotropy. The easy-plane anisotropy of the high-spin  $\text{Fe}^{2+}$  ( $d^6$ ,  $S = 2$ ) ions in  $\text{SrFeO}_2$ <sup>16</sup> and  $\text{Sr}_3\text{Fe}_2\text{O}_5$ <sup>10</sup> and the easy-axis anisotropy of the high-spin  $\text{Mn}^{3+}$  ( $d^4$ ,  $S = 2$ ) ions in  $\text{TbMnO}_3$ <sup>17</sup> and  $\text{Ag}_2\text{MnO}_2$ <sup>18</sup> are well explained on the basis of perturbation theory analysis using  $\hat{H}_{\text{SO}} = \lambda \hat{S} \cdot \hat{L}$  as perturbation and the crystal-field split  $d$ -states of a magnetic ion as unperturbed states. For example, when an occupied down-spin  $d$ -level  $i = \psi_o \downarrow$  with energy  $e_i$  interacts with an unoccupied down-spin  $d$ -level  $j = \psi_u \downarrow$  with energy  $e_j$  via the matrix element  $\langle i | \hat{H}_{\text{SO}}^0 | j \rangle$ , the associated energy lowering is given by  $\Delta E_{\text{SOC}} = -|\langle i | \hat{H}_{\text{SO}}^0 | j \rangle|^2 / |e_i - e_j|$ . In determining the preferred spin orientation, the most important interaction is the one with the smallest energy gap ( $e_i - e_j$ ). According to the split Cu 3d states of  $\text{CuCl}_2 \cdot 2\text{H}_2\text{O}$  (**Fig. 9.1d**), the empty  $(x^2 - y^2) \downarrow$  has the smallest energy gap with the filled  $xz \downarrow$  state. (The split Cu 3d states determined from the DFT+U calculations do not violate Kramers degeneracy theorem. By convention, the majority-spin states are chosen as up-spin states, and the minority-spin states as down-spin states. The alternative choice is equally valid thereby maintaining the doublet degeneracy of a spin-1/2 system.) The interaction between these two states through  $\hat{H}_{\text{SO}}^0$  predicts the easy-plane anisotropy, because the matrix element  $\langle xz \downarrow | \hat{H}_{\text{SO}}^0 | (x^2 - y^2) \downarrow \rangle$  can be nonzero via the  $\hat{L}_+$  and  $\hat{L}_-$  terms of  $\hat{H}_{\text{SO}}^0$ , which come with the coefficient  $\sin\theta$ . This matrix element also predicts the spin orientation along the Cu-O bond; given  $\theta = 90^\circ$ , the  $\langle xz \downarrow | \hat{H}_{\text{SO}}^0 | (x^2 - y^2) \downarrow \rangle$  term is rewritten as

$$\langle xz \downarrow | \hat{H}_{\text{SO}}^0 | (x^2 - y^2) \downarrow \rangle \propto \langle xz | \hat{L}_x \cos \phi + \hat{L}_y \sin \phi | x^2 - y^2 \rangle \propto \sin \phi$$

because  $\langle xz | \hat{L}_x | x^2 - y^2 \rangle = 0$  and  $\langle xz | \hat{L}_y | x^2 - y^2 \rangle = -i$ .<sup>3</sup> Consequently, the matrix element is maximum when  $\phi = 90^\circ$ , namely, the preferred spin orientation in the local  $xy$ -plane is along the Cu-O bond (**Fig. 9.1c**).

The above discussion shows that the easy-plane anisotropy of the  $\text{Cu}^{2+}$  ions in  $\text{CuCl}_2 \cdot 2\text{H}_2\text{O}$  is due solely to their SIA. We now show that the same is true for the easy-plane anisotropy of the  $\text{Cu}^{2+}$  ions in  $\text{LiCuVO}_4$ ,<sup>19</sup>  $\text{CuCl}_2$ <sup>20</sup> and  $\text{CuBr}_2$ ,<sup>22</sup> in which the square planar  $\text{CuL}_4$  units ( $L = \text{O}, \text{Cl}, \text{Br}$ ) share their opposite edges to form  $\text{CuL}_2$  ribbon chains (**Fig. 9.2a**). Neutron powder diffraction studies showed that these  $\text{Cu}^{2+}$  spins prefer to lie in the planes of the  $\text{CuL}_4$  units (i.e., easy-plane anisotropy). Furthermore, the spins in each  $\text{CuL}_2$  ribbon chain has a spin-spiral arrangement (**Fig. 9.2b**) due to the spin frustration arising from the FM nearest-neighbor spin exchange  $J_{\text{nn}}$  and the AFM next-nearest-neighbor spin exchange  $J_{\text{nnn}}$ .<sup>14,20-22</sup> We examine the cause for this easy-plane anisotropy as follows:

(1) To determine if this anisotropy is caused by the ASE interactions, we consider three different models of spin arrangements in each  $\text{CuL}_2$  ribbon chain. One is the “isolated  $\text{Cu}^{2+}$  ion” model in which, of two ribbon chains per unit cell, all  $\text{Cu}^{2+}$  ions of one chain are replaced with  $\text{Mg}^{2+}$  ions while the other chain is converted to a  $(\text{Cu}^{2+}-\text{Mg}^{2+}-\text{Mg}^{2+}-\text{Mg}^{2+})_\infty$  chain (**Fig. 9.2c**). The second model has the  $\uparrow\downarrow\uparrow\downarrow$  collinear arrangement of  $\text{Cu}^{2+}$  spins in each ribbon chain (**Fig. 9.2d**), and the third model has the  $\uparrow\rightarrow\downarrow\leftarrow$  spin-spiral arrangement of  $\text{Cu}^{2+}$  spins in each ribbon chain (**Fig. 9.2b**). For each of these spin arrangements, we carry out DFT+U+SOC calculations for the  $\parallel xy$  and  $\perp xy$  spin orientations to determine their

relative energies. In the case of the spin-spiral arrangement, the  $\perp_{xy}$  spin orientation means that the plane of the spin spiral is perpendicular to the ribbon plane. In the  $\perp_{xy}$  spin spiral, therefore, each spin direction is  $\pm 45^\circ$  away from the local  $\pm z$ -axis. Our calculations for the “isolated  $\text{Cu}^{2+}$  ion” model show that the  $\parallel_{xy}$  orientation is more stable than the  $\perp_{xy}$  orientation (**Table 9.3**), indicating that the easy-plane anisotropy is an intrinsic property of an isolated  $\text{CuL}_4$  unit. The relative energies,  $E_{\parallel_{xy}} - E_{\perp_{xy}}$ , obtained from the  $\uparrow\downarrow\uparrow\downarrow$  chain model are practically identical to those obtained from the “isolated  $\text{Cu}^{2+}$  ion” model, so the spin exchanges  $J_{nn}$  and  $J_{nnn}$  are not responsible for the easy-plane anisotropy. It is reasonable to assume that the components  $J_{nn-x}$ ,  $J_{nn-y}$  and  $J_{nn-z}$  are all FM because  $J_{nn}$  is FM, while the components  $J_{nnn-x}$ ,  $J_{nnn-y}$  and  $J_{nnn-z}$  are all AFM because  $J_{nnn}$  is AFM. Then, the preference for the  $\parallel_{xy}$  spin orientation is explained if  $J_{nn-x}, J_{nn-y} > J_{nn-z}$  and/or if  $|J_{nnn-x}|, |J_{nnn-y}| > |J_{nnn-z}|$ . The  $\uparrow\downarrow\uparrow\downarrow$  spin arrangement does not fulfil these conditions, but it shows the preference for the  $\parallel_{xy}$  spin orientation, just as the “isolated  $\text{Cu}^{2+}$  ion” model predicts. In the case of the spin-spiral arrangement as well, the  $\parallel_{xy}$  spin orientation is favored over the  $\perp_{xy}$  spin orientation (**Table 9.2**). However, the energy difference,  $E_{\parallel_{xy}} - E_{\perp_{xy}}$ , for the spin-spiral arrangement is approximately half of that found for the  $\uparrow\downarrow\uparrow\downarrow$  collinear spin arrangement. This is so because, for each spin of the out-of-plane spin spiral arrangement, only 50% has the  $\parallel_z$  spin component. In short, the ASE interactions are not responsible for the observed easy-plane anisotropy.

(2) Our MDD energy calculations using the  $\uparrow\downarrow\uparrow\downarrow$  spin arrangement in each  $\text{CuL}_2$  ribbon chain show that the  $\perp_{xy}$  spin orientation is more stable than the  $\parallel_{xy}$  spin orientation by 0.07,

0.07 and 0.01 meV/Cu for LiCuVO<sub>4</sub>, CuCl<sub>2</sub> and CuBr<sub>2</sub>, respectively. The MDD interactions are too weak to influence the spin orientation.

(3) We now examine the crystal-field split Cu 3d states of LiCuVO<sub>4</sub>, CuCl<sub>2</sub> and CuBr<sub>2</sub> and their interaction under SOC. As a representative example, **Fig. 9.2e** shows the PDOS plots calculated for CuCl<sub>2</sub> (see the Supporting Material for the PDOS plots of LiCuVO<sub>4</sub> and CuBr<sub>2</sub>). We note that  $\langle x^2 - y^2 | \hat{L}_\mu | x^2 - y^2 \rangle = 0$  for  $\mu = x, y$  and  $z$ ,<sup>3</sup> and  $\langle z^2 \downarrow | \hat{H}_{\text{SO}} | (x^2 - y^2) \downarrow \rangle = 0$  because the magnetic quantum number of  $z^2$  differs from those of  $x^2 - y^2$  by 2. Consequently, **Fig. 9.2e** shows that the preferred spin orientation is determined by the interaction terms  $\langle xy \downarrow | \hat{H}_{\text{SO}} | (x^2 - y^2) \downarrow \rangle$  and  $\langle (xz/yz) \downarrow | \hat{H}_{\text{SO}} | (x^2 - y^2) \downarrow \rangle$ . The filled  $(xz/yz) \downarrow$  states are closer to the empty  $(x^2 - y^2) \downarrow$  states than are the filled  $xy \downarrow$  states so that the  $\parallel xy$  spin orientation is favored over the  $\perp xy$  spin orientation, in agreement with experiment. Thus, just as in the case of CuCl<sub>2</sub>·2H<sub>2</sub>O, the easy-plane anisotropy of the spin-1/2 Cu<sup>2+</sup> ions in LiCuVO<sub>4</sub>, CuCl<sub>2</sub> and CuBr<sub>2</sub> is caused by their SIA. The spin orientations of the Cu<sup>2+</sup> ions in Bi<sub>2</sub>CuO<sub>4</sub> and Li<sub>2</sub>CuCl<sub>2</sub> are briefly mentioned in the Supporting Material.

In summary, the observed easy-plane anisotropy of the spin-1/2 Cu<sup>2+</sup> ions in CuCl<sub>2</sub>·2H<sub>2</sub>O, LiCuVO<sub>4</sub>, CuCl<sub>2</sub> and CuBr<sub>2</sub> is not caused by their ASE interactions, nor by their MDD interactions, but by their SIA. A spin-1/2 ion should possess SIA unless the magnetic orbital accommodating an unpaired electron is triply degenerate as found in Ba<sub>2</sub>NaOsO<sub>6</sub>,<sup>23</sup> so most spin-1/2 ions should have SIA. In superconducting precursor La<sub>2</sub>CuO<sub>4</sub>, calculations show the Cu<sup>2+</sup> ions to possess easy-plane anisotropy,<sup>5</sup> and the presence of SIA at each Cu<sup>2+</sup> site is not prevented by any symmetry consideration. Thus, it would be

interesting to see if the SIA of  $\text{Cu}^{2+}$  ions has any effect on the spin fluctuation in cuprates <sup>24</sup>  
believed to be the key to understanding their superconductivity.

## References

1. (a) T. Moriya and K. Yoshida, *Prog. Theoret. Phys.* **1953**, 9, 663. (b) For example, see the lecture note of M. Suzuki and I. Suzuki on spin Hamiltonian of transition metal ions in crystal field, <http://www2.binghamton.edu/physics/docs/crystal-field6-15-07.pdf>.
2. (a) M. H. L. Pryce, *Proc. Phys. Soc.* **1950**, A 63, 25. (b) N. Majlis, *The Quantum Theory of Magnetism* (World Scientific, Singapore, 2000).
3. D. Dai, H. J. Xiang and M.-H. Whangbo, *J. Comput. Chem.* **2008**, 29, 2187.
4. H. A. Kramers, *Proc. Amsterdam Acad.* **1930**, 33, 959.
5. H. J. Xiang, E. J. Kan, M.-H. Whangbo, C. Lee, S.-H. Wei and X. G. Gong, *Phys. Rev.* **2011**, 83, 174402.
6. (a) G. Kresse and J. Hanfner, *Phys. Rev. B.* **1993**, 47, 558. (b) G. Kresse and J. Furthmüller, *Comput. Mater. Sci.* **1996**, 6, 15. (c) G. Kresse and J. Furthmüller, *Phys. Rev. B.* **1996**, 54, 11169.
7. J. P. Perdew, S. Burke and M. Ernzerhof, *Phys. Rev. Lett.* **1996**, 77, 3865.
8. A. I. Liechtenstein, V. I. Anisimov and J. Zaanen, *Phys. Rev. B.* **1995**, 52, 5467.
9. E. Bousquet and N. Spaldin, *Phys. Rev. B.* **2010**, 82, 220402.
10. H.-J. Koo, H. J. Xiang, C. Lee and M.-H. Whangbo, *Inorg. Chem.* **2009**, 48, 9051.
11. (a) P. P. Ewald, *Ann. Phys.* **1921**, 64, 253. (b) T. Darden, D. York and L. Pedersen, *J. Chem. Phys.* **1993**, **98**, 10089. (c) H. Wang, F. Dommert and C. Holm, *J. Chem. Phys.* **2010**, 133, 034117.
12. A. Basem, ICSD #163013.
13. N. J. Poulis and G. E. G. Haderman, *Physica* **1952**, 18, 201.

14. H. J. Xiang, C. Lee, H.-J. Koo, X. G. Gong and M.-H. Whangbo, *Dalton Trans.* **2013**, 42, 823.
15. X. Wang, R. Wu, D.-S. Wang and A. J. Freeman, *Phys. Rev. B.* **1996**, 54, 61.
16. H. J. Xiang, S.-H. Wei and M.-H. Whangbo, *Phys. Rev. Lett.* **2008**, 100, 167207.
17. H. J. Xiang, S.-H. Wei, M.-H. Whangbo and J. L. F. Da Silva, *Phys. Rev. Lett.* **2008**, 101, 037209.
18. S. Ji, E. J. Kan, M.-H. Whangbo, J.-H. Kim, Y. Qiu, M. Matsuda, H. Yoshida, Z. Hiroi, M. A. Green, T. Ziman, and S.-H. Lee, *Phys. Rev. B.* **2010**, 81, 094421.
19. B. J. Gibson, R. K. Kremer, A. V. Prokofiev, W. Assmus and G. J. McIntyre, *Physica B* **2004**, 350, e253.
20. M. G. Banks, R. K. Kremer, C. Hoch, A. Simon, B. Ouladdiaf, J.-M. Broto, H. Rakoto, C. Lee and M.-H. Whangbo, *Phys. Rev. B.* **2009**, 80, 024404.
21. L. Zhao, T.-L. Hung, C.-C. Li, Y.-Y. Chen, M.-K. Wu, R. K. Kremer, M. G. Banks, A. Simon, M.-H. Whangbo, C. Lee, J. S. Kim, I. G. Kim and K. H. Kim, *Adv. Mater.* **2012**, 24, 2469.
22. (a) D. Dai, H.-J. Koo and M.-H. Whangbo, *Inorg. Chem.* **2004**, 43, 4026. (b) H.-J. Koo, C. Lee, M.-H. Whangbo, G. J. McIntyre and R. K. Kremer, *Inorg. Chem.* **2011**, 50, 3582.
23. H. J. Xiang and M.-H. Whangbo, *Phys. Rev. B.* **2007**, 75, 052407.
24. For example, see: E. Demler and S.-C. Zhang, *Nature*, **1998**, 396, 733.

**Table 9.1** The energy (in meV/Cu) of the  $\parallel_{xy}$  spin orientation with respect to that of the  $\perp_{xy}$  spin orientation,  $E_{\parallel_{xy}} - E_{\perp_{xy}}$ , obtained from the DFT+U+SOC calculations for three models of  $\text{CuCl}_2 \cdot 2\text{H}_2\text{O}$ .<sup>a</sup>

$U_{\text{eff}}$	4 eV	5 eV	6 eV
<b>Model I<sup>b</sup></b>	-0.35	-0.31	-0.27
<b>Model II<sup>c</sup></b>	-0.23	-0.20	-0.17
<b>Model III<sup>d</sup></b>	-0.23	-0.20	-0.18

<sup>a</sup> In the  $\parallel_{xy}$  spin orientation, the spin is parallel to the Cu-O bond.

<sup>b</sup> “Isolated  $\text{Cu}^{2+}$  ion” model

<sup>c</sup> “Isolated  $\text{Cu}^{2+}$  chain” model with  $\uparrow\downarrow\uparrow\downarrow$  spin arrangement

<sup>d</sup> “Isolated  $\text{Cu}^{2+}$  chain” model with  $\uparrow\uparrow\downarrow\downarrow$  spin arrangement

**Table 9.2** The values of the three components  $J_{nn-x}$ ,  $J_{nn-y}$  and  $J_{nn-z}$  (in meV) of the nearest-neighbor spin exchange  $J_{nn}$  in  $\text{CuCl}_2 \cdot 2\text{H}_2\text{O}$  determined from DFT+U+SOC calculations.

	$U_{\text{eff}} = 4 \text{ eV}$	$U_{\text{eff}} = 5 \text{ eV}$	$U_{\text{eff}} = 6 \text{ eV}$
$J_{nn-x}$	-1.335	-1.090	-0.885
$J_{nn-y}$	-1.335	-1.090	-0.890
$J_{nn-z}$	-1.335	-1.095	-0.890

**Table 9.3** The relative energies,  $E_{\parallel xy} - E_{\perp xy}$ , in meV/Cu obtained from DFT+U+SOC calculations for the “isolated  $\text{Cu}^{2+}$  ion” model, the  $\uparrow\downarrow\uparrow\downarrow$  chain model (in parenthesis), and the  $\uparrow\rightarrow\downarrow\leftarrow$  spin-spiral chain model (in square bracket).

	$U_{\text{eff}} = 4 \text{ eV}$	$U_{\text{eff}} = 5 \text{ eV}$	$U_{\text{eff}} = 6 \text{ eV}$
<b>LiCuVO<sub>4</sub></b>	-0.35 <sup>a</sup> , (-0.36) <sup>b</sup> , [-0.18] <sup>c</sup>	-0.31 <sup>a</sup> , (-0.31) <sup>b</sup> , [-0.17] <sup>c</sup>	-0.26 <sup>a</sup> , (-0.27) <sup>b</sup> , [-0.14] <sup>c</sup>
<b>CuCl<sub>2</sub></b>	-0.29, (-0.26), [-0.15]	-0.23, (-0.22), [-0.13]	-0.21, (-0.19), [-0.12]
<b>CuBr<sub>2</sub></b>	-0.13, (-0.16), [-0.07]	-0.11, (-0.14), [-0.06]	-0.10, (-0.12), [-0.05]

<sup>a</sup> The “isolated  $\text{Cu}^{2+}$  ion” model

<sup>b</sup> The  $\uparrow\downarrow\uparrow\downarrow$  chain model

<sup>c</sup> The  $\uparrow\rightarrow\downarrow\leftarrow$  spin-spiral chain model

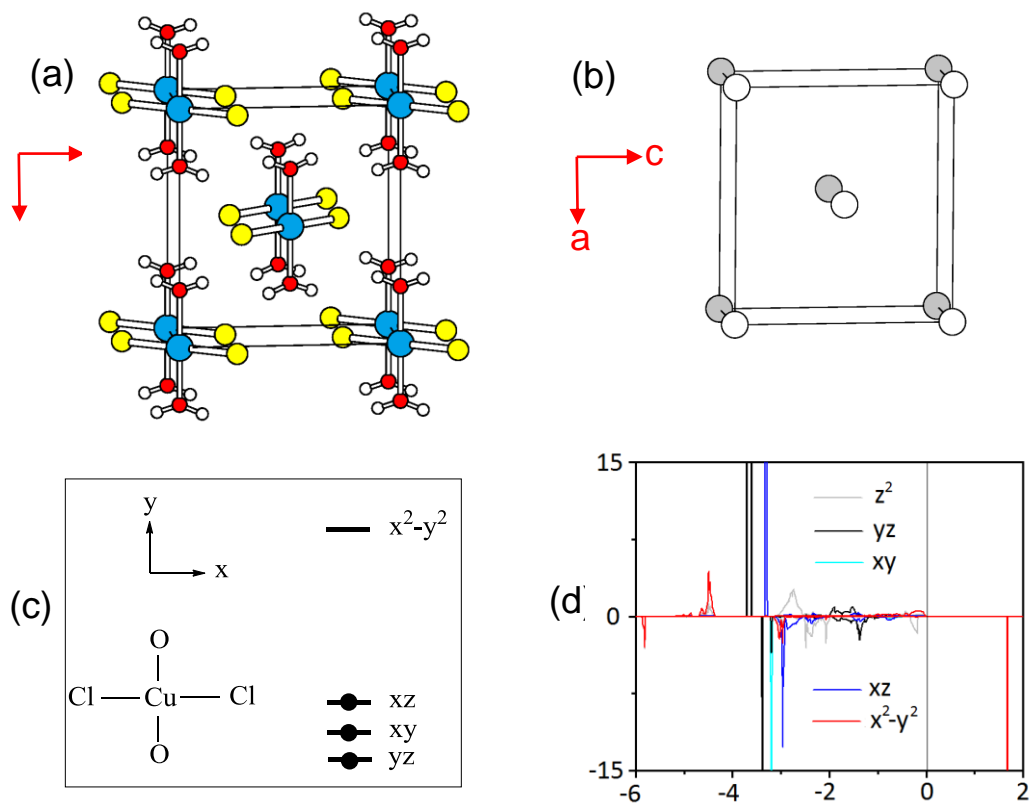


**Fig. 9.1** (a) A perspective view of the crystal structure of  $\text{CuCl}_2 \cdot 2\text{H}_2\text{O}$  (blue circle: Cu, yellow circle: Cl, red circle: O, white circle: H). (b) The magnetic structure of  $\text{CuCl}_2 \cdot 2\text{H}_2\text{O}$ , where the filled and unfilled circles represent up-spin and down-spin  $\text{Cu}^{2+}$  sites, respectively. (c) The local coordinate system chosen for an isolated  $\text{CuCl}_2(\text{OH}_2)_2$  complex with the crystal-field split Cu 3d states. (d) The PDOS plots calculated for the Cu 3d states of  $\text{CuCl}_2 \cdot 2\text{H}_2\text{O}$  using the “isolated  $\text{Cu}^{2+}$  ion” model.

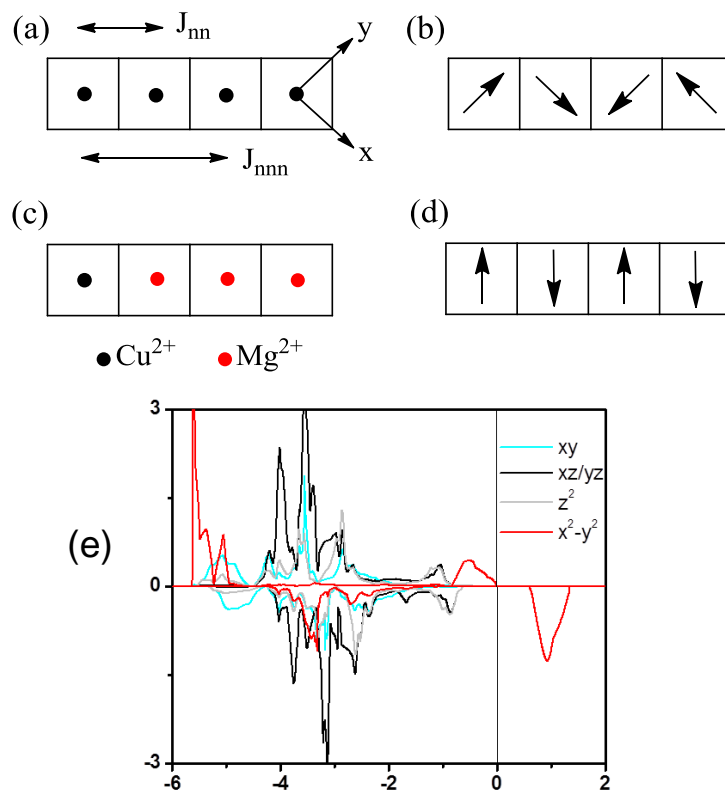


**Fig. 9.2** (a) A schematic view of a  $\text{CuL}_2$  ( $L = \text{O}, \text{Cl}, \text{Br}$ ) ribbon chain found in  $\text{LiCuVO}_4$ ,  $\text{CuCl}_2$  and  $\text{CuBr}_2$ . (b) A schematic view of the  $\uparrow \rightarrow \downarrow \leftarrow$  spin-spiral arrangement in the  $\text{CuL}_2$  ribbon chain, for the case when the spin-spiral plane is the  $xy$ -plane. (c) An “isolated  $\text{Cu}^{2+}$  ion” model, in which a chain of  $\text{Cu}^{2+}$  ions is replaced with a  $(\text{Cu}^{2+}-\text{Mg}^{2+}-\text{Mg}^{2+}-\text{Mg}^{2+})_\infty$  chain. (d) A schematic view of the  $\uparrow \downarrow \uparrow \downarrow$  collinear arrangement of  $\text{Cu}^{2+}$  spins in the  $\text{CuL}_2$  ribbon chain, for the case when the spins lie in the  $xy$ -plane. (e) The PDOS plots calculated for the Cu 3d states of  $\text{CuCl}_2$ .

## 10. Concluding remarks

In this dissertation, we reported results of our DFT calculations on a number magnetic oxides, which were carried out to help understand their observed magnetic properties. The essential findings of our studies can be summarized as follows:

(a) The magnetic properties of  $\text{Ag}_2\text{ZnZr}_2\text{F}_{14}$  and  $\text{FeTe}_3\text{O}_7\text{X}$  ( $\text{X} = \text{Cl}, \text{Br}$ ) are well described by an isolated AFM dimer model.

(b) In the observed magnetic structure of  $\text{LiNaCo}[\text{PO}_4]\text{F}$ , the FM chains of  $\text{Co}^{2+}$  ions along the b-direction are antiferromagnetically coupled along the a-direction, but have a non-collinear spin arrangement along the c-direction. These observations suggest the absence and the presence of spin frustration along the a- and c-directions, respectively. These aspects are well explained by the spin exchange parameters obtained from our GGA+U calculations.

(c) The study of  $\text{CuAs}_2\text{O}_4$  by DFT calculations reveals the presence of dominant nearest-neighbor FM spin exchange interactions, which is four times stronger than the next-nearest-neighbor AFM spin exchange interactions along the ribbon chains.

(d) The magnetic oxides  $\text{ACo}_2\text{V}_2\text{O}_8$  ( $\text{A} = \text{Ba}, \text{Sr}, \text{Pb}$ ) all contain axially-compressed  $\text{CoO}_6$  octahdra, which indicates the possibility of uniaxial magnetic properties. We carried out GGA+U+SOC calculations and found that the  $\text{Co}^{2+}$  ions of these systems possess easy-axis anisotropy. This finding is explained by considering orbital interactions induced by SOC.

(e) In the study of  $\text{CuCl}_2 \cdot 2\text{H}_2\text{O}$ ,  $\text{LiCuVO}_4$ ,  $\text{CuCl}_2$  and  $\text{CuBr}_2$ , the cause for the preferred spin orientation of a spin-1/2 transition-metal ion was explored by studying the easy-plane anisotropy of the spin-1/2  $\text{Cu}^{2+}$  ions in all four compounds. The spin orientation observed for

these spin-1/2 ions is not caused by their anisotropic spin exchange interactions, nor by their magnetic dipole-dipole interactions, but by their single-ion anisotropy.